Nonlinear Hydrodynamic Analysis and Optimization of Bottom-Hinged Oscillating Wave Surge Converters in Shallow Water

by

LIU Yao

A Doctoral Dissertation

Submitted to the Graduate School of Engineering in Nagoya University

In Partial Fulfillment of the Requirements for the Degree of

Doctor of Engineering

Department of Civil and Environmental Engineering

Nagoya University, Japan

June 2022

Contents

List of Tables

List of Figures

Abbreviations

2D	Two-Dimensional
3D	Three-Dimensional
BEM	Boundary Element Method
CFD	Computational Fluid Dynamics
CWR	Capture Width Ratio
DOE	Design of Experiments
DOF	Degree of Freedom
EMEC	European Marine Energy Center
GA	Genetic Algorithm
IPS	Inter Project Service
JONSWAP	Joint North Sea Wave Project
LCOE	Levelized Cost of Energy
LHS	Latin Hypercube Sampling
LMM	Lateral Mobile Module
MOGA	Multi-Objective Genetic Algorithm
NRMSE	Normalized Root Mean Square Error
NWT	Numerical Wave Tank
OAT	One-at-A-Time
OWC	Oscillating Water Column
OWSC	Oscillating Wave Surge Converter
PISO	Pressure Implicit Splitting Operator
PIMPLE	PISO-SIMPLE
PTO	Power Take-Off
RANS	Reynolds-Averaged Navier-Stokes
SIMPLE	Semi-Implicit Method for Pressure-Linked Equations
SKE	Standard k-ε
SPH	Smoothed Particle Hydrodynamics
TMA	TEXEL-MARSEN-ARSLOE
VOF	Volume of Fluid
WEC	Wave Energy Converter

Nomenclature

A_i	Incident wave amplitude of a regular wave
$A(\omega_n)$	Wave amplitude of the nth wave component of an irregular wave
$A_u(\omega)$	Wave amplitude at frequency ω for calculating the transfer function in the expression of response spectrum
b	OWSC thickness
$\overline{BH}$	Constant force arm of buoyancy in the vertical position
$\overline{BH}(t)$	Time-varying force arm of buoyancy
$c(\omega)$	Radiation damping coefficient
C_b	Constant PTO brake damping coefficient
$C_B(t)$	Nonlinear PTO braking damping
C_d	Drag coefficient
$C_g(\omega)$	Wave group velocity
C_{DL}	Linearized drag damping
C_{PTO}	PTO damping
C_{PTOL}	Linearized PTO damping
C_{PTO_opt}	Optimal PTO damping
CWR	Capture width ratio
d	Water depth
d_a	Axis depth
$d_{overset}$	Distance between external cubic surface of the overset zone and the flap surface in CFD computational domain
dt	Time step of integration in time-domain BEM
F_b	Constant buoyancy in the vertical position
$F_b(t)$	Time-varying buoyant force
F_D	Drag force
g	Gravity acceleration
$\overline{GH}$	Force arm of gravity
h	OWSC height
h_e	Height of flap encountering the flow in pseudo 2D steady CFD

h_f	OWSC freeboard height
$h_w(t)$	Time-varying wet surface height
$H_{1/3}$	Significant wave height
I_G	Pitch inertia torque about the gravity center
I_H	Pitch inertia torque about the hinged axis
I_{PTO}	PTO inertia torque about the hinged axis
k in CFD	Turbulent kinetic energy
k in BEM or $k(\omega, d)$	Wave number for a finite depth
$k(\omega, \infty)$	Wave number at infinite depth
k_n	Wave number of the nth wave component
K_0	Initial stiffness when the flap is undisturbed in still water
$K_H(t)$	Hydrostatic stiffness
K_{HL}	Linearized hydrostatic stiffness
$K_{instant}(t)$	Hydrostatic stiffness based on the instantaneous wet surface
$K_{mean}(t)$	Hydrostatic stiffness based on the mean wet surface
K_{PTO}	PTO stiffness
KC	Keulegan–Carpenter number
m	OWSC mass
m_s	Structural mass of flap per unit width
M_D	Drag moment
M_E	Wave exciting moment
$M_f(t)$	PTO friction moment
$M_{fluid}(t)$	Total fluid moment acting on the flap surface
M_H	Hydrostatic Restoring Moment
M_{PTO}	PTO moment
M_R	Radiation damping moment
$\vec{\boldsymbol{n}}$	Unit outer-pointing normal vector of the surface elements of the flap in CFD
N_c	Number of peak values after the beginning time t_b for the measurement of phases

N_{GL}	Number of grid layer between external cubic surface of the overset zone and the flap surface in CFD computational domain
N_o	Number of objective functions in MOGA
N_w	Number of wave components for an irregular wave
o	Origin of coordinate system
$O(H_{1/3}, T_{1/3})$	Percentage occurrence of a sea state
O_j	Normalized objective function for the jth objective function in MOGA
p	Fluid pressure in CFD
P_{ac}	Mean annual capturing wave power
P_c	Time–averaged capturing power
P_{c_opt}	Maximized capturing power
P_i	Input parameter
P_o	Output parameter
$P_{o,max}$	Maximum values of output parameters
$P_{o,min}$	Minimum values of output parameters
$P_{o,t}$	A value dependent on the target of optimization
P_{res}	Mean annual power of wave energy resource per unit width
P_w or $P_w(H_{1/3}, T_{1/3})$	Incident wave power per unit width
r	Radial coordinate of the flap based on the hinge
$R(t)$	Impulse response function
$\vec{\boldsymbol{r}}_s$	Position vector of the point on the flap surface in CFD
$\vec{\boldsymbol{r}}_h$	Position vector of the hinge in CFD
Re	Reynolds number
s	Fluid–structure interface in CFD
S	Dimensionless local sensitivity coefficients
$\vec{\boldsymbol{S}}$	Fluid body force per unit mass in CFD
$S(\omega)$	Irregular wave spectrum at infinite water depth
$S_{BM}(\omega)$	Bretschneider-Mitsuyasu Spectrum
$S_d(\omega_n)$	Irregular wave spectrum at water depth d
$S_J(\omega)$	JONSWAP Spectrum

$S_{out}(\omega)$	Response spectrum
$S_{PM}(\omega)$	Pierson-Moskowitz Spectrum
t or τ	Time
t_b	Beginning time for power recording
t_e	End time for power recording
t_{p,M_E}	Time of peak moment
$t_{p,\dot{\varphi}}$	Time of peak angular velocity
T	Regular wave period
T_0	Mean zero-crossing wave period
$T_{1/3}$	Significant wave period
T_n	OWSC natural period
T_p	Spectral peak period
T_{PTO}	Constant value of PTO friction torque
$\vec{\boldsymbol{T}}$	Fluid stress tensor
$u_n(t)$	Normal velocity of the water particles (in the absence of the flap) on the mid-surface of the flap
$u_x(t)$	Horizontal components of the water particle velocities in the absence of the flap
$u_z(t)$	Vertical components of the water particle velocities in the absence of the flap
v	Incoming current velocity
$\vec{\boldsymbol{v}}$	Fluid velocity vector in CFD
$\vec{\boldsymbol{v}}_S$	Velocity on the fluid–structure interface in CFD
w	OWSC width
W_j	Weighting factor for the jth objective function
x	x axis or coordinate
z	z axis or coordinate
α	Volume fraction of water in CFD
α_k	Modification factor of surface-piercing OWSCs for the adjustment of stiffness
α_{TMA}	Variable coefficient in TMA spectrum

β_J	A parameter of JONSWAP spectrum
γ	Peak enhancement factor of JONSWAP spectrum
δ_c	A bias factor between 0 and 1 for gene crossover in MOGA
δ_m	A small and random variation for gene mutation in MOGA
ε	Turbulent dissipation rate
η	Mean annual CWR
$\eta(t)$	Incident wave elevation
θ	Phase difference between the incident wave and the response under regular waves
θ_1	Phase angle of pitch relative to wave exciting moment
θ_2	phase angular velocity of pitch relative to wave exciting moment
$\mu(\omega)$	Added inertia torque
$\mu(\infty)$	Added inertia torque at infinite frequency
μ	Equivalent dynamic viscosity
μ_1	Air dynamic viscosity
μ_2	Water dynamic viscosity
μ_t	Turbulent viscosity in CFD
ρ or ρ_2	Water density
ρ_1	Air density
σ	A parameter of JONSWAP spectrum
φ	OWSC rotational angle
$\dot{\varphi}$	OWSC angular velocity
$\ddot{\varphi}$	OWSC angular acceleration
φ_0	Pitch amplitude in frequency-domain analysis under regular waves
φ_{amp}	Equivalent pitch amplitude under regular waves
$\bar{\varphi}_{amp}$	Time-averaged pitch amplitude under regular waves
$\dot{\varphi}_{amp}$	Equivalent pitch amplitude under regular waves
$\varphi_{b,i}$	The angle when the brake starts to work in PTO braker
$\varphi_{b,f}$	The angle above which the brake damping is constant in PTO braker
φ_{eq}	Equivalent pitch amplitude under irregular waves
φ_s	Significant value of pitch under irregular waves

$\varphi_k(\omega, d)$	Kitaigorodskii's factor for shoaling correction of irregular waves
$\varphi_{TMA}(\omega, d)$	Depth-dependent function in TMA spectrum
$\phi(\omega_n)$	Random phase of wave components for an irregular wave
Φ	Weighted objective function in MOGA
$\psi(\omega)$ or $\psi(\omega_n)$	Phase difference between the incident wave and the wave exciting moment
ω	Wave angular frequency of a regular wave
ω_n	Wave angular frequency of the nth wave component of an irregular wave
ω_p	Spectral peak frequency
ΔC	Total damping except C_{PTO}.
ΔI	Total inertia torque except I_{PTO}
$\Delta\omega$	Wave frequency interval of wave components

Abstract

This doctoral dissertation studied the nonlinear hydrodynamics and optimization of bottom-hinged oscillating wave surge converters (OWSCs) in shallow water.

In Chapters 1–4, the background and methodologies were introduced. Firstly, the nearshore environments—in particular, shoaling regular and irregular waves, were described. The typical irregular wave spectrums were contrastively illustrated. The spectral values in shallow water should be modified according to the water depth. Based on boundary element method (BEM), the equations of time-varying environmental loads were presented, considering the effects of instantaneous wet surface on the hydrostatic restoring moment and drag moment. The frequency-domain and time-domain mathematical models were established. The linearization of nonlinear stiffness, drag moment, and power take-off (PTO) friction moment was applied in the nonlinear frequency-domain analysis. Python codes were developed to solve the dynamic equations and hydrodynamic performances. Furthermore, the numerical wave tank (NWT) of two-phase flow (water and air) based on computational fluid dynamics (CFD) was built for high-fidelity simulations.

Chapter 5 simply considered the still water surface to calculate the time-varying wet surface for the computation of nonlinear hydrostatic restoring moment and drag moment. The BEM-based numerical results of the pitch amplitude in study cases were compared well with the published experimental data. The nonlinear items cannot be neglected, especially when the pitch amplitude grows up to 30°. Surface-piercing OWSC can capture more power than the same-sized fully submerged one in most wave conditions. The moderate increase of the PTO stiffness for a thin OWSC helps to enhance the peak of capture width ratio (CWR). A proper PTO damping helps to maximize the CWR for peak energy conditions. The PTO friction can significantly reduce the CWR at the whole wave period range, whereas the maximum influence of the viscosity occurs at the resonant wave period.

Chapter 6 studied the resonant behaviors, based on time-domain BEM, of a bottom-hinged OWSC as well as the relationship of resonance with the response and CWR. To improve the accuracy, a corrected wave surface was introduced to calculate the time-varying wet surface. The wave surface correcting factor and drag coefficient were calibrated with CFD. An intermediate initial angle in free decay is appropriate for use to determine the natural period. Under regular waves, the resonance occurs near the natural period for the uniform wave amplitude, rather than the uniform wave torque amplitude, and can disappear due to the

amplification of PTO friction. Under unit-amplitude regular waves, the period of maximum CWR is relatively close to the period of maximum velocity, but far from the natural period. Under irregular waves, no stable resonance is observed because the maximum equivalent pitch angle appears at different peak periods with the variation in PTO damping. When the period of a regular wave or the peak period of an irregular wave is close to the natural period, a phase hysteresis of velocity relative to wave torque always occurs.

Chapter 7 used the frequency-domain BEM method to study the feasibility of performance promotion of a bottom-hinged OWSC under regular and irregular waves in shallow water via adjusting PTO parameters. Under regular waves, the adjusting approaches are classified as: (1) no artificial resonance, (2) perfect resonance, and (3) near resonance. The results show that the adjustment towards resonance can boost the capturing power, although the flap-type absorber was recognized as a wave torque dominating device. A near-resonance situation is more effective to improve the hydrodynamic performance than a perfect resonance, in which the amplification of the damping item is disadvantageous. An increasing hysteretic phase angle of velocity relative to wave torque with the increase of wave period represents the best status of wave energy harvesting. Under irregular waves, the performance at a short peak period can be improved by adjusting PTO stiffness, while, adjusting PTO inertia torque is almost ineffective.

Chapter 8 designed an assembling OWSC with adaptive sizes for the target wave energy farms around Japan and evaluated the mean annual CWR under irregular waves. Unlike the inflexible drag coefficients in a steady flow, the drag coefficients in irregular waves are strongly affected by OWSC thickness. Multi-objective genetic algorithm (MOGA) optimization of OWSC geometric sizes, internal water filling, and PTO parameters was conducted for two objective functions: maximizing the mean annual CWR and minimizing the structural mass per unit width. The optimized result presents a slender OWSC that neutrally balances these two objectives. The effects and local sensitivities of the width, thickness, axis depth, water filling, PTO stiffness, damping, and friction were comprehensively discussed. The results show that the axis depth has the greatest positive influence on the CWR, and the increase in thickness creates a significant economic disadvantage due to a heavier structure. However, inertia adjustment by filling water does not benefit the mean annual CWR.

Chapter 9 presented the conclusions, innovations, and future research.

Keywords: OWSC; hydrodynamics; BEM; CFD; resonance; PTO system; CWR; performance enhancement; optimization

1 Introduction

1.1 Wave Energy Converters

Wave energy is a promising renewable energy resource, because of the advantages of high energy density and continuous supply, compared with other types of ocean energies, such as tidal current and wind. It has received increasing attention from researchers and engineers in recent decades (Astariz and Iglesias, 2015). Fig. 1-1 illustrates the worldwide dispersion of the averaged wave energy resource.

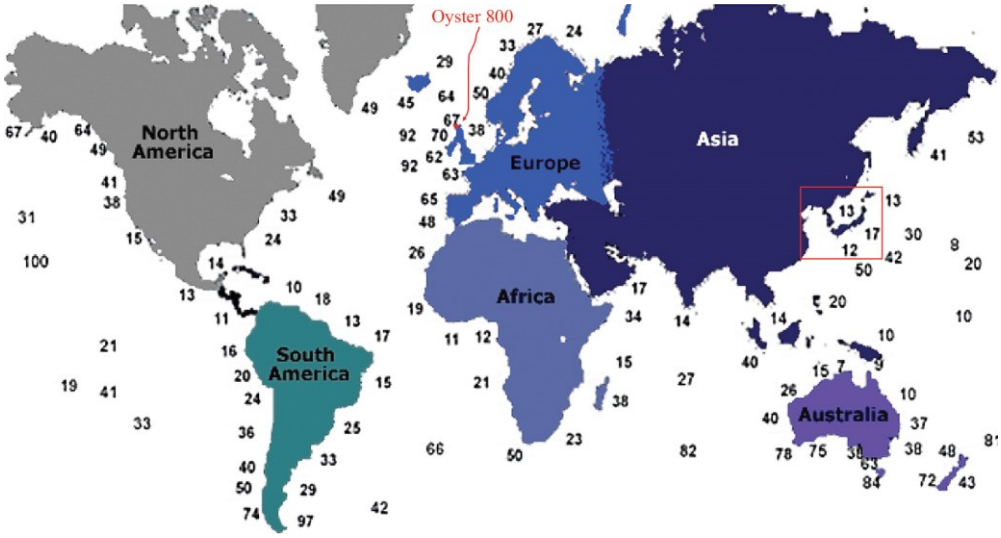

Fig. 1-1 Worldwide dispersion of the average wave energy resource in kW/m (Vates Avilés, 2009).

As the devices to exploit wave energy from the sea, many types of wave energy converters (WECs) were designed, for example, oscillating water column (OWC), overtopping WEC, point absorber, flap-type absorber, and attenuator-type WEC in Fig. 1-2.

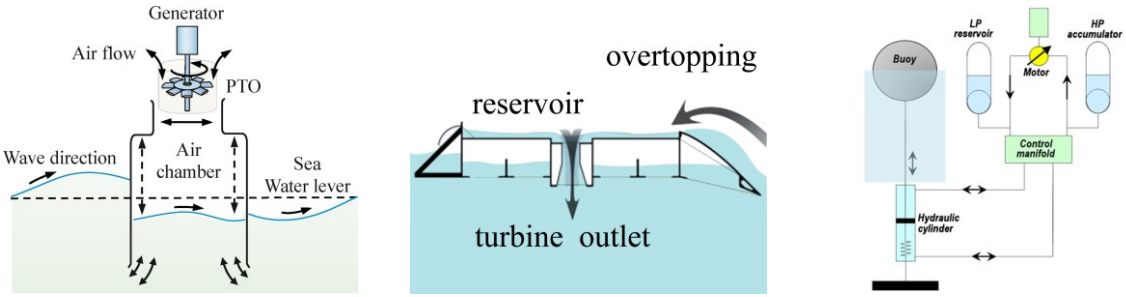

(a) (b) (c)

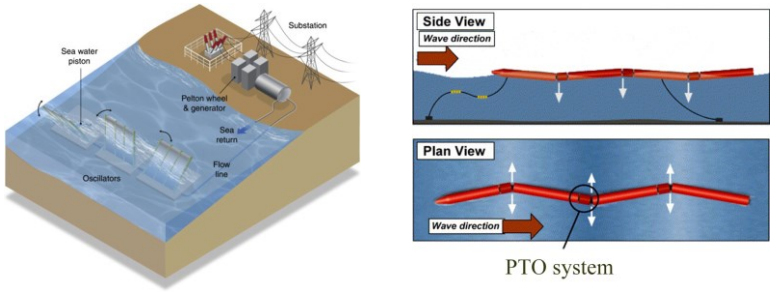

(d) (e)

Fig. 1-2 Principles of: (a) OWC (Zhang et al., 2021); (b) Overtopping WEC (Tedd and Kofoed, 2009); (c) Point absorber (Vicente et al., 2013); (d) Flap-type absorber (Li and Yu, 2012); (e) Attenuator-type WEC (Henderson, 2006).

1.1.1 OWCs

The OWC mainly consists of air chambers, air turbines, and generators. In a wave period, air flows through the air turbine first from the air chambers to the outside and then changes its direction. Subjected to the oscillating airflow, the unidirectional rotating air turbine with a special design, shown in Fig. 1-3, drives the generators.

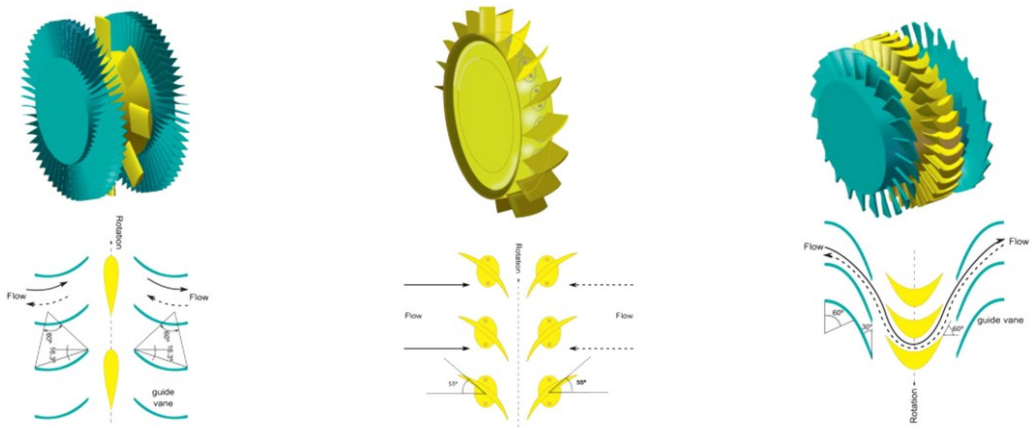

Fig. 1-3 Three examples of air turbines equipped in OWCs (López et al., 2013).

An OWC can be constructed on the coast or integrated with the fixed breakwater, called fixed OWC. Some famous fixed OWC includes British LIMPET (Heath et al., 2001), Portuguese Pico (Lagoun et al., 2010), Italian REWEC (Arena et al., 2013), etc. Another type is the semi-submerged or floating OWC, generally far away from the coastline, for example, the earliest large-scale Japanese Kaimei (Masuda and McCormick, 1986), Energetech OWC in Australia (Alcorn et al., 2005), Oceanlinx in Australia (Heath, 2007), OE buoy in Ireland (Gomes et al., 2012), Mighty Whale in Japan (Osawa et al., 2013), etc. A review of OWCs and air turbines can be found in Falcão and Henriques (2016). Some studies on the wave energy

capture performance of OWCs were conducted by López et al. (2019), Singh et al. (2020), and Zhao et al. (2021).

1.1.2 Overtopping WECs

The overtopping WECs can be also classified as fixed devices for onshore sites and floating devices for offshore areas. There are one or more reservoirs at the top to store water when the wave overtops the device. The principle of generating electricity is that the rotating low-head turbines are driven by the water flow from the reservoir to the sea. TAPCHAN (Mehlum, 1986) was the earliest fixed overtopping WEC, constructed by Norwave AS. Wave dragon (Kofoed et al., 2006) was a floating device developed by Denmark. SSG (Margheritini et al., 2009) was a three-levels overtopping WEC installed in Norway. The overtopping WECs can integrate with other structures, such as ships and breakwaters. The hydrodynamics of some overtopping devices were investigated by Victor et al. (2011), dos Santos et al. (2014), Palma et al. (2019), and Di Lauro et al. (2020).

1.1.3 Point Absorbers

A point absorber absorbs the wave energy by heaving up and down and transfers the mechanical energy to electrical energy via a PTO system. It was classified as single-body, two-bodies, and multi-floaters WECs, shown in Fig. 1-4. The point absorber has good adaptivity to the water depth of working area.

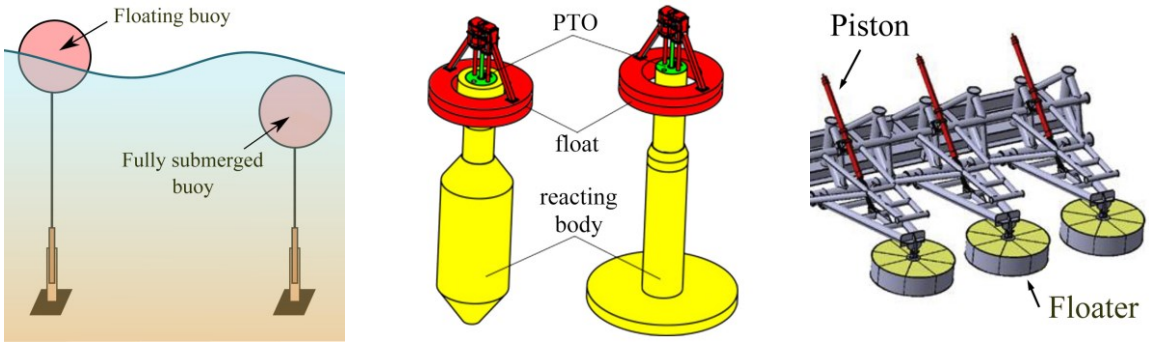

(a) (b) (c)

Fig. 1-4 The illustrations of: (a) Single-body absorber (Sergiienko et al., 2017); (b) Two-bodies absorber (Beatty et al., 2015); (c) Multi-floaters WEC (Kolios et al., 2018).

Some famous heaving point absorbers are listed as follows: AquaBuOY (Weinstein et al., 2004) developed by AquaEnergy, PowerBuoy (Liang and Zuo, 2017) developed by Ocean Power Technologies, Wavebob (Weber et al., 2009) in Ireland, Archimedes-Wave-Swing (Valério et al., 2007) in Portugal, CETO WEC (Mann, 2011) developed by Carnegie Wave

Energy, Inter Project Service (IPS) buoy (Gomes et al., 2010), SEACAP (Combourieu et al., 2014), InfinityWEC (Rashid et al., 2021) developed by Ocean Harvesting Technologies, and WaveStar (Windt et al., 2021). Unlike a traditional heaving point absorber, PS Frog Mk5 (McCabe et al., 2006) was a pitching-type point absorber, extracting wave energy by sliding motion of PTO mass in pitch direction. Some hydrodynamic studies of point absorbers were carried out by Zurkinden et al. (2014), Ropero-Giralda et al. (2020), and Schubert et al. (2020). Some optimization analyses of point absorbers for maximizing the performance were implemented by Pastor and Liu (2014), Shadman et al. (2018), and Alamian et al. (2019).

1.1.4 Flap-Type Absorber

As a flap-type absorber, the oscillating wave surge converter (OWSC) is the study object in this doctoral dissertation. The operation principle of an OWSC is moving back and forth like a flap in the waves to absorb wave energy. It was also recognized as a terminator-type absorber, because of its large size in the perpendicular direction of wave propagation. Budal's upper bound (Budal and Falnes, 1982) explained that the maximum value of the theoretical capture width ratio (CWR) of the flap-type absorber was double that of the axisymmetric point absorber.

According to the water depth, it is classified as fixed OWSCs in shallow water (Flocard and Finnigan, 2009) and floating OWSCs in offshore areas (Yu et al., 2014), for example, a fixed Oyster (Whittaker et al., 2007) and a floating Langlee (Lavelle and Kofoed, 2011). The exploitable wave power at near-shore locations (around 10 m water depth) was only 10 percent lower than the 50 m-deep-water regions under commonly occurring sea states (Whittaker and Folley, 2012). A nearshore wave energy farm has the advantages of powerful wave resources and milder wave climates than offshore locations. The fixed OWSCs were reported to have higher capture factors than the floating OWSCs (Babarit, 2015). Because the wave energy absorption is mainly due to the wave surge phenomenon, nearshore fixed OWSCs benefit from the amplified horizontal velocity of water particles in shallow water due to shoaling effects (Newman, 2018).

According to the pivot position, the fixed OWSCs are further classified as top-hinge (Folley et al., 2007b; Gunawardane et al., 2016) and bottom-hinged (Folley et al., 2007a). Babarit (2015) presented that the bottom-hinged flap mostly had a higher CWR than top-hinge OWSCs. Babarit et al. (2012) reported that the bottom-hinged OWSC captures greater mean annual power than most types of WECs.

The bottom-hinged OWSC can either be fully submerged or pierce the water surface. The most well-known devices, because of their advanced stage of development, are the WaveRoller and the Oyster, which are illustrated in Fig. 1-5 (Cheng et al., 2019).

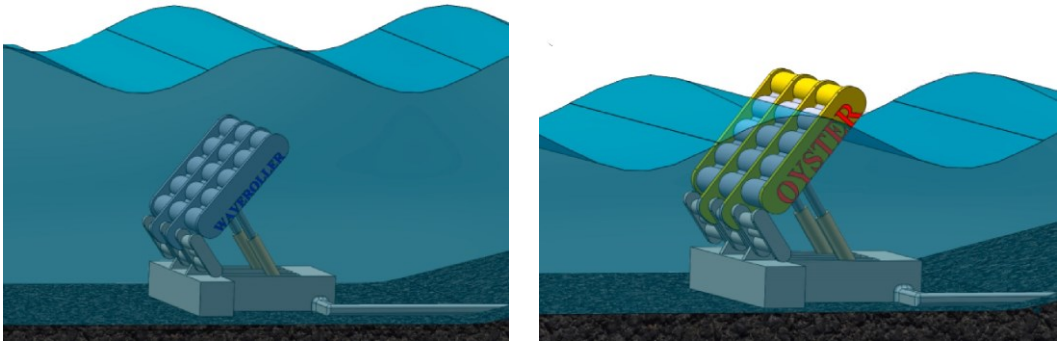

(a) (b)

Fig. 1-5 Conceptual graphs (Cheng et al., 2019) of: (a) WaveRoller; (b) Oyster.

The Finnish company AW-Energy has been developing WaveRoller technology since 2004. Oyster was being developed in the early 2000s by Aquamarine Power Ltd. in cooperation with Queen's University Belfast. Oyster 1, a full-scale prototype of OWSC with a rated power of 315 kW, was developed by Aquamarine Power, collaborating with Queen's University Belfast, installed at the European Marine Energy Center (EMEC) in Orkney, Scotland, in 2009, and decommissioned after its 2-year design life. The second-generation Oyster 800, with a rated power of 800 kW, was tested at EMEC in 2011, and successfully exported electricity to the national grid (O'Boyle et al., 2015). Whittaker and colleagues (Whittaker et al., 2007; Whittaker and Folley, 2012) documented several studies for the development of Oyster. The main difference between WaveRoller and Oyster is the position of the top edge, which is fully submerged for WaveRoller and pierces through the water surface for Oyster.

Experimental investigations by Cameron et al. (2010) showed that a surface-piercing OWSC, blocking the full height of the water column to ensure maximum wave force, was able to capture more wave power than a fully submerged OWSC with leakage of wave energy over the top of the flap. Therefore, the bottom-fixed surface-piercing OWSC is expected to become one of the most prominent nearshore WECs in the future. The numerical analyses of OWSCs were introduced in Section 1.2.

1.1.5 Attenuator-Type WECs

The attenuator-type WEC harvests wave energy by relatively rotational motion of multiple floating rafts. It generally has a large size along the wave propagating direction but a small size

in the perpendicular direction. The typic PTO system for attenuator-type WECs is a hydraulic generator driven by the motion of a piston, installed at the hinges between floating rafts. Some attenuator-type WECs include DEXA (Kofoed, 2009), Sea Power in Ireland, McCabe (Kraemer et al., 2001), Pelamis (Retzler, 2006) in Portugal, and Oceantec WEC (Salcedo et al., 2009). The hydrodynamics on attenuator-type WECs were studied by He et al. (2013), Liu et al. (2017), Wahid et al. (2017), Zhao et al. (2018), Capper et al. (2021), and Ghaneei and Mahmoudi (2021). Geometric optimization of a pivot two-bodies attenuator was implemented by Li et al. (2020). Optimal control of attenuator-type WECs was conducted by Liao et al. (2020).

1.1.6 Other Types

Lilypad, a flexible membrane-type WEC (Collins et al., 2019) submerged underwater connecting hose pumps with cables, as shown in Fig. 1-6, captures wave energy by the deformation of the membrane. The tensional cable produces hydraulic pressure inside the pumps and thus generates electricity.

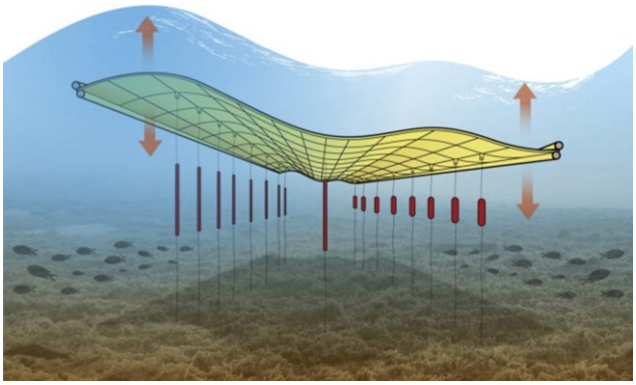

Fig. 1-6 Schematic of a membrane-type WEC (Li and Yu, 2012)

TALOS (Aggidis and Taylor, 2017), a novel multi-axis point absorber, consists of a hull and an internal PTO system, which was assembled by an inertial mass with multiple hydraulic pistons, as shown in Fig. 1-7. It has a similar working principle to SEAREV (Cordonnier et al., 2015).

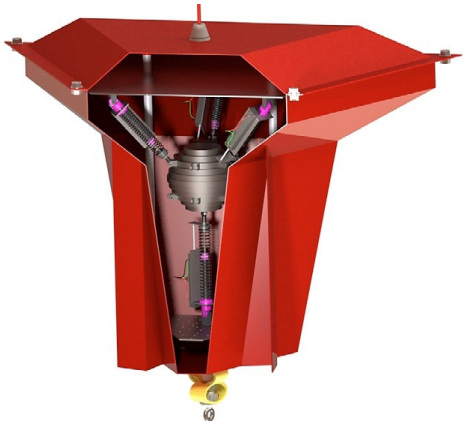

Fig. 1-7 A laboratory model of TALOS (Bhatt et al., 2016).

López et al. (2017) developed a CECO WEC, which consists of two lateral mobile modules (LMMs), an oblique slide way, and a fixed supporting part, as shown in Fig. 1-8. The LMMs oscillate under waves to make the electrical generator rotate through a gear–rack transfer system.

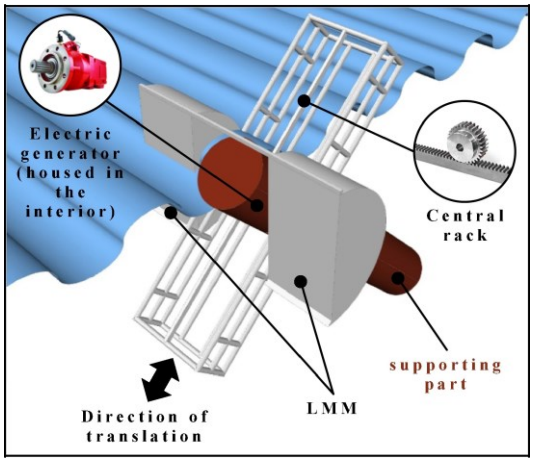

Fig. 1-8 A diagram of CECO WEC (López et al., 2017).

Gao and Yu (2018) numerically developed a three-degree-of-freedom (DOF) cone-cylinder WEC shown in Fig. 1-9, and optimized the diameter (D), draft (T), and z-coordinate of the gravity center for maximizing the absorption efficiency.

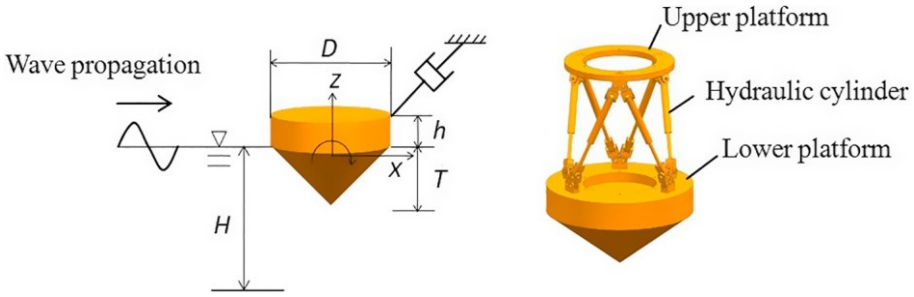

Fig. 1-9 A graph of cone-cylinder WEC (Gao and Yu, 2018).

ModuleRaft (Tongphong et al., 2021), a floating platform combining flap and attenuator concepts, consists of fully-submerged and top-hinged pendulums at the bottom for the absorption of horizontal wave force and semi-submerged rafts for capturing the vertical wave force, shown in Fig. 1-10.

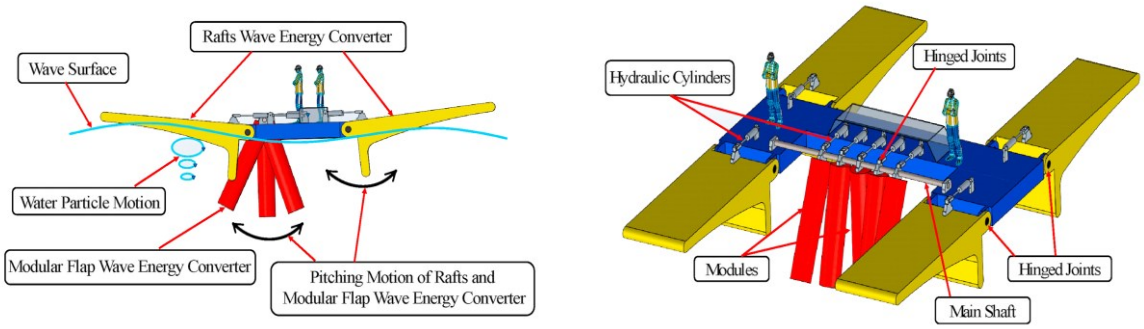

(a) (b)

Fig. 1-10 Conceptual model (Tongphong et al., 2021) of ModuleRaft: (a) Front view; (b) 3D view.

Here, only a small number of other-type WECs were listed. With the increasing attention to WECs, novel WECs are being developed by researchers. Besides, some reviews of the technical principle, design, and status of WECs can be found in Falcão (2010), Rusu and Onea (2016), Aderinto and Li (2018), and Zhang et al. (2021), The potential synergies of WECs and other structures were reviewed by Clemente et al. (2021). The geometry optimization of WECs was reviewed by Garcia-Teruel and Forehand (2021).

1.2 Numerical Studies on Bottom-Hinged OWSCs

1.2.1 BEM

The hydrodynamics of bottom-hinged OWSCs have been studied experimentally, analytically, and numerically by several scholars in recent years. Some experimental investigations on the motions and power capture of bottom-hinged OWSCs in two-dimensional (2D) wave tanks (Brito et al., 2020b, c; Cho et al., 2020) and three-dimensional (3D) wave basins (Ning et al., 2017; Jiang et al., 2018; Choiniere et al., 2019) were conducted by researchers to understand the OWSC-wave interaction. With the development of cheap and powerful computer hardware, numerical simulation is becoming more popular and there is a rapidly growing number of WEC modeling. Numerical simulations of OWSCs have an advantage of less economic expense, compared to the experiments (Penalba et al., 2017).

Folley et al. (2007a,b) used WAMIT, a boundary element method (BEM) software based on potential flow theory, to study the frequency-domain response of the top-hinged flap and bottom-hinged flap based on potential flow theory, and indicated the effects of water depth, width, and thickness on the hydrodynamic coefficients. Van't Hoff (2009) used WAMIT to calculate hydrodynamic coefficients with good accuracy compared to experiments.

A semi-analytical model, based on frequency-domain BEMM, was developed to calculate the reflection, transmission, and radiation coefficients of OWSCs under regular waves in a channel (Renzi and Dias, 2012) and the open sea (Renzi and Dias, 2013a), neglecting the viscous effects of water. Renzi et al. (2014a) investigated the interaction of a finite array of OWSCs and monochromatic waves. These works were solved only in linear frequency-domain analysis, which assumed a constant hydrostatic restoring stiffness and ignored the viscous drag moment without considering the friction induced by the power take-off (PTO) system.

The purely linear BEM generally overestimates the OWSC motion response and capturing power. A nonlinear frequency-domain model including a quadratic drag torque which was derived from the Morison equation (Morison et al., 1950) and linearized by the Lorentz linearization (Zimmerman, 1982) was utilized in the hydrodynamics of OWSCs (Tom et al., 2016), calculating the fluid drag by a given drag coefficient. Li and Yu (2012) reported that the BEM results were apparently affected by the selection of drag coefficient, especially around resonance. Bhinder et al. (2012) empirically estimated the drag coefficients and found less than 4% power loss caused by viscous force for the heaving buoy, but up to 34% for the flap-type device. Therefore, carefully selecting a drag coefficient in the BEM-based method is critical, especially for the resonant research of OWSC, a flap-type absorber.

Based on the time-domain BEM, the nonlinearity of the PTO system (i.e., the nonlinear relationship between the damping and rotating angle) and quadratic viscous drag of a 2D OWSC were involved in the structural motion equation (Cheng et al., 2019). However, Renzi et al. (2014b) theoretically explained that a simplified 2D model underestimated the capturing power because the diffraction effects dominated the wave force. This means that 3D hydrodynamic analysis is required for the performance evaluation of OWSCs. The time-domain method incorporating fluid viscous drag and nonlinear PTO systems was employed by Gomes et al. (2015) for power extraction of 3D OWSCs under regular and irregular waves, without considering the modification of the wave spectrum in shallow water, in which most of the proposed OWSCs will be installed.

Some other BEM-based hydrodynamic studies of OWSCs can be found in Cummins and Dias (2017), Magkouris et al. (2020), and Cheng et al. (2020). BEM has the merit of efficient computation, but the nonlinearities, e.g., wave breaking (Galvin, 1972), flow separation (Maskell, 1955), vortex shedding (King, 1977), slamming (Wei et al., 2016), and wave overtopping, cannot be perfectly considered.

1.2.2 RANS

Based on Reynolds-averaged Navier-Stokes (RANS), the computational fluid dynamics (CFD) can consider comprehensive nonlinearities, e.g., viscous effects, slamming, and overtopping. The CFD-based NWT has been widely applied in the high-fidelity modeling of the interaction between waves and the motion of OWSCs (Schmitt and Elsaesser, 2015; Schmitt et al., 2016a; Benites-Munoz et al., 2020) and other types of WECs (Windt et al., 2018b). A study by Wei et al. (2015) used Fluent to model the wave interaction with a surface-piercing OWSC, including the wave elevation as well as the spatial and temporal pressure distribution on the OWSC surface. Schmitt and Elsaesser (2015,2017) modeled the motion of OWSCs using OpenFOAM and proved that the Froude scaling was appropriate due to the limited effect of viscosity. Loh et al. (2016) used OpenFOAM with 2D and 3D methods to model the fully submerged OWSC and calibrated the numerical results with the experiments.

The OWSC motions under waves could be simulated based on some dynamic mesh approaches, e.g., mesh distortion method (Schmitt et al., 2012b), dynamic layering method (Wei et al., 2015), arbitrary mesh interface (Schmitt and Elsaesser, 2015), and overset mesh (Liu et al., 2022a). A fictitious domain method without grid motion was used in Mottahedi et al. (2018) to simulate the OWSC motion.

A smoothed particle hydrodynamics (SPH) method, a purely Lagrangian meshless interpolation method (Monaghan, 1994), was adopted by Rafiee et al. (2013) to study wave loads, and the numerical model was validated with relevant experiments. Some SPH-based numerical simulations of the wave interaction with rectangular OWSCs were performed by Zhang et al. (2018), Brito et al. (2020a), Liu et al. (2020), and Wang and Liu (2021).

The details of these approaches (BEM, CFD, and SPH) were comparatively summarized in Penalba et al. (2017) and Dias et al. (2017). The RANS can successfully simulate overall nonlinear effects but with the significant disadvantage of inefficient computation. Long-term motion modeling is not feasible for wide parameters studies due to the high computational costs.

Syncretizing the advantages of BEM and CFD, Liu et al. (2022a,b) implemented a few high-fidelity CFD simulations to calibrate the constant drag coefficients in BEM-based nonlinear models, adequate for different periods. The calibrated nonlinear BEM, which balances computational accuracy and efficiency, agrees with qualitative and quantitative studies.

1.3 Objectives

This doctoral dissertation deduced the nonlinear dynamic equations of bottom-hinged OWSCs under shoaling regular and irregular waves in both frequency-domain and time-domain BEM methods. The irregular wave spectral values in shallow water were corrected according to the water depth. With a time-varying wet surface, the nonlinear hydrostatic restoring moment and nonlinear drag moment were considered, as well as the nonlinear PTO friction moment. The drag coefficients were calibrated with CFD simulations in OpenFOAM.

Taking an Oyster 800-like OWSC as the study model, the resonant behaviors, and performance enhancement via resonant adjustment were discussed. The relationship between maximal CWR and resonance was interpreted. The fittest PTO control strategy was found for each wave state to maximize the wave absorption.

An assembling OWSC for the target wave energy farm around Japan was designed. The MOGA optimization of OWSC sizes and PTO parameters was conducted with two objective functions: maximizing the hydrodynamic performance and minimizing the structural mass per unit width. The effects of various design parameters were comprehensively discussed, and the most sensitive parameter was found.

2 Description of Nearshore Environments

2.1 Incident Wave Elevation and Power

Incident wave elevation at an arbitrary position, in the absence of flap, can be expressed by a sine function for regular waves, or the summarization of multi-components of sinusoidal waves for irregular waves:

$$\eta(t) = \begin{cases} A_i \cos(kx - \omega t) & \text{Regular waves} \\ \sum_{n=1}^{N_w} A(\omega_n) \cos[k_n x - \omega_n t + \phi(\omega_n)] & \text{Irregular waves} \end{cases} \tag{2-1}$$

where A_i is the incident wave amplitude of a regular wave and $A(\omega_n)$ is the wave amplitude of the nth wave component of an irregular wave; k is the wave number for a finite depth and functionally related to the dispersion relation $\omega^2 = gk\tanh(kd)$; k_n is the wave number of the nth wave component; g is the gravity acceleration; ω and ω_n are the angular frequencies; t is the time; N_w is the number of wave components; $\phi(\omega_n) \in [0,2\pi]$ is the random phase.

For irregular waves, $A(\omega_n)$ is determined by the wave spectrum,

$$A(\omega_n) = \sqrt{2S_d(\omega_n)\Delta\omega} \tag{2-2}$$

where Δω is the wave frequency interval of wave components; $S_d(\omega_n)$ is the irregular wave spectrum at water depth d, discussed in the Section 2.2.4.

The incident wave power of the resource per unit width P_w of regular and irregular waves at a finite depth d is given by Newman (2018),

$$P_w = \begin{cases} \frac{1}{2}\rho g {A_i}^2 C_g(\omega) & \text{Regular waves} \\ \rho g \int_0^\infty C_g(\omega) S_d(\omega) d\omega & \text{Irregular waves} \end{cases} \tag{2-3}$$

where $C_g(\omega)$ is the wave group velocity at water depth d,

$$C_g(\omega) = \frac{\omega}{2k}\left[1 + \frac{2kd}{\sinh(2kd)}\right] \tag{2-4}$$

In depth water, $kd \to \infty$ and $C_g(\omega) = \omega/2k$.

2.2 Irregular Waves and Shoaling Correction

2.2.1 Bretschneider-Mitsuyasu Spectrum

Bretschneider (1959) suggested a formula of wave spectrum for wind-generated gravity waves, and the coefficients were adjusted by Mitsuyasu (1970). The modified formula, called the Bretschneider-Mitsuyasu spectrum, is given by a form of angular frequency (in rad/s),

$$S_{BM}(\omega) = 4.112\pi^4 \frac{H_{1/3}^2}{T_{1/3}^4} \frac{1}{\omega^5} \exp\left(-\frac{16.48\pi^4}{T_{1/3}^4 \omega^4}\right) \tag{2-5}$$

where $H_{1/3}$ and $T_{1/3}$ are respectively the significant wave height and its period. The spectral peak period T_p was correlated to $T_{1/3}$ as $T_p = 1.05\, T_{1/3}$.

2.2.2 Pierson-Moskowitz Spectrum

Pierson-Moskowitz spectrum (Pierson and Moskowitz, 1964) is a well-known spectrum for fully developed wind waves, but the initial spectrum function was related to the wind speed. A new form (Faltinsen, 1990) was given by (in rad/s),

$$S_{PM}(\omega) = 4\pi^3 \frac{H_{1/3}^2}{T_0^4} \frac{1}{\omega^5} \exp\left(-\frac{16\pi^3}{T_0^4 \omega^4}\right) \tag{2-6}$$

where T_0 is the mean zero-crossing wave period, and agrees to $T_{1/3} = 1.086\, T_0$ and $T_p = 1.408 T_0$.

2.2.3 JONSWAP Spectrum

Unlike a fully developed spectrum, the Joint North Sea Wave Project (JONSWAP) developed a peak-enhanced spectrum (Hasselmann et al., 1973). Later, an adjusted JONSWAP spectrum was given by Goda (1988),

$$S_J(\omega) = 16\beta_J \pi^4 \frac{H_{1/3}^2}{T_P^4} \frac{1}{\omega^5} \exp\left(-\frac{20\pi^4}{T_p^4 \omega^4}\right) \cdot \gamma^{\exp\left[-(T_p\omega/2\pi - 1)^2/2\sigma^2\right]} \tag{2-7}$$

where

$$\beta_J \approx \frac{0.06238(1.094 - 0.01915 ln\, \gamma)}{0.230 + 0.0336\gamma - 0.185(1.9 + \gamma)^{-1}} \tag{2-8}$$

$$T_{1/3} \approx [1 - 0.132(\gamma + 0.2)^{-0.559}] T_p \tag{2-9}$$

$$T_0 \approx [1 - 0.532(\gamma + 2.5)^{-0.569}]T_p \tag{2-10}$$

$$\sigma = \begin{cases} 0.07, & \omega \leq \omega_p \\ 0.09, & \omega > \omega_p \end{cases} \tag{2-11}$$

where $\gamma \in [1, 7]$ is called the peak enhancement factor with a mean value of 3.3 (Hasselmann et al., 1973); $\omega_p = 2\pi/T_p$ is the peak frequency.

The typical spectral shapes of the Bretschneider-Mitsuyasu spectrum, Pierson-Moskowitz spectrum and JONSWAP spectrum in the same sea state $H_{1/3} = 1.8\,m$ and $T_{1/3} = 6.71\,s$ (the most frequent condition in the target wave energy farm in Chapter 8) are shown in Fig. 2-1. It is found that JONSWAP spectrum has the largest peak value and the peak frequency of Pierson-Moskowitz spectrum is slightly smaller than other two spectrums.

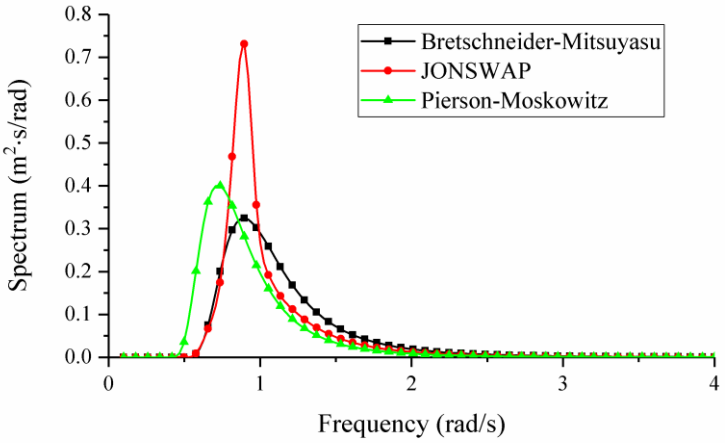

Fig. 2-1 Comparison among Bretschneider-Mitsuyasu spectrum, Pierson-Moskowitz spectrum, and JONSWAP spectrum for infinite depth.

2.2.4 Modification of Wave Spectrum in Shallow Water

For intermediate depth, the spectrum should be modified, referred from Kitaigordskii et al. (1975). The modified wave spectrum was given by

$$S_d(\omega) = S(\omega) \cdot \varphi_k(\omega, d) \tag{2-12}$$

where $S(\omega)$ is the selected wave spectrum; $\varphi_k(\omega, d)$ is the Kitaigorodskii's factor, only related to the frequency and water depth,

$$\varphi_k(\omega, d) = \frac{k(\omega, d)^{-3} \cdot \partial k(\omega, d)/\partial\omega}{k(\omega, \infty)^{-3} \cdot \partial k(\omega, \infty)/\partial\omega} \tag{2-13}$$

where $k(\omega, d)$ is the wave number of frequency ω at water depth d, which is functionally related to the dispersion relation mentioned above; $k(\omega, \infty)$ is the wave number at infinite depth.An example of the comparison between Bretschneider-Mitsuyasu spectrum for infinite depth and the modified spectrum when $H_{1/3} = 1.8$ m and $T_{1/3} = 6.71$ s for 10–40 m water depths is shown in Fig. 2-2. It is noted that the modified spectral values for 40m deep water are nearly close to the original spectrum at infinite depth. As the water depth reduces, the values of the modified spectrum decrease significantly around peak frequency.

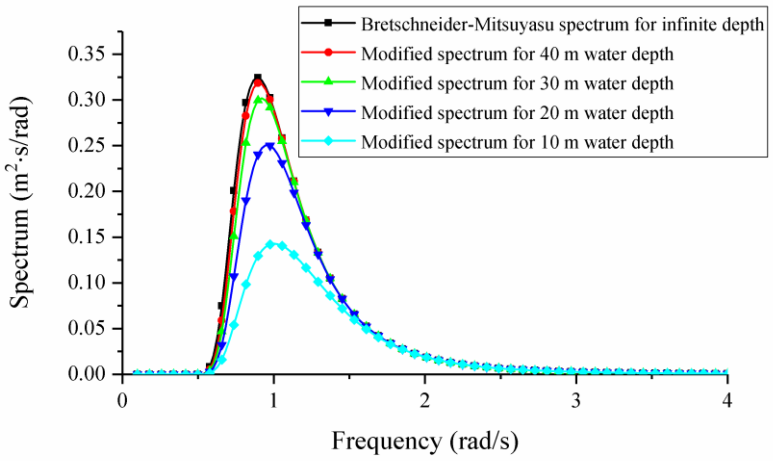

Fig. 2-2 An example of the modified wave spectrum for various water depths.

2.2.5 TMA Spectrum

The TEXEL-MARSEN-ARSLOE (TMA) spectrum was a finite-depth wave spectrum, gained from the produce of infinite-water-depth JONSWAP spectrum and depth-dependent function. The expression of TMA spectrum was given by Bouws et al. (1985),

$$S_{TMA}(\omega) = \alpha_{TMA} \frac{g^2}{\omega^5} \exp\left\{-\frac{20\pi^4}{T_p^4 \omega^4} + \ln\gamma \exp\left[-\left(T_p\omega/2\pi - 1\right)^2/2\sigma^2\right]\right\} \cdot \varphi_{TMA}(\omega, d) \qquad (2\text{-}14)$$

where α_{TMA} is a variable coefficient and $\varphi_{TMA}(\omega, d)$ is the depth-dependent function, the expression of which can be found in Hughes (1984).

In this study, JONSWAP spectrum was utilized in Chapters 5–7, and Bretschneider-Mitsuyasu spectrum was adopted in Chapter 8 because of the wide application in the target wave energy farm around Japan.

2.3 Current and Wind

The descriptions of ocean current and wind can be found in Newman (2018). This study focused the nearshore structures and ignored the effects of current and wind.

3 BEM-Based Mathematical Model of OWSCs

3.1 Environmental Loads

A 3D bottom-hinged OWSC, often called a flap, of width w, thickness b, and height h, captures wave power by oscillating about a horizontal hinge H, fixed to a base constructed on the seabed at water depth d, as shown in Fig. 3-1. The distance between the axis and the still water surface is d_a, called the axis depth. If $d_a \geq h$, the flap is fully submerged, but the top of the flap may emerge out of the water when a wave trough approaches. As the water level decreases to $d_a < h$, the flap is a surface-piercing flap, the height of which above still water is $h_f = h - d_a$, referred to as freeboard. Points B and G are, respectively, buoyant center and gravity center. φ is the rotational angle. $\dot{\varphi}$ and $\ddot{\varphi}$ are angular velocity and acceleration, respectively.

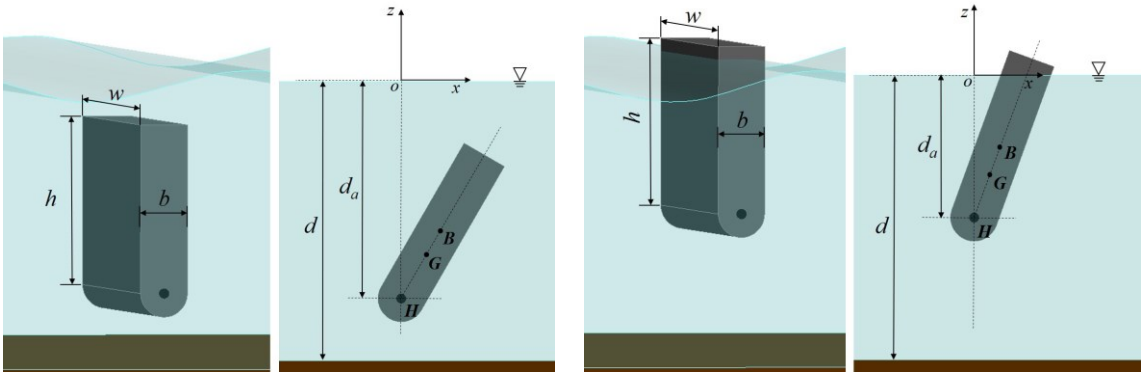

Fig. 3-1 An illustration of: (a) A fully submerged OWSC; (b) A surface-piercing OWSC.

The wave propagation direction is assumed to be unidirectional, and perpendicular to the flap (x-axis of a Cartesian coordinate system), which is an ideal scenario. Some studies on different types of coastal structures, such as low-crested structures (van der Meer et al., 2005) and dikes (van der Werf and van Gent, 2018), demonstrated a significant reduction in wave overtopping and the wave-induced forces in relative non-normal angles between the structures and the waves (e.g., oblique waves or skewed structures). Although the effects of oblique waves are not negligible, the research of OWSCs under perpendicular waves in this work is still meaningful as the foundation for future studies, comparing the influence of oblique waves with perpendicular waves.

The incident waves are not allowed very high, based on the assumption of a linear relationship between wave amplitude and wave exciting moment amplitude. In addition, some

nonlinearities, such as wave breaking, wave overtopping, flow separation, vortex shedding, and slamming, cannot be taken into account in BEM-based methodology. However, viscous drag will be simply considered (see Section 3.1.4).

3.1.1 Wave Exciting Moment

The wave exciting moment $M_E(t)$, including the Froude–Krylov moment and the diffraction moment for a 3D model, can be described as

$$M_E(t) = \begin{cases} M_e(\omega)A_i \ cos[-\omega t + \psi(\omega)] & \text{Regular waves} \\ \sum_{n=1}^{N_w} M_e(\omega_n)\, A(\omega_n) \ cos[-\omega_n t + \phi(\omega_n) + \psi(\omega_n)] & \text{Irregular waves} \end{cases} \tag{3-1}$$

where $M_e(\omega)$ is the wave exciting moment amplitude for unit wave amplitude, and $\psi(\omega)$ is the phase difference between the incident wave and the wave exciting moment.

3.1.2 Radiation Damping Moment

In frequency-domain analysis, the linear hydrodynamic radiation moment can be written as

$$M_R(\omega) = -\mu(\omega)\ddot{\varphi} - c(\omega)\dot{\varphi} \tag{3-2}$$

where $\mu(\omega)$ and $c(\omega)$ are the frequency-dependent added inertia torque and radiation damping, respectively.

Based on the Cummins equation (Cummins, 1962) and the convolution integral (Jefferys, 1984), the time-domain radiation damping moment $M_R(t)$, incorporating the effects of wave-making memory, is given by

$$M_R(t) = -\mu(\infty)\ddot{\varphi}(t) - \int_0^t R(t-\tau)\,\dot{\varphi}(\tau)d\tau \tag{3-3}$$

where $\mu(\infty)$ is the added inertia torque at infinite frequency; $R(t)$ is the impulse response function,

$$R(t) = \frac{2}{\pi}\int_0^\infty c(\omega) \ cos(\omega t)d\omega \tag{3-4}$$

where $c(\omega)$ is the radiation damping coefficient.

3.1.3 Hydrostatic Restoring Moment

The nonlinear hydrostatic restoring moment $M_H(t)$ can be described as

$$M_H(t) = -K_H(t)\varphi(t) \tag{3-5}$$

where $K_H(t)$ is the hydrostatic stiffness.

$$K_H(t) = \begin{cases} K_{mean}(t) & \text{Mean wet surface} \\ K_{instant}(t) & \text{Instantaneous wet surface} \end{cases} \tag{3-6}$$

Based on the simplification of the mean wet surface under waves, the hydrostatic stiffness can be written as

$$K_{mean}(t) = \begin{cases} K_0 \cdot \dfrac{sin\,\varphi(t)}{\varphi(t)}, & \varphi(t) \neq 0 \\ K_0, & \varphi(t) = 0 \end{cases} \tag{3-7}$$

where K_0 is the initial stiffness when the flap is undisturbed in still water,

$$K_0 = F_b \cdot \overline{BH} - mg \cdot \overline{GH} \tag{3-8}$$

where ρ is the water density; m is the mass; g is the gravitational acceleration; $\overline{GH}$ is the force arm of gravity; F_b and $\overline{BH}$ are the constant buoyant force and its force arm, respectively, in the vertical position.

$$F_b = \rho g w \left(d_a b + \frac{\pi b^2}{8} \right) \tag{3-9}$$

$$\overline{BH} = \frac{12 d_a^2 - 2b^2}{24 d_a + 3\pi b} \tag{3-10}$$

Eq. (3-7) ignored the effects of wet surface variation and might produce inaccurate results. To consider the instantaneous wet surface, the hydrostatic stiffness can be given by

$$K_{instant}(t) = \begin{cases} \left[F_b(t) \cdot \overline{BH}(t) - mg \cdot \overline{GH} \right] \cdot \dfrac{sin\,\varphi(t)}{\varphi(t)}, & \varphi(t) \neq 0 \\ F_b(t) \cdot \overline{BH}(t) - mg \cdot \overline{GH}, & \varphi(t) = 0 \end{cases} \tag{3-11}$$

where $F_b(t)$ is the time-varying buoyant force and $\overline{BH}(t)$ is its force arm.

$M_H(t)$ depends on the calculation of wet surface. Based on different assumptions, Chapters 5–8 employed different expressions of $K_H(t)$, for example, $K_{instant}(t)$ in Eq. (3-11) was

applied in Chapter 6; $K_{mean}(t)$ in Eq. (3-7) was used in Chapter 7; Chapters 5 and 8 introduced the sum of a small-angle stiffness and an additional stiffness to take the instantaneous wet surface into account.

3.1.4 Drag Moment

In the realistic physical model, the drag moment is complex. However, in the current mathematical model, as evolved from the Morison equation (Morison et al., 1950), the nonlinear drag moment $M_D(t)$ acting on the wet surface (below the corrected wave surface) can be simply expressed as

$$M_D(t) = -\frac{1}{2} C_d \rho w \int_0^{h_w(t)} [\dot{\varphi}(t) r - u_n(t)] \cdot |\dot{\varphi}(t) r - u_n(t)| \cdot r dr \tag{3-12}$$

where C_d is the drag coefficient; $h_w(t)$ is time-varying wet surface height along the flap mid-surface regardless of the difference of wet surface between the landward and seaward sides, described in Chapters 5–8; r is the radial coordinate of the flap based on the hinge; $u_n(t)$ is the normal velocity of the water particles (in the absence of the flap) on the mid-surface of the flap, and is given by

$$u_n(t) = u_x(t)\ cos\,\varphi(t) - u_z(t)\ sin\,\varphi(t) \tag{3-13}$$

where $u_x(t)$ and $u_z(t)$ are, respectively, the horizontal and vertical components of the water particle velocities in the absence of the flap at a finite depth (Newman, 2018),

$$u_x(t) = \begin{cases} \dfrac{gkA_i}{\omega} \dfrac{cosh[k(z+d)]}{cosh(kd)}\ cos(kx - \omega t) & \text{Regular waves} \\ \displaystyle\sum_{n=1}^{N_w} \dfrac{gk_nA(\omega_n)}{\omega_n} \dfrac{cosh[k_n(z+d)]}{cosh(k_nd)}\ cos[k_nx - \omega_n t + \phi(\omega_n)] & \text{Irregular waves} \end{cases} \tag{3-14}$$

$$u_z(t) = \begin{cases} \dfrac{gkA_i}{\omega} \dfrac{sinh[k(z+d)]}{cosh(kd)}\ sin(kx - \omega t) & \text{Regular waves} \\ \displaystyle\sum_{n=1}^{N_w} \dfrac{gk_nA(\omega_n)}{\omega_n} \dfrac{sinh[k_n(z+d)]}{cosh(k_nd)}\ sin[k_nx - \omega_n t + \phi(\omega_n)] & \text{Irregular waves} \end{cases} \tag{3-15}$$

3.1.5 PTO Moment

López et al. (2017) found that the friction induced by the mechanical losses in the PTO system, including sliding and bearing friction, backlash, and structural flexibility cannot be

ignored. If considering the mass, the stiffness, the damping, and the friction of the PTO system, the total moment of the PTO system M_{PTO} is given by

$$M_{PTO}(t) = -I_{PTO}\ddot{\varphi}(t) - C_{PTO}\dot{\varphi}(t) - K_{PTO}\varphi(t) - M_f(t) \tag{3-16}$$

where C_{PTO} is the damping of the PTO system for wave energy harvesting; I_{PTO} and K_{PTO} are, respectively, the PTO inertia torque and stiffness for adjusting the natural period of OWSCs; $M_f(t)$ is the friction moment against the flap motion,

$$M_f(t) = \begin{cases} T_{PTO}, & \dot{\varphi}(t) > 0 \\ 0, & \dot{\varphi}(t) = 0 \\ -T_{PTO}, & \dot{\varphi}(t) < 0 \end{cases} \tag{3-17}$$

where T_{PTO} is a constant value of PTO friction torque.

3.2 Frequency-Domain Analysis

3.2.1 Under Regular Waves

In linear approximation, the harmonic responses in the pitch degree of freedom, are given by

$$\varphi(\omega) = \varphi_0 \sin(\omega t + \theta) \tag{3-18}$$

$$\dot{\varphi}(\omega) = \omega\varphi_0 \cos(\omega t + \theta) \tag{3-19}$$

$$\ddot{\varphi}(\omega) = -\omega^2\varphi_0 \sin(\omega t + \theta) \tag{3-20}$$

where φ_0 is the pitch amplitude of motion; θ is the phase difference between the incident wave and the response.

3.2.1.1 Dynamic Equation

The frequency-domain method is applicable for the bodies oscillating under regular waves. The dynamic equation for the pitch motion of a bottom-hinged OWSC can be expressed as

$$I_H\ddot{\varphi}(\omega) = M_E(\omega) + M_R(\omega) + M_H(\omega) + M_D(\omega) + M_{PTO}(\omega) \tag{3-21}$$

where I_H is the pitch mass moment of inertia about the hinged axis, $I_H = I_G + m \cdot \overline{GH}^2$, where I_G is the pitch mass moment of inertia about the gravity center; $M_E(\omega)$, $M_R(\omega)$, $M_H(\omega)$, $M_D(\omega)$, and $M_{PTO}(\omega)$ are the ideally harmonic wave exciting moment, radiation damping

moment, hydrostatic restoring moment, drag moment, and PTO moment in frequency-domain form.

Under regular waves, $M_E(\omega)$ can be given by

$$M_E(\omega) = M_e(\omega)A_i \ cos[-\omega t + \psi(\omega)] \tag{3-22}$$

It is observed from Eqs. (3-22), (3-2), (3-5), (3-12), and (3-16) that $M_E(\omega)$ and $M_R(\omega)$ are harmonic, but $M_H(t)$, $M_D(t)$, and $M_{PTO}(t)$ are not sinusoidal function. To obtain the sinusoidal forms of these loads, linearization is required.

3.2.1.2 Linearization of Hydrostatic Stiffness

According to energy conservation during the one wave period with the flap moving from 0 to the maximum angle, the nonlinear stiffness can be linearized as the constant value of K_{HL} in each wave condition, assuming that the linearized stiffness moment produces the same work as the real nonlinear stiffness moment during the one wave period,

$$\int_0^T |M_H(t) \cdot \dot{\varphi}(t)|dt = K_{HL} \int_0^T |\varphi(t) \cdot \dot{\varphi}(t)|dt \tag{3-23}$$

where T is the regular wave period and K_{HL} is the linearized hydrostatic stiffness. For a given flap, K_{HL} is a series of constant values only dependent on the wave and PTO conditions.

Once $M_{\mathrm{H}}(t)$ in a duration is obtained, K_{HL} can be obtained from Eq. (3-23).

$$K_{HL} = \frac{\int_0^T |M_H(t) \cdot \dot{\varphi}(t)|dt}{2\varphi_0^2} \tag{3-24}$$

Within a wave period, the non-sinusoidal $M_H(t)$ can be expressed as a linearized frequency-domain form for a given wave condition.

$$M_H(\omega) = -K_{HL}\varphi(\omega) \tag{3-25}$$

3.2.1.3 Linearization of Drag Moment

According to energy conservation in one wave cycle, the nonlinear drag moment can be linearized (Zimmerman, 1982) as the constant value of linearized viscous damping C_{DL} for each wave condition, assuming that the linearized moment is equivalent to the real quadratic moment over one wave cycle,

$$\int_o^T -M_D(t)\cdot\dot{\varphi}(t)dt = C_{DL}\int_0^T \dot{\varphi}^2(t)dt \tag{3-26}$$

It should be noted that $M_D(t)$ is strongly related to the pitch amplitude φ_0 and the phase angle θ. The linearized drag damping C_{DL} can be obtained from Eq. (3-26).

$$C_{DL} = \frac{\int_o^T -M_D(t)\cdot\dot{\varphi}(t)dt}{\omega\pi\varphi_0^2} \tag{3-27}$$

Within a wave period, the non-sinusoidal $M_D(t)$ can be expressed as a linearized frequency-domain form.

$$M_D(\omega) = -C_{DL}\dot{\varphi}(\omega) \tag{3-28}$$

3.2.1.4 Linearization of PTO Friction moment

Assuming the same work produced by the linearized friction moment as the nonlinear friction moment over one wave cycle, the nonlinear friction moment T_{PTO} can be linearized as

$$C_{PTOL} = -\frac{4T_{PTO}}{\omega\pi\varphi_0} \tag{3-29}$$

where C_{PTOL} is the linearized PTO damping. Within a wave period, non-sinusoidal $M_{PTO}(t)$ can be given as a linearized frequency-domain form.

$$M_{PTO}(\omega) = -I_{PTO}\ddot{\varphi}(\omega) - (C_{PTO} + C_{PTOL})\dot{\varphi}(\omega) - K_{PTO}\varphi(\omega) \tag{3-30}$$

3.2.1.5 Solution of Dynamic Equation

Substituting Eqs. (3-20), (3-22), (3-2), (3-25), (3-28), and (3-30) into Eq. (3-21), the dynamic equation can be transferred into the frequency-domain form,

$$[(K_{HL} + K_{PTO}) - (\Delta I + I_{PTO})\omega^2 + i(\Delta C + C_{PTO})\omega]\varphi_0 = M_e(\omega)A_i \tag{3-31}$$

where ΔI is the inertia torque except I_{PTO}, and ΔC is the damping except C_{PTO}.

$$\Delta I = I_H + \mu(\omega) \tag{3-32}$$

$$\Delta C = c(\omega) + C_{DL} + C_{PTOL} \tag{3-33}$$

The solution of the dynamic equation is given by

$$\varphi_0 = \frac{M_e(\omega)A_i}{\sqrt{[(K_{HL}+K_{PTO})-(\Delta I+I_{PTO})\omega^2]^2+[(\Delta C+C_{PTO})\omega]^2}} \tag{3-34}$$

The phase angle of pitch relative to wave exciting moment is given by

$$\theta_1 = -arctan\left[\frac{(\Delta C+C_{PTO})\omega}{(K_{HL}+K_{PTO})-(\Delta I+I_{PTO})\omega^2}\right] \tag{3-35}$$

where $\theta_1 \in [-\pi, 0]$. The phase of response can be calculated by

$$\theta = \theta_1 - \psi(\omega) + \pi/2 \tag{3-36}$$

The phase angle of angular velocity relative to wave exciting moment is often used in the judgment of resonance and given by

$$\theta_2 = \theta_1 + \pi/2 \tag{3-37}$$

where $\theta_2 \in [-\pi/2\,, \pi/2]$.

Table 3-1 presents the phase angles of various items for clear comparison.

Table 3-1 Phase angles of various items for regular waves.

Phase Angle of	Value
Incident wave elevation at $x = 0$	$\pi/2$
Wave exciting moment relative to incident wave elevation	$-\psi(\omega)$
Pitch angle relative to wave exciting moment	θ_1
Angular velocity relative to wave exciting moment	θ_2
Pitch angle	θ

In a generic oscillating system under harmonic excitation, the resonance occurs when $(K_{HL}+K_{PTO})-(\Delta I+I_{PTO})\omega^2 = 0$, i.e., the exciting period T is equal to the natural period,

$$T_n = 2\pi\sqrt{(\Delta I+I_{PTO})/(K_{HL}+K_{PTO})} \tag{3-38}$$

Simultaneously, $\theta_2 = 0$. This resonant phenomenon can be introduced into the enhancement of wave energy absorption of an OWSC and will be described in Chapter 7.

The workflow of solving the dynamic equation is shown in Fig. 3-2. Firstly, the hydrodynamic coefficients $M_e(\omega)$, $\psi(\omega)$, $\mu(\omega)$ and $c(\omega)$ are computed in NEMOH, an open-source frequency domain BEM program. NEMOH was employed in the analysis of OWSCs under waves, and validated via experiments (Schmitt et al., 2016b). For a given wave condition

and PTO system, the values of $K_{HL}(\omega)$ and $C_{PTOL}(\omega)$ are affected by the solution φ_0, and $C_{DL}(\omega)$ is related to the solutions φ_0 and θ. Therefore, a Python code is developed for the iterative computation of linearized items and solutions until reaching the converge criterion, setting as 10^{-6} rad for both φ_0 and θ.

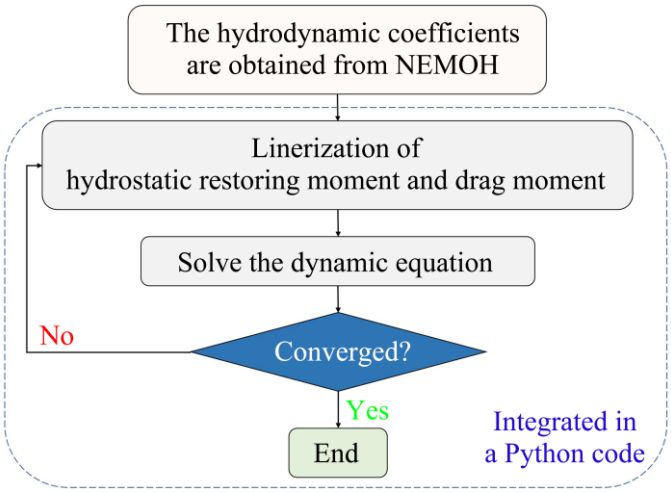

Fig. 3-2 A workflow of iterative computation in frequency-domain.

3.2.2 Under Irregular Waves

Sarkar et al. (2013) stated that the performance of an OWSC under an irregular wave was given by the sum of the average capturing power values for the monochromatic wave components, based on the frequency-domain method.

Under irregular waves, the response spectrum $S_{out}(\omega)$ are formulated by

$$S_{out}(\omega) = \left[\frac{\varphi_0(\omega)}{A_u(\omega)}\right]^2 \cdot S_d(\omega) \tag{3-39}$$

where $A_u(\omega)$ denotes the wave amplitude at frequency ω, and agrees to $A_u(\omega) = A_i = min[1,\ \lambda(\omega)/14]$. It can be either the unit wave amplitude for a long period or the maximum allowable wave amplitude with respect to the limited wave steepness 1/7 for short waves. $\varphi_0(\omega)/A_u(\omega)$ is called the transfer function.

The significant value of pitch can be defined by

$$\varphi_s = 4\sqrt{\int_0^\infty S_{out}(\omega)d\omega} \tag{3-40}$$

The time–history response of pitch can be described by the sum of responses under multiple wave components,

$$\varphi(t) = \sum_{n=1}^{N_w} \sqrt{2S_{out}(\omega_n)\Delta\omega} \cdot sin[\omega_n t + \theta(\omega_n) - \phi(\omega_n)] \tag{3-41}$$

where $\Delta\omega$ is the frequency interval; $\theta(\omega_n)$, referred to Eq. (3-36), is the phase of nth wave component under regular wave; $\phi(\omega_n)$ is the random phase of wave component.

From Eq. (3-39) and Eq. (3-41), it is noted that once $\varphi_0(\omega)/A_u(\omega)$ for various frequencies are obtained, the response spectrum $S_{out}(\omega)$ and time–history pitch response $\varphi(t)$ under an arbitrary irregular wave can be quickly calculated.

3.3 Time-Domain Analysis

In the time-domain analysis, the dynamic equation of the pitch motion can be written as

$$I_H\ddot{\varphi}(t) = M_E(t) + M_R(t) + M_H(t) + M_D(t) + M_{PTO}(t) \tag{3-42}$$

The workflow of solving the dynamic equation is illustrated in Fig. 3-3. For a certain geometry of study model, the forementioned hydrodynamic coefficients and $\mu(\infty)$ can be obtained from NEMOH. According to the inputted wave parameters (e. g., in still water, under regular or irregular waves) and initial conditions of the flap (e. g., at an inclined angle for free decay or at the vertical position under waves), a Python code was developed to implement a time marching computation. In each time step, the process is as follows:

• Using the solutions of angle $\varphi(t)$ and angular velocity $\dot{\varphi}(t)$ at the previous time t, the environmental loads can be calculated by Eqs. (3-1), (3-3), (3-5), (3-12), and (3-16);

• Substitute the values of environmental loads into Eq. (3-42) to assemble a dynamic differential equation;

• By 4th-order Runge–Kutta integration, the hydrodynamic responses of the flap at the current time $(t + dt)$ can be computed, where dt is the time step of integration.

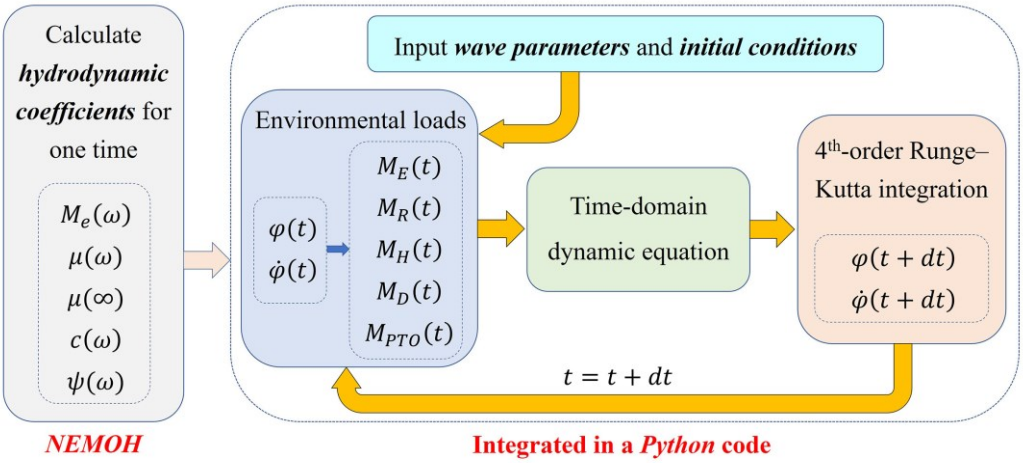

Fig. 3-3 A workflow of solving the dynamic equation in time-domain.

Although the actual time–history response under a regular wave is not perfectly harmonic, an equivalent sinusoidal response, based on energy conservation for a duration, can be introduced as

$$\varphi(t) = \varphi_{amp}\, sin(\omega t + \theta) \tag{3-43}$$

where φ_{amp} is the equivalent pitch amplitude; θ is the phase of the pitch. According to the kinetic energy conservation of equivalent sinusoidal motion with the actual response during the recording time, φ_{amp} can be calculated by

$$\varphi_{amp} = \frac{1}{\omega}\sqrt{\frac{2}{t_e - t_b}\int_{t_b}^{t_e}\dot{\varphi}^2(t)dt} \tag{3-44}$$

where t_b and t_e are, respectively, the beginning and end time for recording angular velocity $\dot{\varphi}(t)$ in a duration.

Then, the equivalent amplitude of angular velocity can be written as

$$\dot{\varphi}_{amp} = \varphi_{amp}\omega \tag{3-45}$$

The phase angle of angular velocity θ_2 relative to the wave exciting moment under regular waves can be estimated by measuring the averaged time difference between peak angular velocity and peak wave exciting moment in the time–history curves,

$$\theta_2 = \frac{2\pi}{N_c T}\sum_{n=1}^{N_c}\left(t_{p,M_E} - t_{p,\dot{\varphi}}\right)_n \tag{3-46}$$

where N_c is the number of peak values after the beginning time t_b; t_{p,M_E} and $t_{p,\dot{\varphi}}$ are, respectively, the time of peak moment and peak angular velocity. The phase angle of pitch relative to the wave exciting moment θ_1 can be obtained, substituting Eq. (3-46) into Eq. (3-37).

To examine the response under irregular waves, according to kinetic energy conservation, the irregular response is also equivalent to the harmonic motion, the period of which is equal to the peak period, and the equivalent pitch amplitude is defined as

$$\varphi_{eq} = \frac{1}{\omega_p}\sqrt{\frac{2}{t_e - t_b}\int_{t_b}^{t_e}\dot{\varphi}^2(t)dt} \tag{3-47}$$

where ω_p is the peak frequency of an irregular wave.

To illustrate the calculation of equivalent pitch amplitude for an irregular wave condition, Fig. 3-4 gives a comparison of actual irregular response and equivalent sinusoidal response. The total kinetic energies for both responses in a given duration are identical. φ_{eq} can be calculated through kinetic energy conservation.

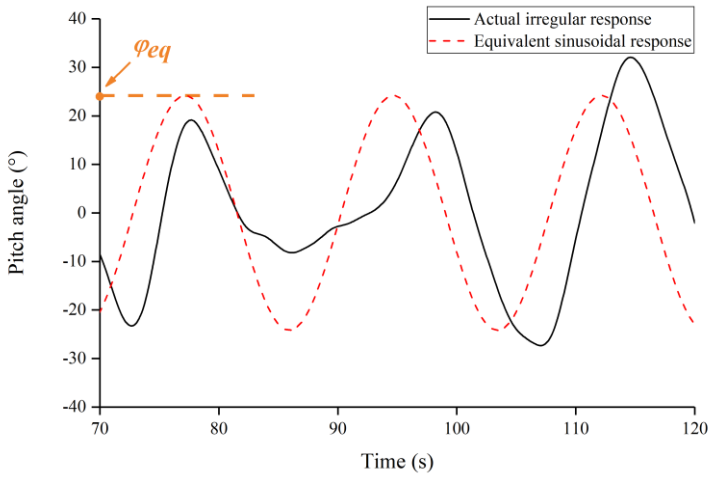

Fig. 3-4 Comparison of actual irregular and equivalent sinusoidal responses.

3.4 Performance Assessment

3.4.1 CWR for a Single Wave Condition

For a single wave condition, regardless of a regular or irregular wave, the time–averaged capturing power P_c is given by

$$P_c = \begin{cases} \frac{1}{2} C_{PTO} \omega^2 \varphi_0^2 & \text{Frequency domain under regular waves} \\ C_{PTO} \int_0^\infty S_{out}(\omega) \cdot \omega^2 d\omega & \text{Frequency domain under irregular waves} \\ \frac{C_{PTO}}{t_e - t_b} \int_{t_b}^{t_e} \dot{\varphi}^2(t) dt & \text{Time domain} \end{cases} \quad (3\text{-}48)$$

The CWR under regular or irregular waves can be expressed as

$$CWR = \frac{P_c}{P_w \cdot w} \quad (3\text{-}49)$$

where w is the OWSC width.

3.4.2 Mean Annual CWR

To estimate the performance of the OWSCs in one year and even longer, the mean annual capturing wave power is recommended and given by

$$P_{ac} = \sum_{T_{1/3}=0}^{\infty} \sum_{H_{1/3}=0}^{\infty} O(H_{1/3}, T_{1/3}) \cdot P_c(H_{1/3}, T_{1/3}) \quad (3\text{-}50)$$

where $O(H_{1/3}, T_{1/3})$ is the percentage occurrence of a sea state.

The mean annual power of wave energy resource per unit width is calculated by

$$P_{res} = \sum_{T_{1/3}=0}^{\infty} \sum_{H_{1/3}=0}^{\infty} O(H_{1/3}, T_{1/3}) \cdot P_w(H_{1/3}, T_{1/3}) \quad (3\text{-}51)$$

The mean annual CWR is given by

$$\eta = \frac{P_{ac}}{P_{res} \cdot w} \quad (3\text{-}52)$$

3.5 BEM Model of an Oyster 800-Like OWSC

Table 3-2 lists the parameters of the research model in Chapters 5–7, a 3D surface-piercing OWSC, of which w, b, h, and d_a are referred to the Oyster 800-like model in Renzi and Dias (2013b). d, I_G, and initial $C_{PTO} = 16\ \text{MN} \cdot \text{m} \cdot \text{s/rad}$ are given in Tay and Venugopal (2017b). Some parameters, $\overline{BH}$ and m, are estimated by the author. $\overline{GH}$ is calculated by the given restoring stiffness at a small rotational angle $K_0 = 12.81\ \text{MN} \cdot \text{m/rad}$ (Tay and Venugopal, 2017b).

Table 3-2 Geometric and physical parameters of study model in Chapters 5–7.

w (m)	b (m)	h (m)	d_a (m)	d (m)	$\overline{GH}$ (m)	$\overline{BH}$ (m)	m (kg)	I_G (kg · m^2)
26	4	10	9	12.5	4.781	3.705	6×10^5	9.1455×10^6

In BEM, to eliminate the effects of initial conditions, $t_b = 24T$ and $t_e = 40T$ for the time–averaged response and CWR, and $N_c = 10$ for the measurement of phases are imposed for regular waves. $t_b = 20T_p$, $t_e = 100T_p$ and $N_w = 100$ for wave components from 0.1 to 4.6 rad/s were employed. To eliminate the effects of random phase, the solutions of equivalent pitch amplitude and CWR for five arrays of random phases have been averaged. The time step is set to $dt = T/200$ for regular waves and $dt = T_p/200$ for irregular waves in Chapters 5–7, confirming the solution steady adequately.

Only the grids on the wet surface should be generated in BEM. The quadrilateral grids are applied, and the element sizes are almost uniform. Three different element sizes (coarse, medium, and fine meshes), as shown in Table 3-3, are tested for mesh independence by comparing the results of the hydrodynamic coefficients, which are calculated by NEMOH on a desktop of 3.4 GHz CPU with 16 processors and 32GB RAM. Unfortunately, NEMOH does not provide the parallel computation with multi-processors. The normalized root mean square error (NRMSE) is utilized to estimate the agreement of the results of a certain mesh configuration (coarse or medium mesh) with the results of fine mesh. In Fig. 3-5, each hydrodynamic coefficient seems to be insensitive to the mesh size. Finally, the medium grids, as shown in Fig. 3-6, are selected for the case studies. The calculated value of added inertia torque at infinite frequency $\mu(\infty) = 28.94 \times 10^6$ kg · m^2.

Table 3-3 Mesh statistics and computational cost (on 1 processor) for three configurations of grids in BEM.

Mesh	Mean cell size (m)	# of Wet Surface Cells Above the Hinge	# of Divisions on the Bottom Round	# of Cells	Computational Cost
Coarse	≈ 0.45	16 × 52 × 23	12	3.9K	≈ 5 h
Medium	≈ 0.35	20 × 65 × 30	16	6.4K	≈ 19 h
Fine	≈ 0.3	24 × 75 × 35	20	8.8K	≈ 49 h

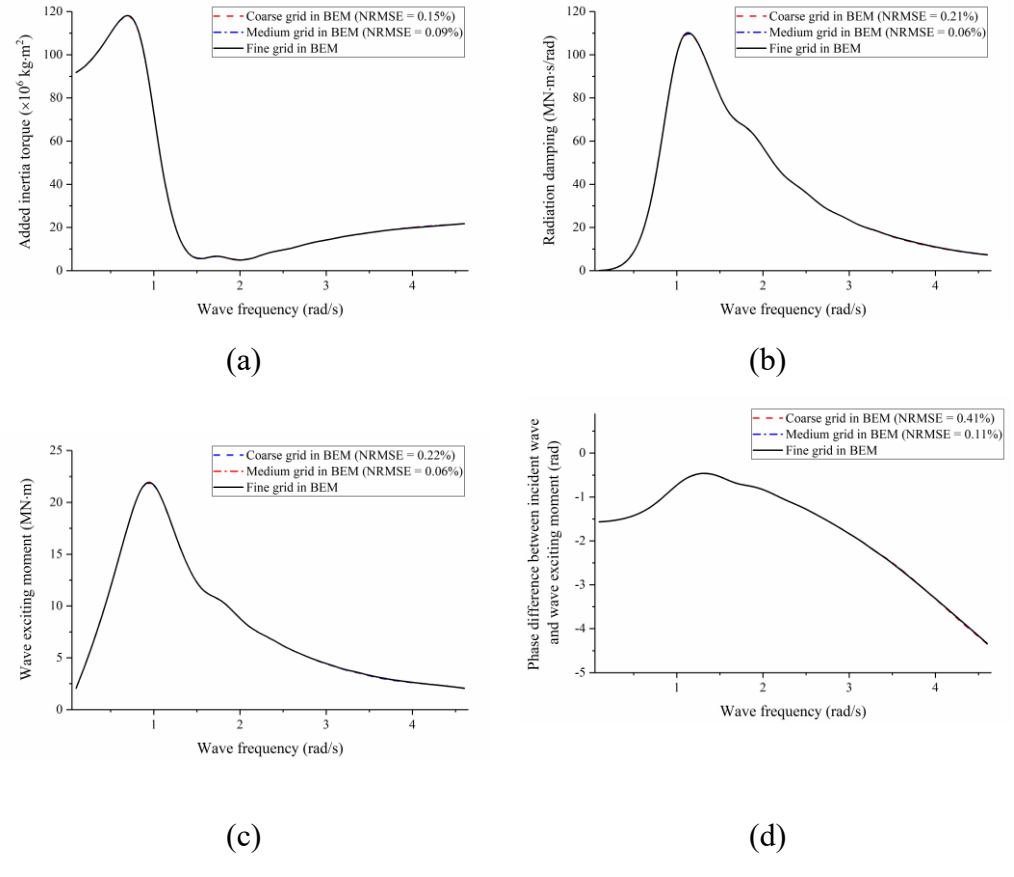

Fig. 3-5 Comparison of the hydrodynamic coefficients under unit-amplitude regular waves for different element sizes in BEM: (a) Added inertia torque; (b) Radiation damping; (c) Wave exciting moment; (d) Phase difference between the incident wave and the wave exciting moment.

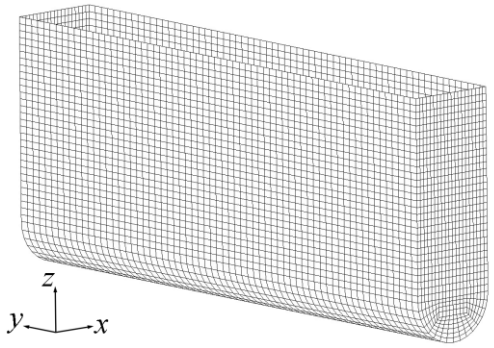

Fig. 3-6 Selected mesh model of mean wet surface input into NEMOH for computation of hydrodynamic coefficients.

3.6 Summarization in the Chapter

The hydrodynamic coefficients were obtained from NEMOH, an open-source frequency-domain BEM program.

In frequency-domain BEM analysis, the pitch-dependent hydrostatic restoring moment, nonlinear drag torque, and nonlinear PTO friction moment were linearized as a constant stiffness, drag damping, and PTO frictional damping, respectively, assuming that the linearized items produce the same work as the realistic nonlinear items during a period. A Python code was developed to iteratively solve the dynamic equations under regular waves, due to the strong coupling between the nonlinear items and the solutions. The response under an irregular wave was calculated by the sum of responses under multiple regular waves.

In time-domain BEM analysis, A Python code with 4th-order Runge–Kutta integration scheme was developed to directly solve the nonlinear dynamic equation, in which various environmental loads are time-varying.

However, the selection of wet surface $h_w(t)$ for calculating $M_H(t)$ and $M_D(t)$ was not determined in this chapter and will be introduced in Chapters 5–8.

4 CFD-Based Numerical Model of OWSCs

4.1 Governing Equations

Based on the assumption of fluid incompressibility, the mass conservation equation for the NWT based on the Volume of Fluid (VOF) method (Hirt and Nichols, 1981) is given by

$$\frac{\partial \rho}{\partial t} + \nabla(\rho \vec{\boldsymbol{v}}) = 0 \tag{4-1}$$

where $\vec{\boldsymbol{v}}$ is the fluid velocity vector; $\rho = (1-\alpha)\rho_1 + \alpha\rho_2$ is the equivalent fluid density, calculated by air density ρ_1, water density ρ_2, and the volume fraction of water α. The equivalent dynamic viscosity μ is also determined by $\mu = (1-\alpha)\mu_1 + \alpha\mu_2$, where μ_1 and μ_2 are the dynamic viscosity of air and water, respectively. The volume fraction can be calculated by the mass conservation equation.

The RANS equation is given by

$$\frac{\partial(\rho \vec{\boldsymbol{v}})}{\partial t} + \nabla(\rho \vec{\boldsymbol{v}}\vec{\boldsymbol{v}}) = -\nabla p + \nabla \vec{\boldsymbol{T}} + \vec{\boldsymbol{S}} \tag{4-2}$$

where p is the pressure; $\vec{\boldsymbol{T}}$ is the stress tensor, including viscous stress and turbulent stress; $\vec{\boldsymbol{S}}$ is the body force per unit mass (such as gravity). For incompressible Newtonian fluids and a turbulent model of eddy viscosity, $\vec{\boldsymbol{T}}$ is defined as

$$\vec{\boldsymbol{T}} = (\mu + \mu_t)[\nabla \vec{\boldsymbol{v}} + (\nabla \vec{\boldsymbol{v}})^T] \tag{4-3}$$

where μ_t is the turbulent viscosity.

The dynamic equation of the flap pitch is written by

$$I_H \ddot{\varphi}(t) = mg \cdot \overline{GH}\, sin\, \varphi(t) + M_{fluid}(t) + M_{PTO}(t) \tag{4-4}$$

where $M_{fluid}(t)$ is the total fluid moment acting on the flap surface, and is obtained by integrating the pressure and shear stress over the fluid–structure interface,

$$M_{fluid}(t) = \int_s (\vec{\boldsymbol{r}}_s - \vec{\boldsymbol{r}}_h) \times \left(\vec{\boldsymbol{T}} - p\vec{\boldsymbol{I}}\right) \cdot \vec{\boldsymbol{n}} ds \tag{4-5}$$

where s is the fluid–structure interface; $\vec{\boldsymbol{r}}_s$ is the position vector of the point on the flap surface; $\vec{\boldsymbol{r}}_h$ is the position vector of the hinge; and $\vec{\boldsymbol{n}}$ is the unit outer-pointing normal vector of the surface elements of the flap.

The motion of the flap and fluid are fully coupled by velocity and pressure on the fluid–structure interface. The velocity on the fluid–structure interface $\vec{\boldsymbol{v}}_S$ is related to the motion of the flap based on the position of the hinge point,

$$\vec{\boldsymbol{v}}_S = \dot{\varphi}(t) \times (\vec{\boldsymbol{r}}_s - \vec{\boldsymbol{r}}_h) \tag{4-6}$$

4.2 Setup in OpenFOAM

The interaction of the flap with waves is simulated by the finite volume method solver overInterDyMFoam in the package OpenFOAM, an open source CFD toolbox.

In order to calibrate the BEM results, some settings in CFD should be same or similar with BEM. Therefore, the Stokes I wave model (corresponding to the linear waves in BEM) is applied for regular waves, and 100 wave components with different wave periods, wave heights, and random phases are utilized for irregular waves. Shallow water wave absorption works on both inlet and outlet.

For simulating the motion of a flap with a potential large amplitude, the overset mesh approach (Windt et al., 2018a) is used. The domain is separated into two zones—a stationary main zone and a moving overset zone. The flap rotation is simulated by the motion of the whole overset zone and the cell volume weight interpolation of velocity, pressure, and volume fraction between the overlapping volume of these two zones. The flap surface is restricted by a hinged axel with a torsional spring-damper (i. e., a joint constraint releasing only *Ry* degree of freedom and a restraint of linear axial angular spring inputting rotational stiffness and damping) to simulate the PTO system.

A turbulence model of eddy viscosity of type standard k-ε (SKE), where k and ε are, respectively, turbulent kinetic energy and dissipation rate, is applied to calculate the turbulent viscosity μ_t, which will be introduced into Eq. (4-3) for the calculation of stress tensor $\vec{\boldsymbol{T}}$. Although the SST k-$omega$ model is widely applied for the simulation of wave–structure interaction (Finnegan and Goggins, 2012; Chen et al., 2017), Wei et al. (2015) compared the variable types of turbulence model and found that the torque on the flap due to the wave force is not sensitive to the turbulence model. Hence, the SKE model is employed in the present study, due to the relatively low computational cost (Wei et al., 2015).

In iterative processing, the pressure field is coupled to the velocity field via the PISO-SIMPLE (PIMPLE) method, a merged algorithm of the Pressure Implicit Splitting Operator

(PISO) (Issa, 1986) and the Semi-Implicit Method for Pressure-Linked Equations (SIMPLE) (Ferziger et al., 2002).

All other numerical solver settings were chosen based on the tutorial case of floating body in ESI OpenCFD Releases OpenFOAM v1912.

4.3 CFD Model of an Oyster 800-Like OWSC

To reduce the computational cost in CFD, one half of the wave basin is built as the computational domain of NWT, as shown in Fig. 4-1a, since the geometry, restriction of the flap, and boundary conditions are symmetric. The lengths of the upstream and downstream in the main zone are set as 5 times the flap width, and the width of the main zone (one half of the full model) is 3 times the flap width. The height of the initial air zone is 11 m. The distance between external cubic surface of the overset zone and the flap surface, $d_{overset}$ as shown in Fig. 4-1b, should contain multi-layer grids. The number of grid layer is defined as N_{GL}. A small value of N_{GL} could result in the divergence of computation due to inaccurate interpolation in the overlapping region. However, for more layers (i. e., a large value of N_{GL}), the implement of dynamic overset grid algorithm (Petra, 2019) in each iteration is time consuming. The influence of the value of N_{GL} will be discussed below.

Due to the expensive computational cost of long-duration modeling, the duration of simulation under regular waves is 5–13 times the length of the wave period, according to the stability of the response. Usually, more cycles in a short wave are necessary. The method of extracting pitch amplitude results in CFD is similar to that in the time-domain BEM when the response is steady. The recording period for the computation of pitch amplitude is the last 1–3 periods in regular waves.

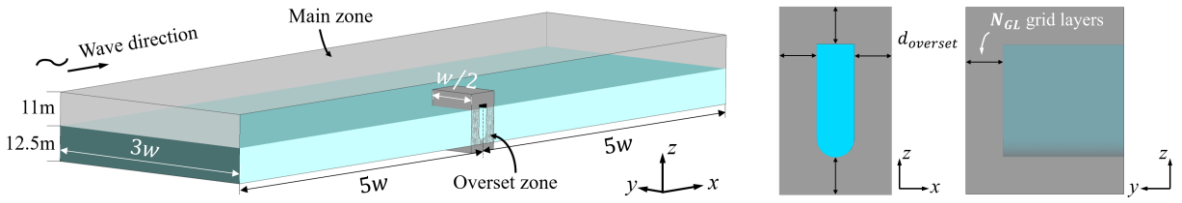

(a) (b)

Fig. 4-1 CFD computational domain: (a) An overall diagram of NWT with a symmetry *x*-*z* plane bisecting the tank; (b) Overset zone with multi-layers of grid between the external cubic surface and the flap surface (in blue).

The mixed grids consisting of cut-cell elements (Causon et al., 2000) for the main zone and hexahedral elements for the overset zone are employed in CFD, as shown in Fig. 4-2. To understand the generation of cut-cell grids, the meshes in the main zone are created as follows:

• The overall Cartesian meshes with almost uniform size are constructed;

• The transition region and refined region (near the water surface and overset zone) are cut off once, and their grid size bisects;

• Cut off the meshes in the refined region again, so the grid size of refined region is a quarter of outermost Cartesian region.

Thus, the grids near the overset zone and the water surface are fine for the accurate simulation of flap motion and wave propagation. The length of refined region in x-direction is set to more than $3h$ to guarantee a larger coverage area than the range of flap motion. The cell size in the overset zone should be approximately same as the grid size in refined region of the main zone, as this will diminish the interpolation error between these two zones (Windt et al., 2018a).

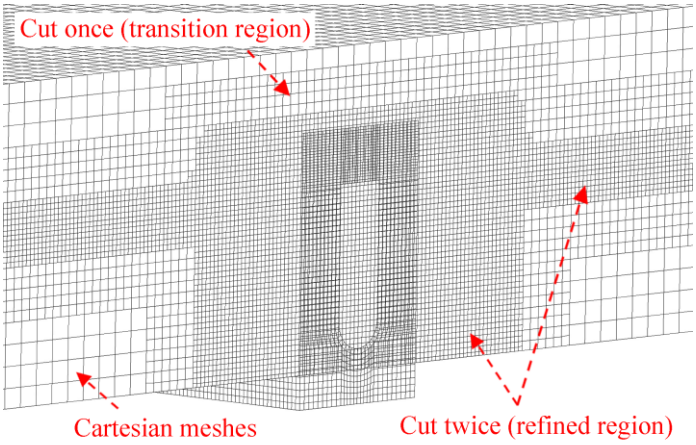

Fig. 4-2 Cut-cell elements in transition region (4–6 grid layers in z-direction) and refined region (12 grid layers in z-direction near the water surface).

In the overset zone, the boundary layer (very fine mesh near the structure surface), which affects the calculation of tangential fluid shear stress on the structure surface, is neglected in this work, because Schmitt et al. (2012a) indicated that the shear forces on the fixed flap calculated are less than 1% of the total surge force. Wei et al. (2015) also suggested that the shear stress is not essential relatively to the normal stress for the prototype OWSC with a large size in width.

Three different element sizes (the number of grid layer between external cubic surface of overset zone and the flap surface is uniformly set to $N_{GL} = 10$), as shown in Table 4-1, are

tested for mesh independence by comparing the wave elevation at 20 m in front of the flap and the time–history total fluid moment $M_{fluid}(t)$ (for 55 s simulation time) on a fixed flap under a representative regular wave ($A_i = 1$ m and $T = 17.5$ s) in CFD. The mean cell sizes of the refined regions for coarse, medium and fine mesh configurations are 0.56 m, 0.41 m and 0.30 m, respectively. Because of the limitation in BEM, the wave height is not allowed very high. With the purpose of calibrating for BEM, the unit-amplitude wave is chosen. The selected wave period is a representative period close to the resonant period of the flap with greatest interests in this study.

Table 4-1 Mesh statistics and computation cost (on 16 processors) for three configurations of grids in CFD.

Mesh	Main Zone			Overset Zone			Total # of Cells	Computational Cost
	# of Water Surface	# of Top & Bottom	# of Cells	# of Flap Surface Above Hinge	# of Divisions on Flap Rounds	# of Cells ($N_{GL} = 10$)		
Coarse	468 × 140	117 × 35	0.94M	12 × 24 × 19	16	34.1K	0.98M	≈ 5 h
Medium	636 × 192	159 × 48	1.96M	16 × 33 × 26	20	58.7K	2.02M	≈ 28 h
Fine	868 × 264	217 × 66	3.83M	20 × 44 × 34	24	88.5K	3.92M	≈ 76 h

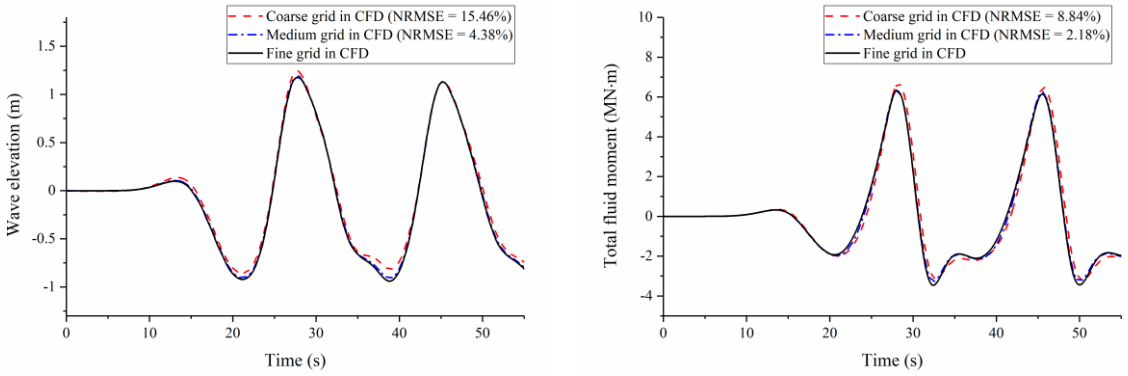

(a) (b)

Fig. 4-3 Comparison of the time–history results for different element sizes in CFD: (a) Wave elevation at 20 m in front of the flap; (b) Total fluid moment on a fixed flap under a representative regular wave.

The NRMSE is applied to estimate the agreement of the results of current mesh with the results of fine mesh. A more than 5% NRMSE related to the results for $A_i = 1$ m and $T = 17.5$ s are found in Fig. 4-3 from a comparison between coarse and fine grids. However, the result for the medium grid is very close to that of the fine grid, in which the total number of elements is almost double of the medium grid. In addition, the computation for medium mesh

is much faster than fine mesh. Accordingly, the medium grids with acceptable accuracy and efficient computation are selected for the case studies.

To assess the influence of the grid layers between the external cubic surface of overset zone and flap surface, four different numbers of grid layer ($N_{GL} = 5$, $N_{GL} = 10$, $N_{GL} = 15$ and $N_{GL} = 20$, as shown in Fig. 4-4) are tested to assess the effects of overset zone dimension. The solver with the current settings cannot produce the converged result of flap motion in the case of 5 layers ($N_{GL} = 5$), possibly caused by the amplified interpolation error.

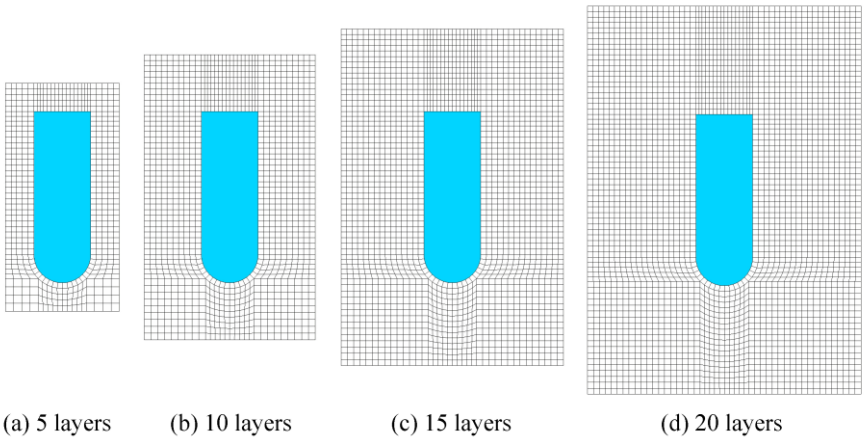

Fig. 4-4 Four different grid layers in overset zone.

The comparison of time–history responses of a flap without a PTO system ($C_{PTO} = 0$ and $T_{PTO} = 0$) under a regular wave ($A_i = 1$ m and $T = 17.5$ s) for 10 layers, 15 layers and 20 layers exhibits a negligible difference, as shown in Fig. 4-5. Similarly, a slight influence of overset zone size can also be found in Windt et al. (2018a).

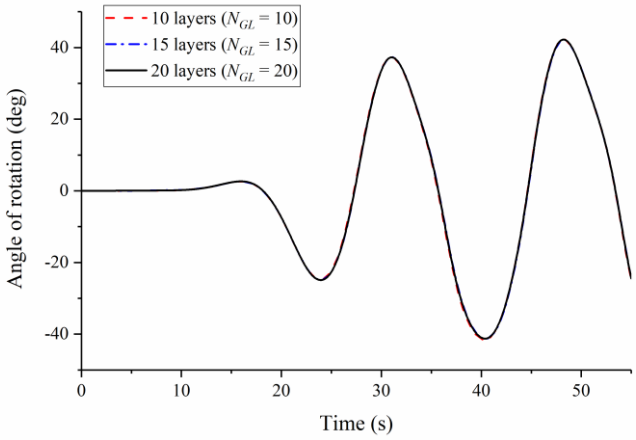

Fig. 4-5 Comparison of time–history responses of a flap without a PTO system under a regular wave among different overset zone sizes.

The computational costs of three different N_{GL} on a desktop (see Section 3.5) using 16 processors are approximately 90 h for $N_{GL} = 10$, 95 h for $N_{GL} = 15$ and 105 h for $N_{GL} = 20$, respectively, for a 55 s simulation time. Because of a shorter time consumption of computation in the smaller number of grid layer and insignificant influence on the motion of flap, $N_{GL} = 10$ are adopted. Fig. 4-6 illustrates the selected mesh model in CFD for the case studies.

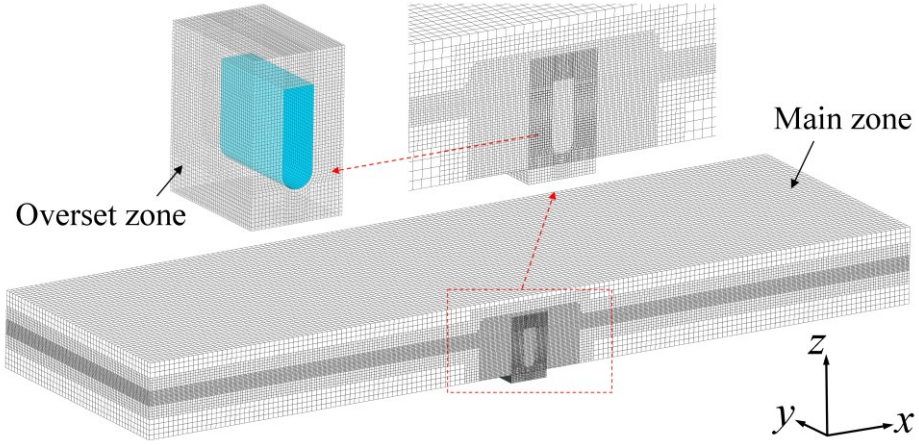

Fig. 4-6 Selected mesh model of the NWT in CFD, including a main zone and an overset zone, in which the flap (in blue) is restricted by a hinge.

5 Nonlinear Hydrodynamics of OWSCs under Regular Waves

5.1 Introduction

This chapter focuses on the comprehensive nonlinear behavior with highly efficient calculation in three-dimensional hydrodynamics of the bottom-hinged OWSCs, including fully submerged and surface-piercing ones. As shown in Fig. 5-1, dependent on the draft depth and the pitch amplitude, the motions of OWSCs can be classified as three distinct modes:

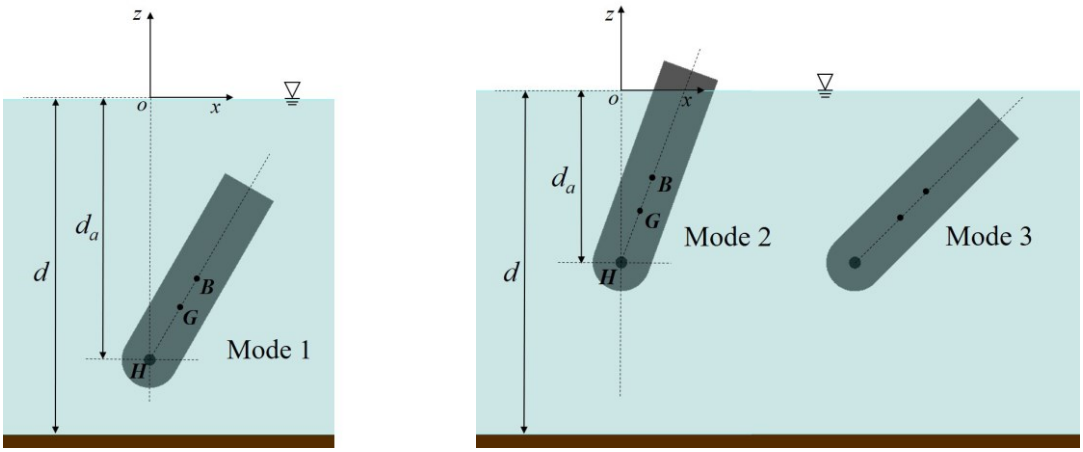

(a) (b)

Fig. 5-1 Front view of three distinct modes of the 3D OWSCs: (a) Mode 1; (b) Modes 2 and 3.

• Mode 1: fully submerged always, in which the flap can be always hidden below the water surface.

• Mode 2: surface piercing always, in which the top of the flap can be always above the ocean surface.

• Mode 3: alternating between surface piercing and fully submerged, in which the flap is surface piercing in still water but alternates between surface piercing and fully submerged in the case of large-amplitude motion.

5.2 Environmental Loads Related to Wet Surface

Under regular waves, the environmental loads, including wave exciting moment, radiation damping moment, and PTO moment, referred to Chapter 3.

5.2.1 Hydrostatic Restoring Moment

Considering the variations of the wet surface as a result of both the volumetric displacement and the position of buoyancy center varying when the OWSC is inclined with a rotating angle, the nonlinear hydrostatic restoring stiffness can be described as

$$K_{instant}(t) = K_{mean}(t) + \Delta K(t) \tag{5-1}$$

where $\Delta K(\varphi)$ is the additional stiffness and can be described as three distinct types, as follows:

$$\Delta K(t) = \begin{cases} 0, \ \text{Fully submerged} \\ 0.5\alpha_k \rho g w b d_a^2 \cdot \tan^2 \varphi(t) \cdot \sin\varphi(t)/\varphi(t), \ \ |\varphi(t)| \le \varphi_m \\ 0.5\alpha_k \rho g w b d_a^2 \cdot \tan^2 \varphi_m \cdot \sin\varphi(t)/\varphi(t), \ \ |\varphi(t)| > \varphi_m \end{cases} \tag{5-2}$$

where α_k is the modified factor of surface-piercing OWSCs for the adjustment of stiffness (a value of α_k lower than 1 means that the water surface is affected by the flap); φ_m is the threshold angle of the moment when the initial surface-piercing flap becomes just fully submerged.

$$\varphi_m = \cos^{-1}(d_a/h) \tag{5-3}$$

According to Eq. (3-5), when $\varphi(t) = 0$, $M_H(t) = 0$. When $\varphi(t) \neq 0$, $M_H(t)$ can be classified into three different types in the time-domain form.

• Mode 1 (fully submerged always)

$$M_H(t) = -K_0 \sin\varphi(t) \tag{5-4}$$

• Mode 2 (surface piercing always; $\varphi_0 \le \varphi_m$)

$$M_H(t) = -K_0 \sin\varphi(t) - 0.5\alpha_k \rho g w b d_a^2 \cdot \tan^2 \varphi(t) \cdot \sin\varphi(t) \tag{5-5}$$

• Mode 3 (alternating between surface piercing and fully submerged; $\varphi_0 > \varphi_m$)

At the duration when t agrees to $|\sin(\omega t + \theta)| \le \varphi_m/\varphi_0$, $M_H(t)$ has the same form as Eq. (5-5), but when t is out of this range, $M_H(t)$ should be given as follows.

$$M_H(t) = -K_0 \sin\varphi(t) - 0.5\alpha_k \rho g w b d_a^2 \cdot \tan^2 \varphi_m \cdot \sin\varphi(t) \tag{5-6}$$

5.2.2 Drag Moment

Ignoring the effects of wave elevation on the wet surface, $h_w(t)$ in Eq. (3-12) is illustrated in Fig. 5-2 and can be expressed as three different types:

• Mode 1 (fully submerged always)

$$h_w(t) = h \tag{5-7}$$

• Mode 2 (surface piercing always; $\varphi_0 \leq \varphi_m$)

$$h_w(t) = \frac{d_a}{\cos\varphi(t)} \tag{5-8}$$

• Mode 3 (alternating between surface piercing and fully submerged; $\varphi_0 > \varphi_m$)

At the duration when t agrees to $|\sin(\omega t + \theta)| \leq \varphi_m/\varphi_0$, $h_w(t)$ has the same form as Eq. (5-8), but when t is out of this range, $h_w(t)$ can be expressed as follows.

$$h_w(t) = \frac{d_a}{\cos\varphi_m} = h \tag{5-9}$$

Substituting Eqs. (5-7), (5-8), and (5-9) into Eq. (3-12), $M_D(t)$ can be calculated.

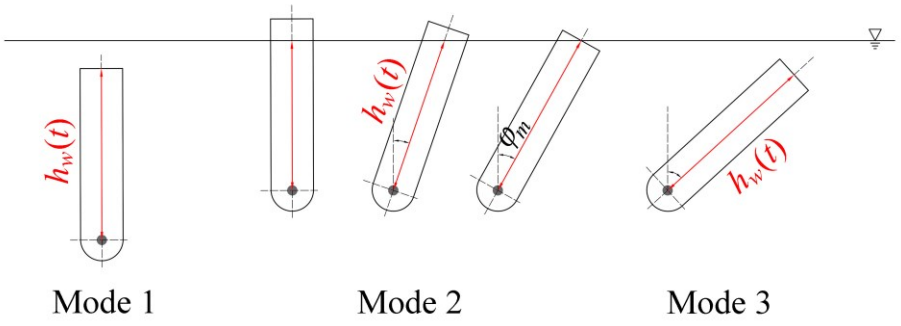

Fig. 5-2 Wet surface height in three different modes.

5.3 Hydrodynamic Coefficients and Dynamic Equations

In this chapter, the hydrodynamic coefficients $M_e(\omega)$, $\mu(\omega)$, $c(\omega)$, and $\psi(\omega)$ are obtained from ANSYS AQWA (student version). The typical grid models of a fully submerged and a surface-piercing OWSC for calculation of these hydrodynamic coefficients are shown in Fig. 5-3. Different from the grid model in NEMOH, the freeboard is also built here because AQWA can automatically define the wet surface grids as diffraction elements and the freeboard grids as non-diffraction elements.

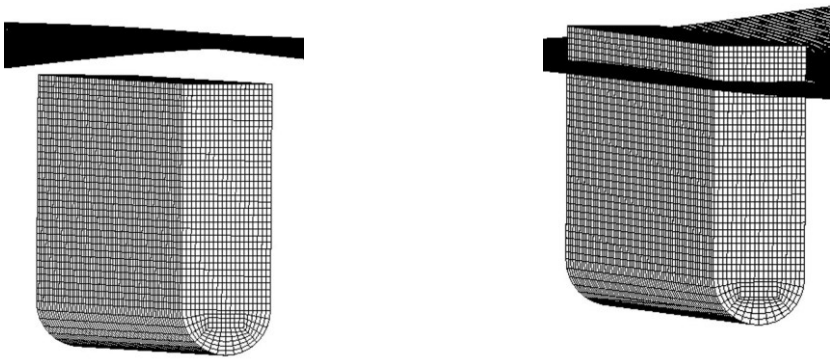

(a) (b)

Fig. 5-3 Grid models for calculation of hydrodynamic coefficients: (a) A fully submerged OWSC; (b) A surface-piercing OWSC.

The calculated hydrodynamic coefficients for an Oyster 800-like OWSC are matched well with the results obtained from NEMOH, shown in Fig. 5-4.

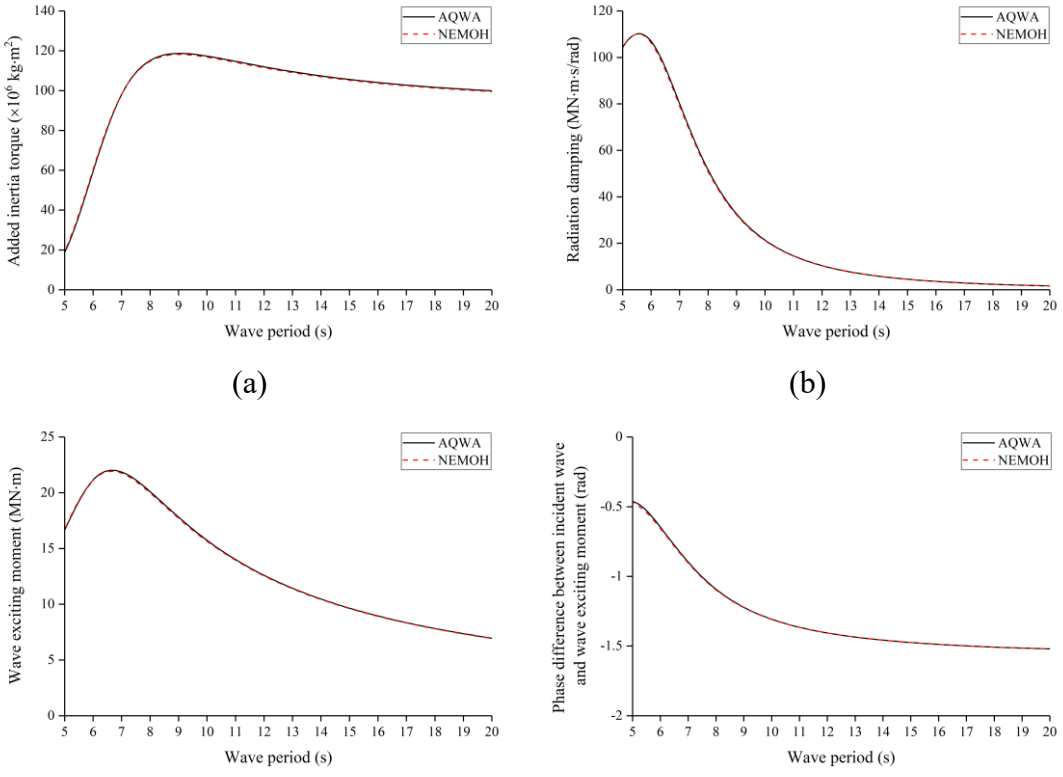

Fig. 5-4 Comparison of the hydrodynamic coefficients under unit-amplitude regular waves between AQWA and NEMOH: (a) Added inertia torque; (b) Radiation damping; (c) Wave exciting moment; (d) Phase difference between the incident wave and the wave exciting moment.

Substituting Eqs. (5-4)–(5-6) into Eq. (3-24), K_{HL} can be obtained. Substituting Eqs. (5-7)–(5-9) into Eq. (3-12), and then into Eq. (3-27), C_{DL} can be obtained. C_{PTOL} in Eq. (3-29) is irrelevant to wet surface. Therefore, the solutions of frequency-domain dynamic equations in three modes can be calculated by Eqs. (3-34)–(3-37).

The time-domain dynamic equations of the flap are classified as three different types, substituting Eqs. (3-1), (3-3), (5-4)–(5-6), (5-7)–(5-9), and (3-16) into Eq. (3-42).

$$\begin{cases} [I_H + I_{PTO} + \mu(\infty)]\ddot{\varphi}(t) + C_{PTO}\dot{\varphi}(t) + \int_0^t R(t-\tau)\,\dot{\varphi}(\tau)d\tau + [K_0(t)+K_{PTO}]\varphi(t) \\ \quad + \frac{1}{2}C_d\rho w\int_0^h [\dot{\varphi}(t)r - u_n(t)]\cdot|\dot{\varphi}(t)r - u_n(t)|\cdot r dr = M_E(t) - M_f(t), \ \text{Model 1} \\ [I_H + I_{PTO} + \mu(\infty)]\ddot{\varphi}(t) + C_{PTO}\dot{\varphi}(t) + \int_0^t R(t-\tau)\,\dot{\varphi}(\tau)d\tau + [K_0(t)+K_{PTO}]\varphi(t) \\ + \frac{1}{2}C_d\rho w\int_0^{d_a/\cos\varphi(t)} [\dot{\varphi}(t)r - u_n(t)]\cdot|\dot{\varphi}(t)r - u_n(t)|\cdot r dr \\ + 0.5\alpha_k\rho g w b d_a^2\cdot\tan^2\varphi(t)\cdot\sin\varphi(t) = M_E(t) - M_f(t), \ \text{Modes 2 and 3 } (\varphi \le \varphi_m) \\ [I_H + I_{PTO} + \mu(\infty)]\ddot{\varphi}(t) + C_{PTO}\dot{\varphi}(t) + \int_0^t R(t-\tau)\,\dot{\varphi}(\tau)d\tau + [K_0(t)+K_{PTO}]\varphi(t) \\ + \frac{1}{2}C_d\rho w\int_0^{d_a/\cos\varphi_m} [\dot{\varphi}(t)r - u_n(t)]\cdot|\dot{\varphi}(t)r - u_n(t)|\cdot r dr \\ + 0.5\alpha_k\rho g w b d_a^2\cdot\tan^2\varphi_m\cdot\sin\varphi(t) = M_E(t) - M_f(t), \ \text{Mode 3 } (\varphi > \varphi_m) \end{cases} \tag{5-10}$$

where $\mu(\infty)$ can be obtained by a fitting curve (Gao and Liang, 2019) of $\mu(\omega)$, because AQWA, unlike NEMOH, cannot directly output the value of $\mu(\infty)$.

5.4 Results and Discussion

5.4.1 Validation

To validate the mathematical model, the numerical results of three different modes were compared with the published experimental data. In the time-domain analysis, because of the nonlinearities, the response of the flap is not completely but nearly sinusoidal. The time-averaged pitch amplitude of the flap during 10 wave periods (31–40 *T*, where *T* is the regular wave period) is adopted as the time-domain numerical results:

$$\bar{\varphi}_{amp} = \frac{1}{10}\sum_{i=31}^{40}\frac{\varphi_{\max(i)} - \varphi_{\min(i)}}{2} \tag{5-11}$$

where $\varphi_{\max(i)}$ and $\varphi_{\min(i)}$ are, respectively, the maximum and minimum values within the ith wave period.

It showed from the experimental study by Whittaker et al. (2005) that there were significant differences in the behavior of the OWSC in 2D and 3D tests. Renzi et al. (2014b) theoretically explained that a simplified 2D OWSC underestimated the CWR than a 3D OWSC. For these reasons, all of the study cases are 3D OWSCs.

Cheng et al. (2019) simulated the hydrodynamics of an OWSC with the drag coefficient $C_d = 1.2$ and validated with both the published numerical results of a scaled model in Wei et al. (2015) and the laboratory experimental results in Henry et al. (2014). This chapter follows the selection of the value $C_d = 1.2$ for the validation of numerical results of these scaled models. Besides, the factor $\alpha_k = 0.1$ in Eq. (5-10) was tested, confirming the numerical results of scaled and full-scale models with good accuracy.

Xu et al. (2016) tested 3D experiments of the bottom-hinged OWSCs with various water depths under regular waves. The fully submerged flap (Mode 1) with a total height of 0.75 m at water depth $d = 1$ m was chosen (see flap A in Table 5-1). According to the given natural period T_n, $\overline{GH}$ can be reversely derived.

The flaps of Mode 2 are selected from the 3D experimental models conducted by Ning et al. (2017). The total height is $h = 1.05$ m, greater than d_a (see flaps B, C, and D in Table 1). They had the same geometric size but different inertia, and the threshold angle is $\varphi_m = 34.05°$.

Table 5-1 Geometric parameters and physical properties of the study cases.

Flap	Mode	w (m)	b (m)	h (m)	d (m)	d_a (m)	h_f (m)	m (kg)	I_H (kg·m2)	$\overline{BH}$ (m)	$\overline{GH}$ (m)	Reference
A	1	1	0.25	0.75	1	1	--	42.2	12.63	0.375	0.485	Xu et al. (2016)
B								29.8	13.77		0.57	
C	2	0.8	0.15	1.05	0.9	0.87	0.18	51.8	14.52	0.45	0.462	Ning et al. (2017)
D								73.4	17.81		0.453	
E	3	1.04	0.12	0.48	0.6	0.44	0.04	33	1.84	0.196	0.16	Wei et al. (2015)

Wei et al. (2015) conducted 3D experiments of a surface-piercing OWSC (see flap E in Table 5-1) at Queen's University Belfast. The pitch amplitude of the flap was large without a PTO system so that the flap went from initially surface piercing to fully submerged (Mode 3) when reaching the maximum rotational angle. The threshold angle is $\varphi_m = 23.56°$. The

experimental results of the pitch amplitude of the flap are greater than φ_m. Table 5-1 lists the geometric and physical parameters of the experimental flaps.

Neglecting the inertia, stiffness, and damping of the PTO system in all these experiments, only the friction moment was applied. Table 5-2 shows the regular waves and PTO parameters.

Table 5-2 Wave conditions and PTO parameters of the study cases.

Case No.	Flap	T (s)	A_i (m)	T_{PTO} of PTO (N · m)
1	A	1.75	0.0625	15
2	A	2	0.125	15
3	B	1.79	0.083	75
4	C	1.79	0.083	75
5	D	1.79	0.083	75
6	D	3.13	0.067	75
7	E	2	0.06	0
8	E	2	0.1	0

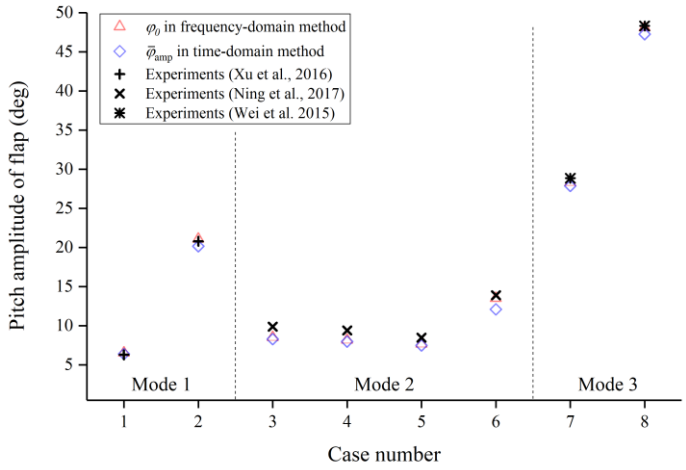

Fig. 5-5 Validation of numerical results against experiments for each case.

In Fig. 5-5, most numerical results have good agreement with the experiments, but the elapsed time of running a frequency-domain calculation (≈ 15 s for a single wave case on a desktop with 4.0 GHz CPU and 16 GB RAM) is much less than time-domain method (≈ 2 min for a single wave case on the same computer). It should be noticed that the numerical results of Mode 2 (Cases 3–6) are a little lower than the experimental results because the friction moments of the PTO system in experiments were a little lower than the theoretical value as a result of the irregular disturbance of the current controller, as explained by Ning et al. (2017). The numerical results (Cases 3–6) in the present study slightly overestimated the PTO friction moment, resulting in the more conservative pitch amplitude.

However, these published experiments only focused on a few wave periods without covering a wide range of wave frequencies. More detailed experimental research will be held in the future.

5.4.2 Linear vs. Nonlinear Solution in Frequency-Domain Analysis

Using a small pitch amplitude assumption, Tom et al. (2016) studied a surface-piercing flap and presented a linear solution of one-degree-of-freedom motion, which ignored the PTO inertia torque and stiffness and was described as

$$\varphi_0 = \frac{M_E(\omega)}{\sqrt{\{K_0 - [I_H + \mu(\omega)]\omega^2\}^2 + \{[c(\omega)+C_{PTO}]\omega\}^2}} \tag{5-12}$$

where the hydrostatic stiffness was assumed as a constant value K_0 when $\varphi \leq 30°$. The linear solution can be solved directly without iterations but cannot consider the nonlinear effects of the stiffness, drag, and PTO system.

In this sub-section and below, the research model is an Oyster 800-like OWSC, the properties of which refer to Chapter 3. The wave amplitude is 1 m. The frequency-domain numerical results compare with the OpenFOAM simulation results. According to Eq. (5-11), the time-averaged pitch amplitude result $\bar{\varphi}_{amp}$ is still extracted from the OpenFOAM solution. The drag coefficient $C_d = 5$ is calibrated well for the full-scale Oyster 800, according to the comparison between the frequency-domain results and OpenFOAM simulation results without PTO damping.

Notice in Fig. 5-6 that the nonlinear frequency-domain results agree well with the OpenFOAM results at the whole wave period range. However, the linear results calculated by Eq. (5-12) are good only at short wave periods because of the small pitch amplitude, but they have a large error when the pitch amplitude increases at long wave periods. It is evident that taking the nonlinear items into account is necessary especially when the pitch amplitude is large, up to 30°.

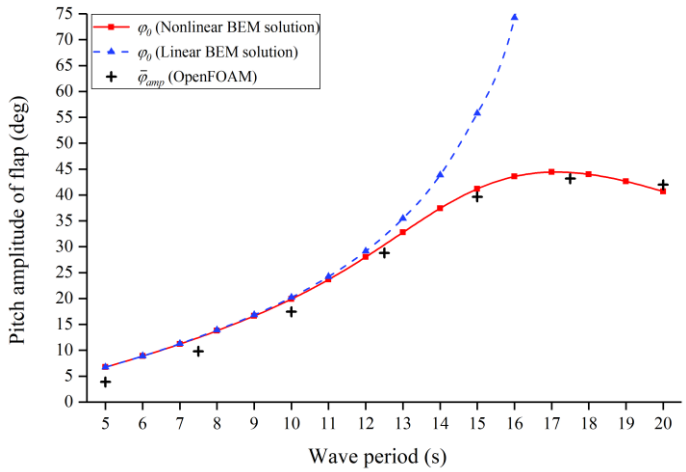

Fig. 5-6 Comparison of frequency-domain results with OpenFOAM simulation results without PTO system.

5.4.3 Surface Piercing vs. Fully Submerged

In this sub-section, the CWR of a surface-piercing OWSC ($h = 10$ m and $d_a = 9$ m at water depth $d = 12.5$ m, shown in Fig. 5-1b) compare to fully submerged OWSCs of different water depths ($d = 14.5$–20.5 m, shown in Fig. 5-1a) with the same foundation height ($d - d_a = 3.5$ m for all OWSCs), geometric size, physical property (except buoyant center—e.g., $\overline{BH} = 4.206$ m for fully submerged OWSCs), and identical PTO system. Whittaker et al. (2007) and Whittaker and Folley (2012) thought that an OWSC usually does not have a large oscillation under a common sea state due to being far away from resonance. Thus, the frequency-domain method is applicable for the flap with an intermediate PTO damping. Fig. 5-7 shows the CWRs for surface-piercing and fully submerged OWSCs when $K_{PTO} = 0$, $C_{PTO} = 16$ MN · m · s/rad, $T_{PTO} = 0$, and $C_d = 5$.

The performances of various fully submerged OWSCs of different water depth are almost lower than the surface-piercing one, especially under long waves, because more wave energy flows over the fully submerged devices. It also proves that the surface-piercing OWSC, such as the Oyster 800, can absorb more wave energy than the same-sized fully submerged one at most wave conditions. However, the fully submerged OWSCs of shallow submerged depth (e.g., at 14.5 m deep water) exhibit a little higher CWR at the wave periods from 9 s to 11 s, because the current PTO damping is a little small for surface-piercing OWSCs but favorable for fully submerged ones of shallow submerged depth at some specified wave periods. Another reason is the larger working surface of fully submerged flap, being beneficial for these wave periods.

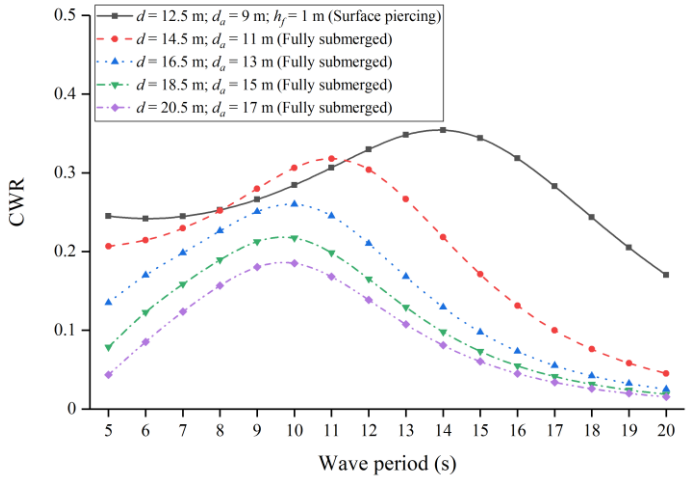

Fig. 5-7 CWR of a surface-piercing OWSC compared with fully submerged OWSCs of different water depths.

5.4.4 Effect of PTO Stiffness

Another model of OWSC with thickness $b = 2$ m and a half of inertia property of the Oyster 800 is investigated to compare with the Oyster 800. Different values of the stiffness of the PTO system are considered. The wave amplitude is 1 m. The frequency-domain method is also applied for the same reason mentioned in the previous sub-section and will be adopted continually in the following sub-sections.

As the results shown in Fig. 5-8 ($C_{PTO} = 16$ MN $\cdot$ m $\cdot$ s/rad, $T_{PTO} = 0$, and $C_d = 5$), the maximum CWR of a 4 m thick flap without PTO stiffness (black solid line) is 0.35 at the wave period 14 s, but the CWR of a 2 m thick flap without PTO stiffness (red dotted line) at the wave period 14 s is only 0.25. Renzi and Dias (2013a) and Gomes et al. (2015) reported that the thickness influences on hydrodynamic coefficients were quite small. The thickness influence on CWR is possibly from the hydrostatic restoring stiffness as a result of buoyancy and gravity. The 2 m thick flap has less restoring stiffness than the 4 m thick flap. When increasing PTO stiffness, the peak of CWR grows and the period of peak decreases. Therefore, the moderate increase of PTO stiffness, such as adding a torque spring at the hinged axis, can be a good strategy for a thin flap to enhance peak CWR.

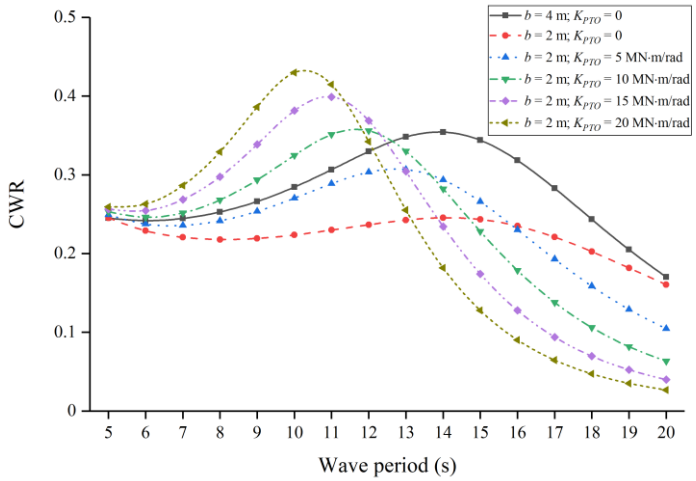

Fig. 5-8 CWR for different values of PTO stiffness.

5.4.5 Effect of PTO Damping

The PTO damping is a significant variable to maximize the CWR for a given OWSC. Fig. 5-9 shows the CWR of the Oyster 800 with different values of PTO damping when ignoring PTO stiffness and friction moment ($K_{PTO} = 0$ and $T_{PTO} = 0$) when $C_d = 5$.

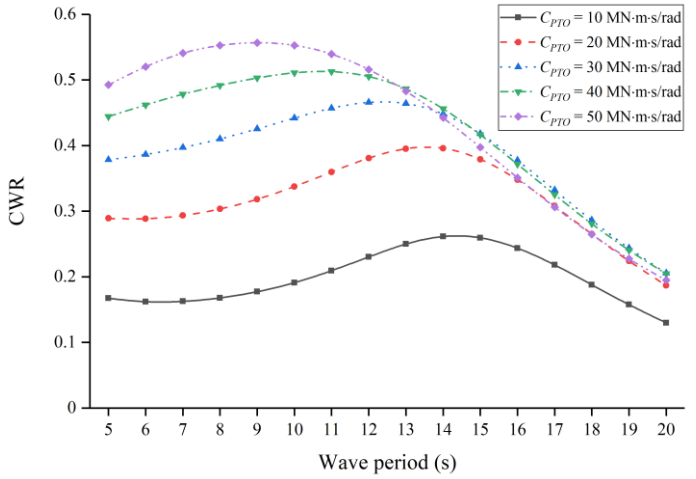

Fig. 5-9 CWR for different values of PTO damping.

The values of CWR entirely increase when C_{PTO} grows from 10 to 30 $\mathrm{MN \cdot m \cdot s/rad}$ but locally decrease with further augmenting. Without a friction moment, a larger PTO damping results in higher performance under short waves. However, Plummer and Schlotter (2009) presented that it was very hard for a hydraulic PTO system that was usually used in OWSCs to produce electricity under small waves, because of friction and other factors. Therefore, the performances at peak energy conditions are recommended to be the primary considerations in PTO system design.

5.4.6 Effect of PTO Friction Moment

The same PTO damping and zero PTO stiffness were considered. The curve of CWR for different values of the PTO friction moment is shown in Fig. 5-10, when $K_{PTO} = 0$, $C_{PTO} = 16\ \mathrm{MN \cdot m \cdot s/rad}$, and $C_d = 5$. The CWR decreases significantly with an increasing PTO friction moment for almost the whole wave period range. The frictional resistance against the oscillating of the flap is harmful to the captured wave power, so the reduction of the friction moment will be a way to enhance the CWR.

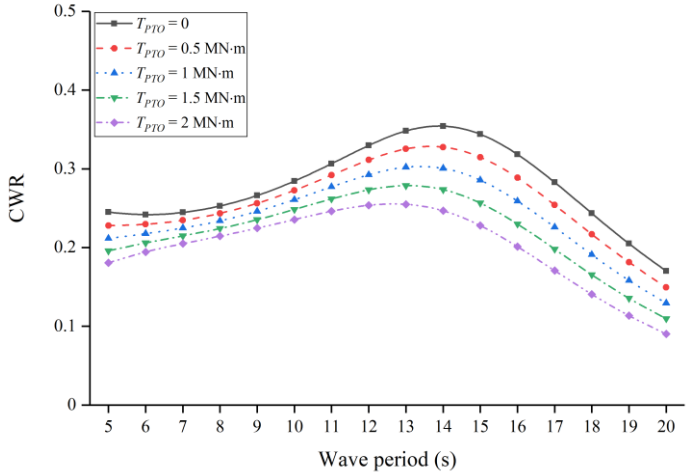

Fig. 5-10 CWR for different values of the PTO friction moment.

5.4.7 Effect of Drag Coefficient

The effect of the drag coefficient is also studied in comparison with the effect of the PTO friction moment when $K_{PTO} = 0$, $C_{PTO} = 16\ \mathrm{MN \cdot m \cdot s/rad}$, and $T_{PTO} = 0$. As shown in Fig. 5-11, as the drag coefficient increases, the CWR decreases slightly at short wave periods but largely around the period of peak. It proves that the viscosity has the maximum influence around the resonant wave period. In resonance conditions, the pitch angular amplitudes are much bigger, and the incremental velocity amplitudes, resulting in much higher drag forces, lead to large viscous dissipation.

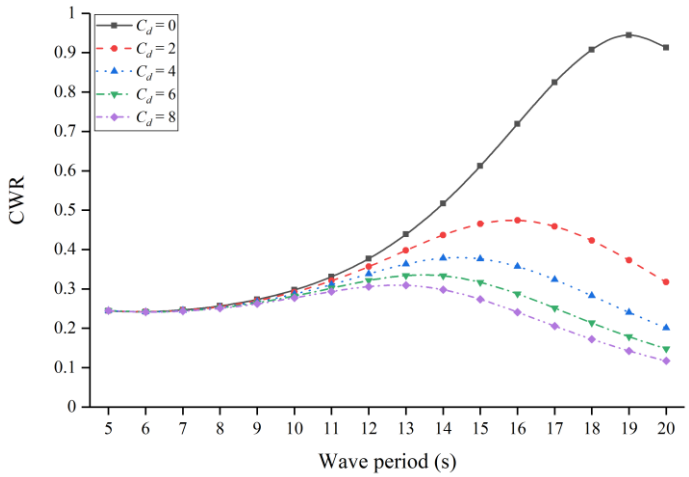

Fig. 5-11 CWR for different values of the drag coefficient.

5.5 Conclusions in the Chapter

According to the devices operating fully submerged or surface piercing, the motions of the bottom-hinged OWSCs in the waves are classified into three distinct modes:

- Fully submerged always;
- Surface piercing always;
- Alternating between surface piercing and fully submerged.

The results from the validation of cases indicate that the present numerical results compare well against the published experimental results, and the computation in frequency-domain method takes less time than the time-domain method. It proves that the frequency-domain method with linearization of nonlinear stiffness, drag, and friction can efficiently predict the motion of flaps with good accuracy, even if pitch amplitude is larger than 30° when the nonlinearities play important roles.

The linear solution of pitch amplitude was significantly overestimated in long waves. The performance of a surface-piercing OWSC is better than the fully submerged one in most wave conditions. To enhance the peak CWR for a thin flap, the way to increase the stiffness of the PTO system can be applicable, for example, by adding a torque spring at the hinged axis. A proper PTO damping helps to ensure maximum power, but in the design of a real PTO system, the CWR under peak energy periods at a given wave energy farm will be a prior consideration. The CWR decreases with either the increasing viscous drag coefficient or the increasing PTO friction moment. The CWR might be overestimated without viscous drag, especially near the

resonant zone. Making efforts to decrease the PTO friction leads to less energy loss and higher CWR.

This chapter has a limitation of ignoring the effects of wave elevation on the wet surface in the calculation of hydrostatic restoring moment and drag moment. A part of contents in Chapters 1–4 and this chapter was published in International Journal of Offshore and Polar Engineering ([5] in Publications).

6 Resonant Behaviors of OWSCs

6.1 Introduction

Resonance study is one of the subsystems of hydrodynamic research. Some studies demonstrated the structural dynamic amplifications near resonance in calculating the reaction forces for offshore platforms (Anagnostopoulos, 1982), coastal bridges (Istrati and Buckle, 2014), and piles (Choi et al., 2015) subjected to the wave impacts. Taking inspiration from the above phenomenon, resonance could be prospective in the promotion of wave energy absorption by amplifying the dynamic response of WECs. For example, tuning a point absorber to resonance, when its undamped natural period is close to the period of a regular wave (Falcão, 2010) or the dominant period of an irregular wave (Korde, 1999), can be recognized as an effective approach to derive more energy. However, a flap-type WEC, usually of relatively large size, has a different resonant mechanism to the traditional point absorber, due to its diffracting of the wave's propagation. The resonant behaviors of an OWSC in a channel were investigated using a semi-analytical method and concluded that the resonant sloshing modes lead to increase the maximum CWR (Renzi and Dias, 2012). The research of an OWSC in front of a vertical wall also proved that the much higher levels of CWR were achieved when the OWSC was located at a specific distance from the vertical wall, in which the larger wave torque was produced due to an appropriate phase difference between the reflected wave and the exciting wave (Sarkar et al., 2015). However, less attention has been paid to the study of resonant wave interactions with OWSCs in the open sea.

In this chapter, the time-domain BEM was employed. A wave surface correcting factor was introduced for more accurate calculation of hydrostatic restoring moment and drag moment. The free decay analysis, and the relationship of resonance to the responses and CWRs under regular and irregular waves, are discussed.

6.2 Environmental Loads Related to Wet Surface

In Chapter 5, the wave elevation was not considered in the calculation of $h_w(t)$. This chapter will consider the effects of wave elevation on wet surface.

6.2.1 Corrected Wave Surface

The actual wave surface, with the existence of a flap, is different from the incident wave. In this study, the wave surface is corrected, as shown in Fig. 6-1, to adjust the restoring stiffness

and drag moment for more accurate results. $R_w(t)$ is the instantaneous distance between the hinge point H and its projection on the corrected wave surface along the mid-surface of the flap, and this can be given by

$$R_w(t) = \alpha_\eta[\eta_w(t) - d_a] + d_a \tag{6-1}$$

where α_η is the wave surface correcting factor; $\eta_w(t)$ is the instantaneous distance between point H and its projection on the incident wave surface, obtained via geometric measurement according to the incident wave elevation $\eta(t)$ and the flap angle $\varphi(t)$. The instantaneous height of the wet surface above the hinge was given by

$$h_w(t) = min[R_w(t), h] \tag{6-2}$$

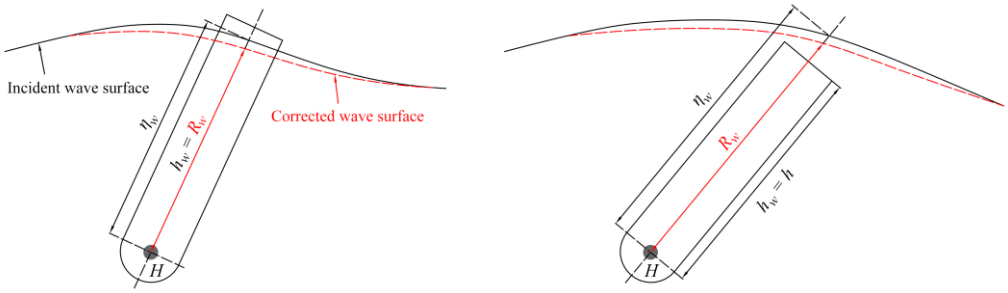

Fig. 6-1 A schematic diagram of a corrected wave surface.

6.2.2 Hydrostatic Restoring Moment

Both $F_b(t)$ and $\overline{BH}(t)$ in Eq. (3-11) are dependent on the wet surface (below the corrected wave surface),

$$F_b(t) = \rho g w \left[h_w(t)b + \frac{\pi b^2}{8}\right] \tag{6-3}$$

$$\overline{BH}(t) = \frac{12h_w^2(t) - 2b^2}{24h_w(t) + 3\pi b} \tag{6-4}$$

Substituting Eqs. (6-3) and (6-4) into Eq. (3-11), and then into Eq. (3-5), $M_H(t)$ can be gained.

6.2.3 Drag Moment

Substituting Eq. (6-2) into Eq. (3-12), $M_D(t)$ can be obtained.

6.3 Free Decay Analysis

According to time-domain dynamic equation in Eq. (3-42), in the free decay analysis of a flap with an initial inclination under still water, $M_E(t) = 0$, $\eta(t) = 0$, $T_{PTO} = 0$, $\dot{\varphi}(0) = 0$, $\ddot{\varphi}(0) = 0$ and a nonzero $\varphi(0)$ are set.

The response of free decay in still water is studied with different initial angles. According to the time–history curve of response extracted from OpenFOAM, as shown in Fig. 6-2, the natural period can be estimated by measuring the time distance between the first and second valley values of the response. Without friction ($T_{PTO} = 0$), the averaged periods of response in cases with different initial angles and either an undamped flap ($C_{PTO} = 0$) or a damped flap ($C_{PTO} = 16\ \mathrm{MN \cdot m \cdot s/rad}$) are, respectively, 17.57 s or 19.15 s. The measured period of response lengthens when configuring PTO damping. In actuality, the natural period without additional declaration usually defaults as the natural period of an undamped flap without friction for the judgment of resonance, i.e., 17.57 s.

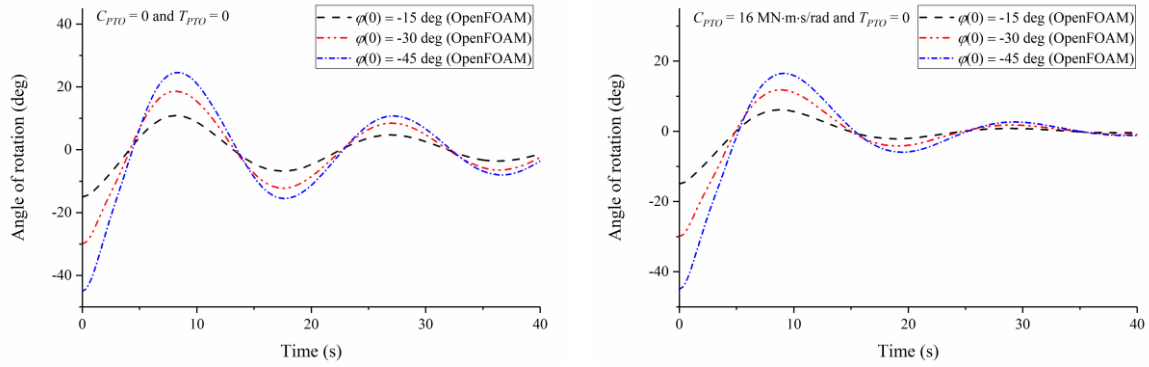

(a) (b)

Fig. 6-2 Time–history free decay response based on CFD for three distinct initial angles of a no-friction flap with different PTO damping: (a) C_{PTO} = 0; (b) C_{PTO} = 16 MN·m·s/rad.

In BEM, the actual water surface, affected by the moving flap's radiating wave, is difficult to determine. It is assumed that the water surface is always horizontal in free decay analysis, i.e., $\alpha_\eta = 1$ in Eq. (6-1). The free decay responses for different drag coefficients in BEM are calibrated with CFD, as shown in Fig. 6-3. It is noticed by observation from the periods of these signals that the case of a 30° initial angle matches relatively well with OpenFOAM, as shown in Fig. 6-3b. However, a longer period with a small initial angle 15° and a shorter period with a large initial angle 45° are observed in Fig. 6-3a,c, respectively. These inaccurate results in BEM are possibly caused by the assumption of a horizontal water surface.

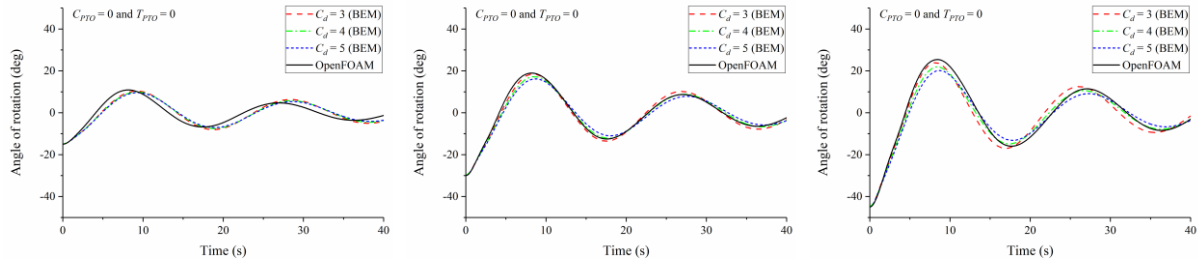

(a) (b) (c)

Fig. 6-3 Comparison of free decay between BEM and CFD for a flap without a PTO system and with different initial angles: (a) 15°; (b) 30°; (c) 45°.

To understand the distinctions between BEM and CFD in free decay analysis, Fig. 6-4 shows some typical frames in the CFD of a flap without a PTO system at three different initial angles. The water surface near the flap is elevated in several frames, and the elevation seems quantitatively unpredictable. Theoretically, the values of the radiation damping moment, the restoring moment, and the drag moment are disturbed by the change in the realistic wet surface, but cannot be accurately considered in BEM.

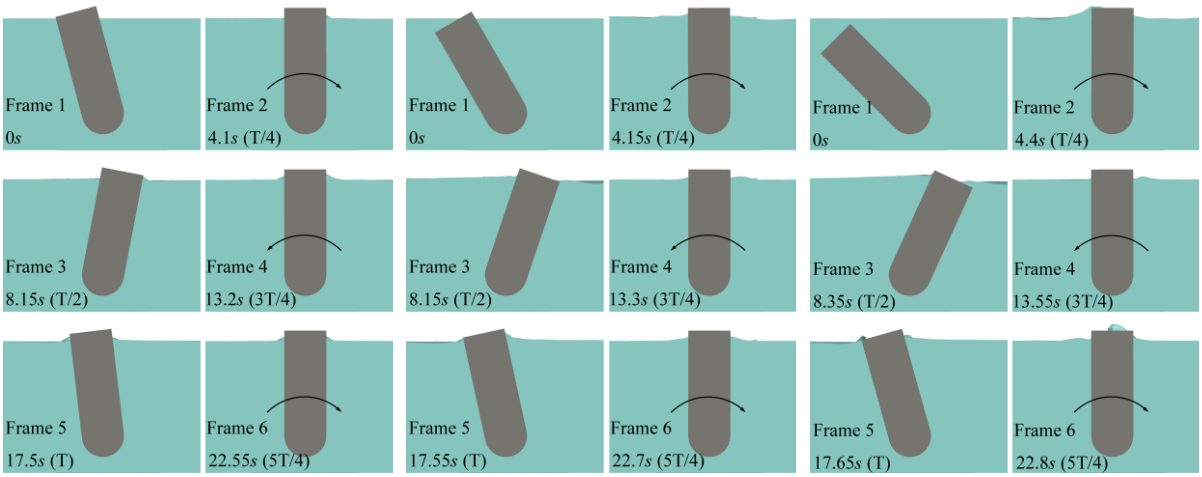

(a) (b) (c)

Fig. 6-4 Screenshots of free decay analysis of a flap without a PTO system and with different initial angles in CFD: (a) 15°; (b) 30°; (c) 45°.

The values of C_d from 2 to 6 were scanned to find a proper drag coefficient with a minimum NRMSE of BEM against CFD in the case of a 30° initial angle. As shown in Fig. 6-5a, $C_d = 3.4$ leads to the lowest NRMSE. The comparison of time–history free decay response between BEM ($C_d = 3.4$) and CFD is illustrated in Fig. 6-5b. For engineering applications of the free decay analysis based on BEM, an intermediate initial angle (e.g., 30°) with a selection of $C_d = 3.4$ for the current model is more appropriate.

For a 40 s simulation time of a 30° initial angle free decay response, the computational cost on the same desktop (see Section 3.5) is about 30 s for the Python code based on BEM (on 1 processor), except the elapsed time of extracting hydrodynamic coefficients for one time from NEMOH. However, it takes about 40 h for the CFD simulation with 16 processors in OpenFOAM.

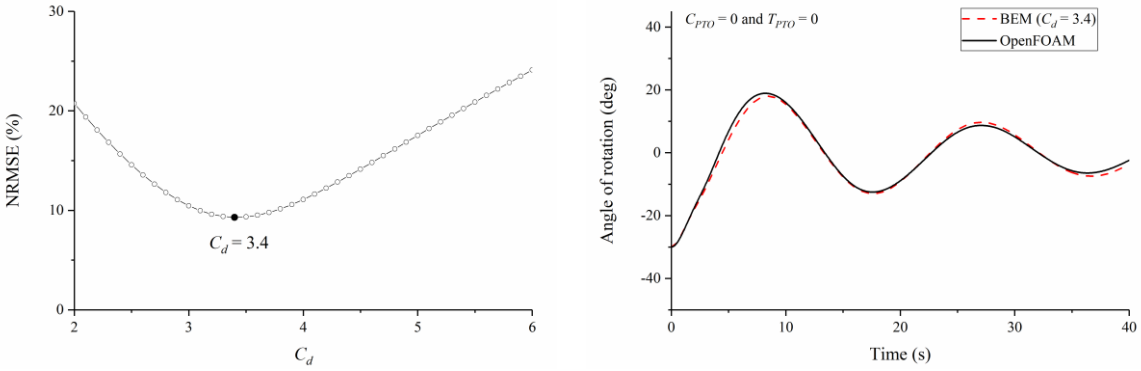

(a) (b)

Fig. 6-5 Results in the case of a 30° initial angle: (a) NRMSE vs. C_d; (b) Comparison of time–history free decay response between BEM (corresponding to the minimum NRMSE) and CFD.

6.4 Under Regular Waves

In this section, the responses of the flap under regular waves are studied. The range of wave period is from 5 to 23 s. The unit-amplitude waves and the varying wave heights corresponding to the uniform wave exciting moment are considered, respectively. The range of PTO damping is from 0 to 64 MN · m · s/rad, and the range of PTO friction is from 0 to 3 MN · m. However, the expanded range of PTO parameters can be included in some study cases with additional illustrations.

6.4.1 Calibration of BEM with CFD

There are two undecided factors in the computation of the response under waves in BEM: wave surface correcting factor α_η and drag coefficient C_d. The results of equivalent pitch amplitude in BEM and CFD are extracted according to Eq. (3-44). The NRMSEs of the pitch amplitude in BEM with respect to the CFD of both the undamped ($C_{PTO} = 0$) and damped ($C_{PTO} = 16$ MN · m · s/rad) flaps, without friction and under unit-amplitude regular wave conditions ($T = 5$–22.5 s with interval 2.5 s), were calculated.

Fig. 6-6 indicates that $\alpha_\eta = 0.16$ and $C_d = 5.4$ are well calibrated for the time-domain BEM results in the study's model. It should be noted that the corrected wave surface is not a

realistic water surface, and it only numerically influences the computations of restoring moment and drag moment for the sake of better accuracy.

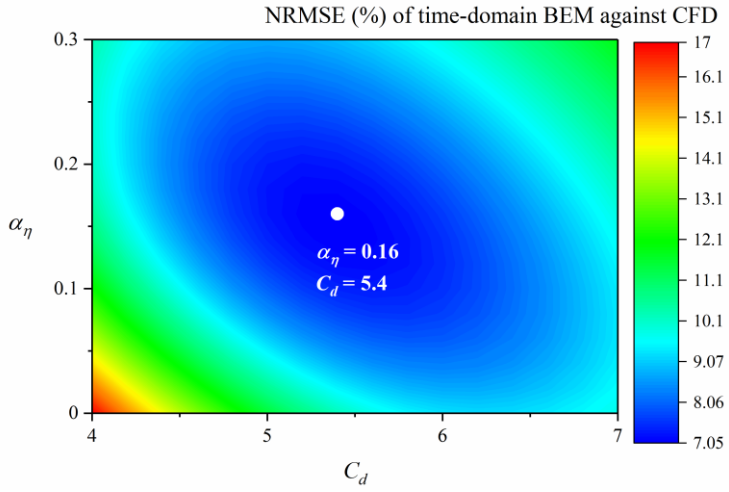

Fig. 6-6 NRMSE of BEM against CFD for different values of α_η and C_d.

With the calibrated factors, a good agreement of BEM with CFD in the whole range of wave periods from 5 s to 23 s is shown in Fig. 6-7. However, BEM slightly overestimated the response in short periods due to the constant drag coefficient, which was Keulegan–Carpenter (KC) and Reynolds (Re) number-dependent (Sarpkaya, 1976). Using a larger value of the non-constant drag coefficient would seem to be necessary for a high Re number under short waves in future work. Given its acceptable accuracy and efficient computation, the calibrated BEM will be adopted in the next sub-sections.

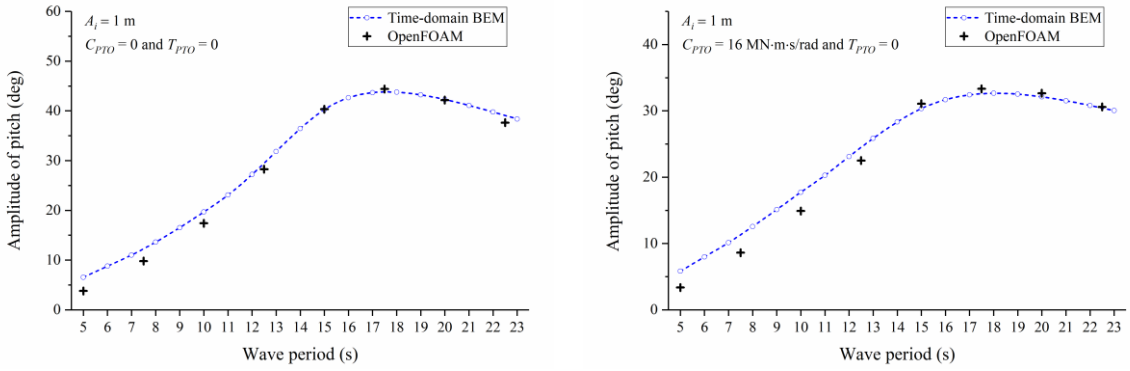

(a) (b)

Fig. 6-7 Comparison of pitch amplitude under regular waves of unit-amplitude between BEM and CFD of a no-friction flap with different PTO damping: (a) C_{PTO} = 0; (b) C_{PTO} = 16 MN·m·s/rad.

Taking an example of a simulation under a unit-amplitude regular wave, the computational cost to run the Python code based on BEM (on 1 processor) on the same desktop (see Section

3.5) is about 4 min for 40 wave cycles. However, it takes about 190 h for 6 wave cycles in OpenFOAM with 16 processors.

6.4.2 When Does the Maximum Pitch Occur?

The responses of the flap under regular waves of uniform amplitude ($A_i = 1$ m) and uniform wave exciting moment (e.g., $M_e(\omega)A_i = 10$ MN · m), assessed by varying the wave amplitude for each period, are studied to determine the maximum pitch amplitude.

Fig. 6-8a shows the wave amplitudes for different wave periods with respect to $M_e(\omega)A_i = 10$ MN · m. When the wave period is longer than 15 s, the wave amplitude is greater than 1 m (the freeboard height $h_f = 1$ m). Based on the assumption of a linear relationship between wave amplitude and wave exciting moment amplitude, the wave torque of a high wave in BEM may be imprecise, due to wave overtopping. Fig. 6-8b shows a comparison of the pitch amplitude of a flap without a PTO system ($C_{PTO} = 0$ and $T_{PTO} = 0$) between BEM and CFD, confirming the reasonable precision of BEM related to the slight influence of wave overtopping under such intermediate waves (the wave amplitude slightly exceeds the freeboard height).

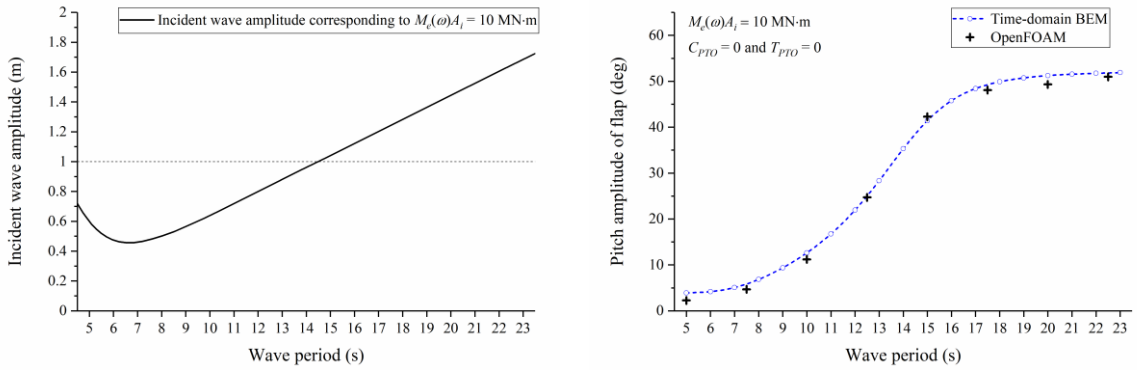

(a) (b)

Fig. 6-8 Parameters and results for regular waves of uniform wave exciting moment amplitude 10 MN·m: (a) Incident wave amplitude vs. period; (b) Comparison between BEM and CFD of a flap without a PTO system.

Fig. 6-9 shows the pitch amplitude results of a no-friction flap with various values of PTO damping C_{PTO} under regular waves of uniform amplitude and exciting moment amplitude. The maximum pitch amplitudes (solid point on each curve, between 16 s and 19 s in Fig. 6-9a) with different C_{PTO} values occur within a small range of wave periods from 17.6 s to 18.3 s, close to the natural period (17.57 s is obtained from the free decay analysis in CFD). This means that

the flap resonates near the natural period. However, there are no obvious maximum values of pitch amplitude near the natural period with uniform wave exciting moment amplitude, as shown in Fig. 6-9b. Therefore, the resonant conditions of regular waves, in which an incident wave near the natural period produces the maximum response over wave periods, should be restricted by employing the same amplitude of incident wave elevation, rather than the same amplitude of wave torque.

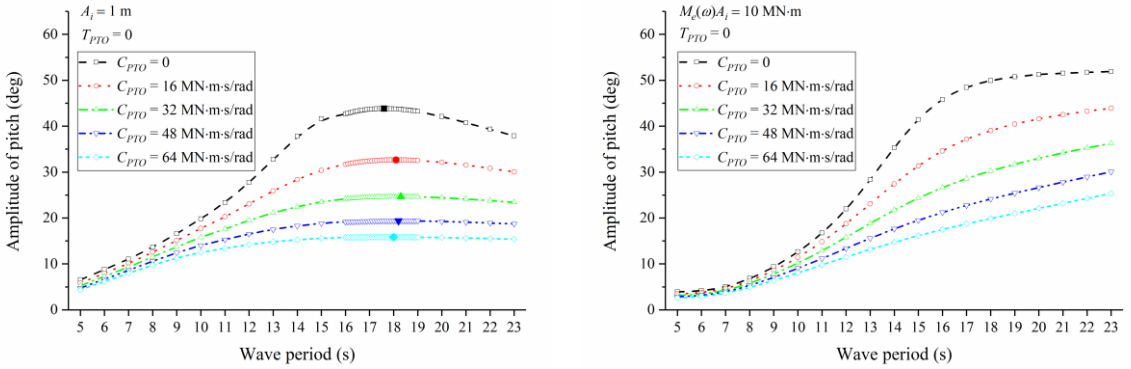

(a) (b)

Fig. 6-9 Pitch amplitude results of a no-friction flap for various values of PTO damping under regular waves of: (a) Uniform wave amplitude; (b) Uniform wave exciting moment amplitude.

Fig. 6-10a shows the effects of friction (with an expanded range) on the period of maximum pitch amplitude of a damped flap ($C_{PTO} = 16\ \mathrm{MN \cdot m \cdot s/rad}$). The increasing value of friction breaks the resonance rule (the maximum response occurs near the natural period) by moving the period of maximum pitch amplitude towards the period of peak wave exciting moment, which is near 7 s for the current model, as shown in Fig. 6-10b.

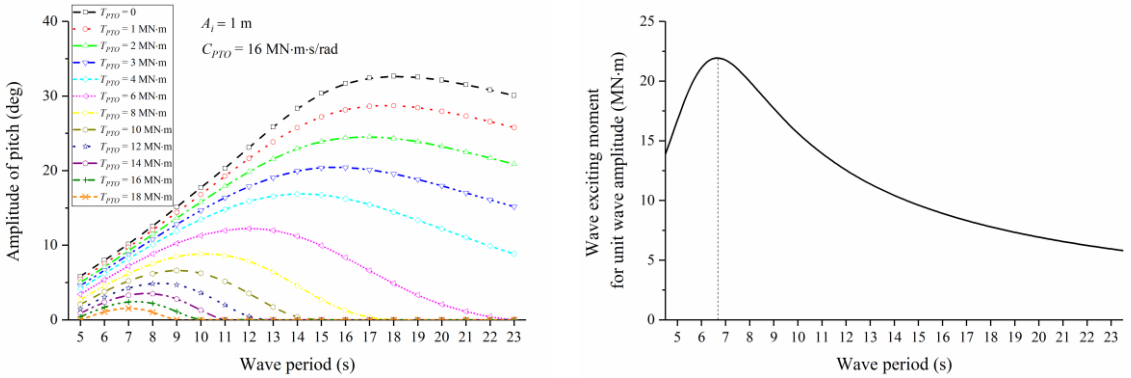

(a) (b)

Fig. 6-10 (a) Pitch amplitude results for a damped flap with various values of PTO friction under unit-amplitude regular waves; (b) Wave exciting moment for unit wave amplitude.

6.4.3 Phase Characteristics Near and Far from Resonance

The phase angle of angular velocity relative to the wave exciting moment θ_2 of a flap with different PTO damping and friction values under unit-amplitude regular waves was studied. A negative value of θ_2 means that the angular velocity lags behind the wave exciting moment, and a positive value denotes the advance of angular velocity. As mentioned in Section 3.2.1, the velocity is in phase with the wave torque, i.e., $\theta_2 = 0$ represents the occurrence of resonance in a one-degree-of-freedom structure with constant inertia, stiffness, and damping. It is evident from Fig. 6-11 that the values of θ_2 are not zero near the natural period (orange circle). Therefore, the standard of $\theta_2 = 0$ for the assessment of resonance in the hydrodynamics of a flap is unreliable, due to the strong nonlinearities of the restoring and drag moments.

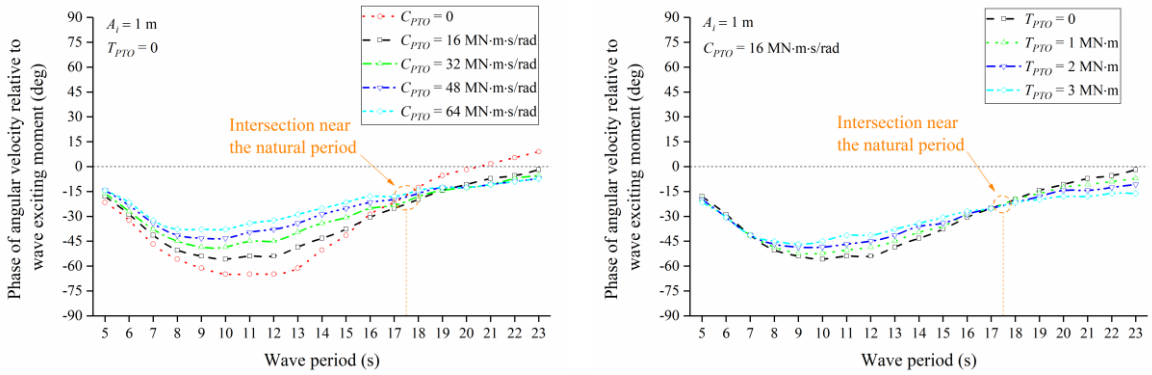

(a) (b)

Fig. 6-11 Phases of angular velocity relative to wave exciting moment under unit-amplitude regular waves: (a) Various values of C_{PTO} and T_{PTO} = 0; (b) Various values of T_{PTO} and C_{PTO} = 16 MN·m·s/rad.

A higher value of C_{PTO} or T_{PTO} generally produces a trend of diminishing hysterical angles of angular velocity (absolute value of a negative θ_2) within a shorter period than the natural period, and it causes increases in hysteretic angle or reductions in advanced angle (value of a positive θ_2) over a longer period. However, the intersections of these phase vs. period curves always occur near the natural period.

To understand the phase characteristics near to or far from resonance, Fig. 6-12 shows the time–history curves of the ratios of the wave exciting moment and angular velocities for a no-friction flap with various PTO damping during one wave cycle, over periods of 12 s, 17.5 s (near the natural period), and 23 s. The ratios are defined as below with a steady response,

$$R_E(t) = \frac{M_E(t)}{\max\left(|M_E(t)|\right)} \tag{6-5}$$

$$R_v(t) = \frac{\dot{\varphi}(t)}{\max\left(|\dot{\varphi}(t)|\right)} \tag{6-6}$$

where $R_E(t)$ and $R_v(t)$ are, respectively, the ratio of the wave exciting moment and the ratio of the angular velocity.

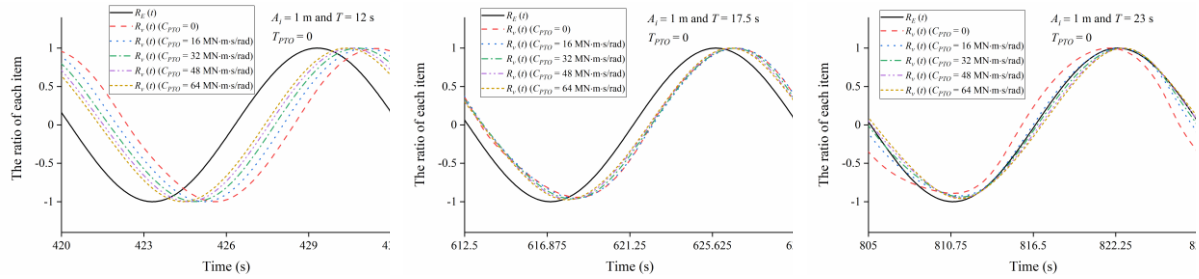

(a) (b) (c)

Fig. 6-12 Time–history of the ratios of wave exciting moment and angular velocities of a no-friction flap for various values of PTO damping under unit-amplitude regular waves: (a) T = 12 s; (b) T = 17.5 s near the natural period; (c) T = 23 s.

With various values of PTO damping, there are obviously different phases of angular velocity relative to the wave exciting moment in a wave period of 12 s, but the distinctions are slight over a wave period of 17.5 s, close to the natural period. Under a long wave of period 23 s, the angular velocity of an undamped flap ($C_{PTO} = 0$) precedes the wave exciting moment slightly, shown as the red dotted line in Fig. 6-12c, but the angular velocities are almost in phase with the wave torque for various values of PTO damping from 16 to 64 $\mathrm{MN \cdot m \cdot s/rad}$.

6.4.4 Relationship between Maximum CWR and Resonance

To understand the relationship between the maximum CWR and the resonance, Fig. 6-13a shows the CWRs of a no-friction flap with various degrees of PTO damping under unit-amplitude regular waves. The period of maximum CWR is apparently shorter than the natural period 17.57 s, and the difference almost increases with the increase in PTO damping. Fig. 6-13b,c exhibits the curves of time–averaged capturing power vs. period and angular velocity amplitude vs. period, respectively. For each value of PTO damping, the period of maximum capturing power is identical with the period of maximum angular velocity amplitude. However, the period of maximum CWR is closer to the period of maximum angular velocity amplitude than to the period of maximum angle amplitude (near the natural period), as listed in Table 6-1. This implies that the highest CWR does not occur simultaneously with resonance.

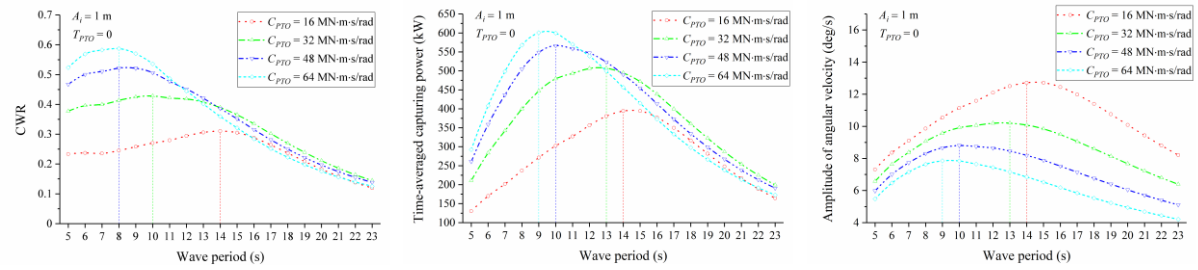

(a) (b) (c)

Fig. 6-13 Results of a no-friction flap with various values of PTO damping under unit-amplitude regular waves: (a) CWR; (b) Time–averaged capturing power; (c) Angular velocity amplitude.

Table 6-1 Periods of peak values of various items under unit-amplitude regular waves.

C_{PTO} (MN · m · s/ rad)	The Periods of Max.				Difference of the Peak Periods	
	Angle Amplitude φ_{amp}	CWR	Capturing Power P_c	Angular Velocity Amplitude $\dot{\varphi}_{amp}$	From Max. CWR to Max. φ_{amp}	From Max. CWR to Max. $\dot{\varphi}_{amp}$
16	18.1 s	14 s	14 s	14 s	22.65%	0
32	18.3 s	10 s	13 s	13 s	45.36%	23.08%
48	18.2 s	8 s	10 s	10 s	56.04%	20.00%
64	18 s	8 s	9 s	9 s	55.56%	11.11%

6.5 Under Irregular Waves

JONSWAP spectrum was adopted. Fig. 6-14a shows a comparison between the original and modified JONSWAP spectra for an irregular wave ($H_s = 6$ m and $T_p = 17.5$ s) in 12.5 m-deep water, and Fig. 6-14b shows the time–history elevation $\eta(t)$ of a modified irregular wave with the specific array of random phase $\phi(\omega_n)$ used for the validation of BEM. Due to the assumption of linear relationship between wave exciting moment and wave amplitude in BEM, the significant wave height is also not allowed very high. After correcting the spectral values, the highest wave elevation is a little more than 1 m (the freeboard heigh of the flap). It implicates that a higher significant wave height might cause the overestimated results because of ignoring the wave overtopping in BEM.

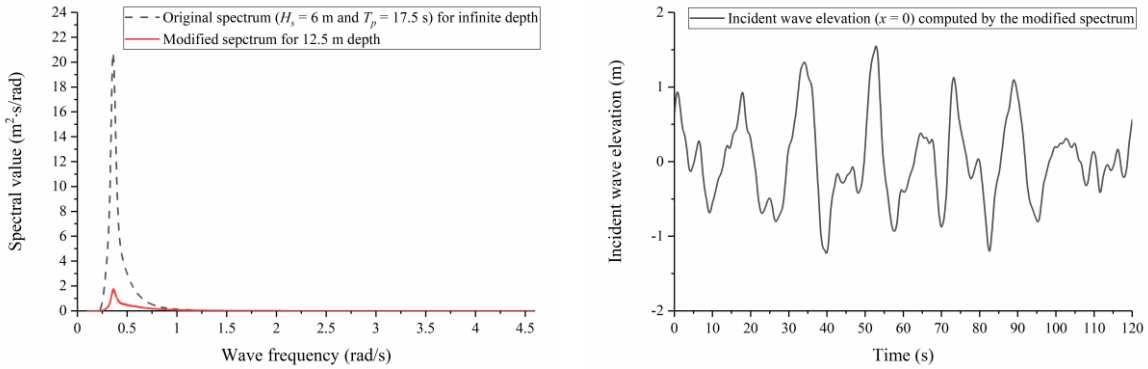

(a) (b)

Fig. 6-14 Irregular wave parameters: (a) Comparison between original JONSWAP spectral values and its modified spectral values in 12.5 m-deep water; (b) Time–history wave elevation of the modified irregular wave for a specific array of random phases of wave components.

6.5.1 Validation of BEM against CFD

The wave surface correcting factor $\alpha_\eta = 0.16$ and drag coefficient $C_d = 5.4$, described in Section 6.4.1, are continuously applied in irregular waves. Fig. 6-15 shows that the time–history response in BEM matches well with that in CFD, using the same wave components and the identical array of random phases within the time–history wave elevation of Fig. 6-14b. Due to the relatively small wave elevation in the modified wave spectrum, the linear assumption of wave exciting moment vs. wave amplitude is still applicable for such an intermediate irregular wave. Considering the linear assumption of wave exciting moment vs. wave amplitude in BEM, a relatively small significant wave height $H_s = 2$ m with lower nonlinearities will be applied in the next case studies.

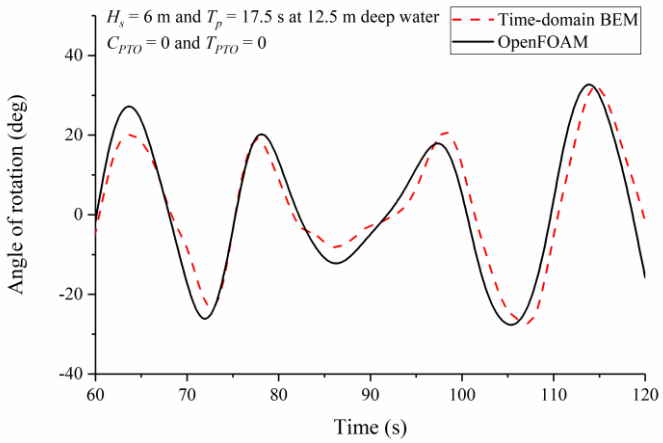

Fig. 6-15 Comparison of the time–history responses of a flap without a PTO system between BEM and CFD under a modified irregular wave in 12.5 m-deep water.

For the 120 s simulation time under an irregular wave, running the Python code based on BEM (on one processor) spends about 4 min on the same desktop (see Section 3.5), and the elapsed time for CFD with 16 processors is about 192 h.

6.5.2 When Does the Maximum Equivalent Pitch Occur?

Under modified irregular waves with the same significant wave height $H_s = 2$ m, the equivalent pitch amplitudes φ_{eq} of each peak period for various values of PTO damping C_{PTO} are calculated. The maximum equivalent pitch amplitude of a flap without a PTO system ($C_{PTO} = 0$ and $T_{PTO} = 0$) appears in a peak period longer than the natural period, shown via the black dotted lines in Fig. 6-16a, but the period of maximum φ_{eq} decreases significantly with the increase in C_{PTO}. This reveals that the maximum equivalent pitch amplitude cannot consistently occur near the natural period, which differs from the results under regular waves. This can be explained via the response under an irregular wave, achieved from the linear combination of the results derived using multi-components of regular waves.

In a specified JONSWAP spectrum, the proportion of longer waves relative to the peak period is less than that of the shorter waves due to the asymmetry of spectral values, and the transfer function (i.e., the response for unit-amplitude regular waves in Fig. 6-9a) under shorter waves thus dominates the synthetic solution. Fig. 6-9a shows that the difference between the transfer function in a short period and its maximum value near the natural period reduces with the increase in C_{PTO}. In other words, the short-period transfer function for a large C_{PTO} contributes relatively more to the equivalent pitch amplitude than a small C_{PTO}. That is why the maximum equivalent pitch amplitude for a larger C_{PTO} appears within a shorter peak period.

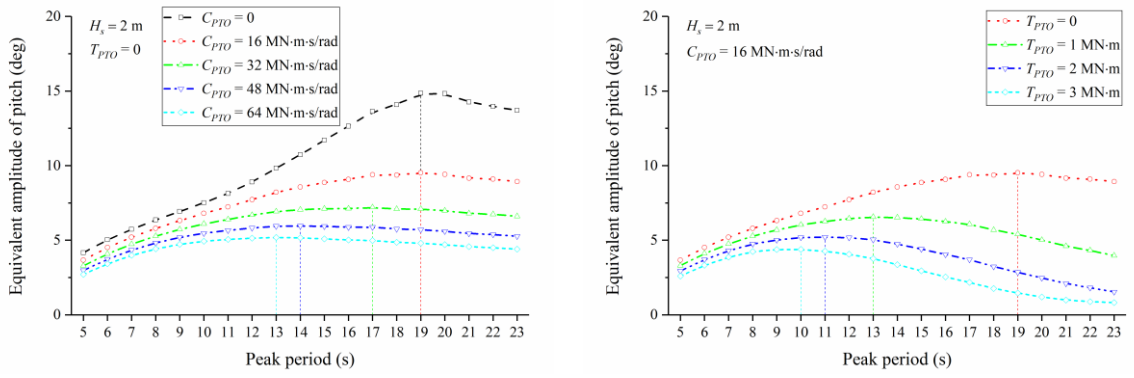

Fig. 6-16 Equivalent pitch amplitude results under modified irregular waves in 12.5 m-deep water: (a) Various values of C_{PTO} and T_{PTO} = 0; (b) Various values of T_{PTO} and C_{PTO} = 16 MN·m·s/rad.

As shown in Fig. 6-16b, the impact of the friction on the peak period of maximum equivalent pitch amplitude is similar to that under regular waves, as discussed in Section 6.4.2.

6.5.3 Phase Characteristics Near Natural Period

Fig. 6-17 shows the time–history wave exciting moment and angular velocities for different values of PTO damping and friction when the peak period is close to the natural period, $T_p = 17.5$ s and $H_s = 2$ m in 12.5 m-deep water. It is found that the angular velocity lags behind the wave exciting moment (orange arrows), and the phase difference reduces with the increase in either PTO damping C_{PTO} or friction T_{PTO}, as opposed to the near-constant phase difference (hardly affected by C_{PTO} and T_{PTO}) near the natural period under regular waves, shown in Fig. 6-11.

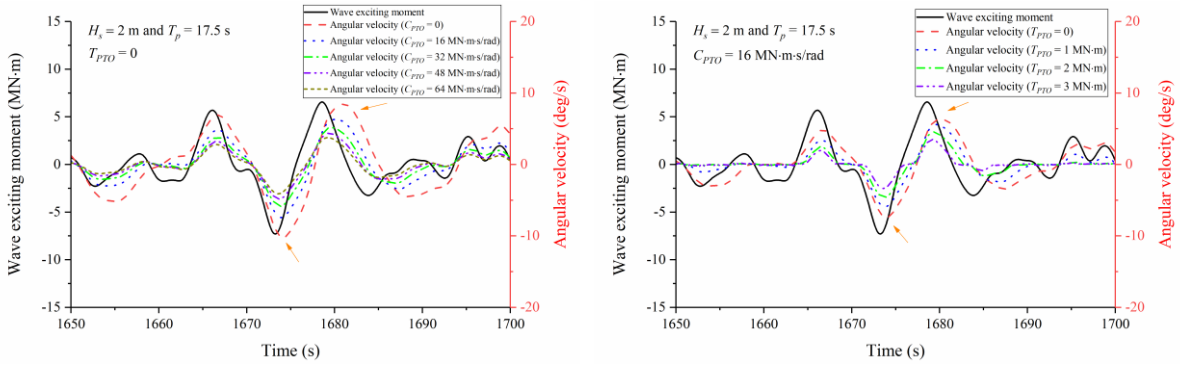

(a) (b)

Fig. 6-17 Time–history wave exciting moment and angular velocities under a modified irregular wave during five repetitions of the peak period: (a) Various values of C_{PTO} and T_{PTO} = 0; (b) Various values of T_{PTO} and C_{PTO} = 16 MN·m·s/rad.

6.5.4 CWR vs. Peak Period

Fig. 6-18 shows the curves of CWR vs. peak period for various values of PTO damping when $H_s = 2$ m. Similar to the results under regular waves, the maximum CWR here appears in a peak period lower than the peak period of the maximum equivalent pitch amplitude, as quantitatively compared with Fig. 6-16a, and it declines with the increase in PTO damping.

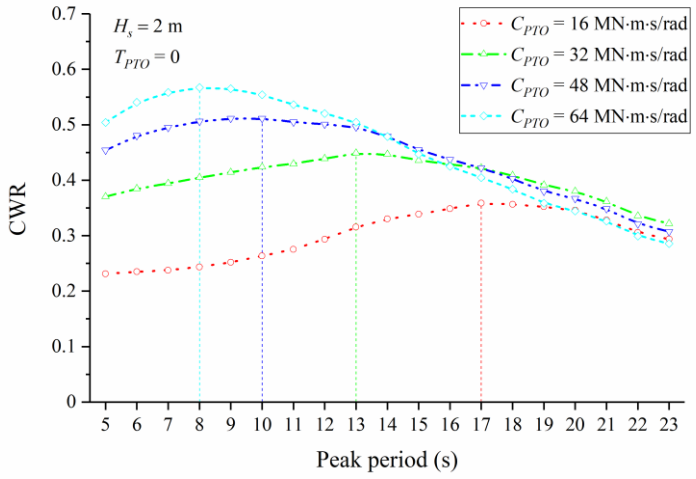

Fig. 6-18 CWRs of a no-friction flap for various values of PTO damping under modified irregular waves in 12.5 m-deep water.

6.6 Conclusions in the Chapter

To improve the accuracy of time-domain BEM, a corrected time-varying wet surface was introduced to calculate the nonlinear hydrostatic restoring moment and drag moment. The wave surface correcting factor α_η and drag coefficient C_d are calibrated with the CFD results in OpenFOAM. For an Oyster 800-like flap, the factors $\alpha_\eta = 1$ and $C_d = 3.4$ are applicable for free-decay analysis in still water, and $\alpha_\eta = 0.16$ and $C_d = 5.4$ are suitable in regular and irregular waves.

In the analysis of free decay, an intermediate angle—30° in this study—is recommended as the initial inclination in BEM for the estimation of the natural period, because a small initial angle overestimates the natural period and a large initial angle underestimates it.

Under regular waves, one criterion when judging resonance is the period of maximum pitch amplitude with uniform wave amplitude, rather than the uniform amplitude of the wave exciting moment. A large value of friction destroys the resonant condition and drives the period of maximum pitch closer to the period of peak wave torque. Perfect resonance cannot be achieved, because a hysteresis of angular velocity relative to the wave exciting moment near the natural period is always present, and is almost independent of PTO damping and friction. Maximum CWR does not coexist with resonance but relatively near the largest angular velocity, the period of which is lower than that of maximum pitch (resonance).

Under irregular waves of the same significant height, the peak period of maximum equivalent pitch amplitude reduces with the increase in PTO damping. This implies that

resonance cannot exist stably at a peak period near the natural period. The angular velocity also lags behind the wave torque within the current regime of PTO damping and friction when the peak period is close to the natural period. Here, one discrepancy from the results under regular waves is that the hysterical angle of angular velocity relative to wave torque relies on either PTO damping or friction. In addition, the curves of CWR vs. peak period for different PTO damping exhibit a similar trend to the results under regular waves.

This chapter studied the resonant behaviors based on weak nonlinear hydrodynamics and is applicable for small-amplitude waves. A part of contents in Chapters 1–4 and this chapter was published in Journal of Marine Science and Engineering ([4] in Publications).

7 Performance Enhancement of OWSCs via Resonant Adjustment

7.1 Introduction

The working principle of a flap-type WEC was to amplify the wave torque to enhance the capturing power without the need of turning to resonate with the incident waves (Renzi et al., 2014b). However, the inertia adjustment was experimentally studied and concluded the magnified efficiency in the long regular waves by increasing the flap inertia (Flocard and Finnigan, 2012). Introducing pitch stiffness into the PTO system was numerically proved to capture more power at some frequencies than the flap without pitch stiffness (Benites-Munoz et al., 2020). It implies that the adjustment of inertia and stiffness would still be beneficial to the hydrodynamic performance for a flap-type WEC, despite the wave torque might dominate. The augment of inertia enlarges the natural period, and the flap thus resonates under a longer period wave. Oppositely, the increase of stiffness shortens the natural period, and the flap hence syntonizes at a shorter period. However, it is uncertain as to how much the resonant adjustment (i.e., change of the natural period by adjusting the inertia and stiffness) influences the hydrodynamic performance for an OWSC.

This chapter used the frequency-domain BEM and assumed the mean wet surface under waves, i.e., $K_H(t) = K_{mean}(t)$ and $h_w(t) = d_a$. The main purpose is to interpret the principle and discuss the feasibilities of the resonant adjustment for both regular and irregular waves in order to promote hydrodynamic performance. Another objective is to find the relationship between the best situation of wave energy harvesting for each wave period and the perfect resonance.

7.2 Approaches of Performance Enhancement

Maria-Arenas et al. (2019) introduced some PTO control strategies to enhance the performance, including damping, reactive, latching, and model predictive controls. In this chapter, the damping control (varying C_{PTO}) and reactive control (varying I_{PTO}, K_{PTO}, and C_{PTO}) for maximizing CWR are comparatively analyzed. For a given wave condition, P_w is determined, while P_c is strongly related to PTO system. In order to maximize the CWR, upgrading the value of P_c by adjusting PTO parameters is essential, assuming $T_{PTO} = 0$.

7.2.1 Under Regular Waves

Substituting Eq. (3-34) into Eq. (3-48), and the capturing power under regular waves can be expressed as

$$P_c = \frac{1}{2} C_{PTO} \frac{[M_e(\omega) A_i]^2}{[(K_{HL} + K_{PTO})/\omega - (\Delta I + I_{PTO})\omega]^2 + (\Delta C + C_{PTO})^2} \tag{7-1}$$

To maximize P_c, the optimal PTO damping is mathematically given by

$$C_{PTO\_opt} = \sqrt{[(K_{HL} + K_{PTO})/\omega - (\Delta I + I_{PTO})\omega]^2 + \Delta C^2} \tag{7-2}$$

and then the optimal capturing power can be expressed as

$$P_{c\_opt} = \frac{[M_e(\omega) A_i]^2}{4\sqrt{[(K_{HL} + K_{PTO})/\omega - (\Delta I + I_{PTO})\omega]^2 + \Delta C^2} + 4\Delta C} \tag{7-3}$$

Three methods of adjusting PTO parameters to maximize P_c were summarized in Table 7-1.

(1) No artificial resonance.

Without PTO inertia and stiffness (i.e., $I_{PTO} = 0$ and $K_{PTO} = 0$), the maximized capturing power can be analytically expressed as

$$P_{c\_opt} = \frac{[M_e(\omega) A_i]^2}{4\sqrt{(K_{HL}/\omega - \Delta I\omega)^2 + \Delta C^2} + 4\Delta C} \tag{7-4}$$

(2) Perfect resonance.

P_{c_opt} in Eq. (7-4) can be maximized by adjusting I_{PTO} or K_{PTO} to guarantee $(K_{HL} + K_{PTO})/\omega - (\Delta I + I_{PTO})\omega = 0$, and simultaneously collaborating with C_{PTO_opt}. The maximized capturing power can be analytically calculated by

$$P_{c\_opt} = \frac{[M_e(\omega) A_i]^2}{8\Delta C} \tag{7-5}$$

The condition of adjusting I_{PTO} or K_{PTO} is related to wave frequency, shown in Table 7-1, where $\omega_n = \sqrt{K_{HL}/\Delta I}$ is the natural frequency.

(3) Best performance near resonance.

Because of the frequency-dependent K_{HL}, ΔI, and ΔC, the analytical expression of maximized capturing power in the former two methods may not be the maximal value at some frequencies. To search for the actual maximal solution of P_c, a batch of computational cases for

different PTO parameters (keeping I_{PTO} or K_{PTO} zero, and varying others with a given range and interval for each parameter) are conducted to screen the maximal calculated result of P_c for each frequency. It is noticed in Eq. (3-38) that adjusting one of I_{PTO} and K_{PTO} is sufficient to change the natural period towards the incident wave period.

Table 7-1 Methods of adjusting PTO parameters to maximize the capturing power at an arbitrary wave frequency for regular waves.

No.	Description	Conditions	I_{PTO}	K_{PTO}	C_{PTO}	Maximized P_c
1	No artificial resonance		0	0	$\sqrt{\left(\frac{K_{HL}}{\omega}-\Delta I\omega\right)^2+\Delta C^2}$	Eq. (7-4)
2	Perfect resonance	$\omega \geq \omega_n$	0	$\Delta I\omega^2 - K_{HL}$	ΔC	Eq. (7-5)
		$\omega < \omega_n$	$\frac{K_{HL}}{\omega^2}-\Delta I$	0		
3	Best performance near resonance		0	Scanning	Scanning	Screening
			Scanning	0		

7.2.2 Under Irregular Waves

Substituting Eq. (3-39) into Eq. (3-48), the capturing power under irregular waves can be expressed as

$$P_c = C_{PTO}\int_0^{\infty}\left[\frac{\varphi_0(\omega)}{A_u(\omega)}\right]^2 \cdot S_d(\omega)\cdot\omega^2 d\omega \tag{7-6}$$

Substituting Eq. (3-34) and $A_u(\omega) = A_i$ into Eq. (7-6), the capturing power is formulated by

$$P_c = C_{PTO}\int_0^{\infty}\frac{{M_e}^2(\omega)}{[(K_{HL}+K_{PTO})/\omega-(\Delta I+I_{PTO})\omega]^2+(\Delta C+C_{PTO})^2}\cdot S_d(\omega)d\omega \tag{7-7}$$

For a given irregular wave condition, when keeping both I_{PTO} and K_{PTO} zero, it is still difficult to analytically find the fittest C_{PTO} for maximizing the value of P_c due to the frequency-dependent K_{HL}, ΔI and ΔC. It is also impossible to adjust I_{PTO} and K_{PTO} to guarantee $(K_{HL}+K_{PTO})/\omega-(\Delta I+I_{PTO})\omega = 0$ for all frequencies at same time. Even though the natural period can be controlled equal to the peak period, it also cannot analytically ensure the value of P_c maximal.

To search for the maximal solution of P_c in Eq. (7-6), the transfer functions $\varphi_0(\omega)/A_u(\omega)$ in regular waves of all frequencies of wave components with different PTO parameters, as a database, are calculated firstly. Then, the values of P_c for different wave spectrums can be quickly obtained. Finally, the maximum solution of P_c (the best performance) and the corresponding PTO parameters for each wave condition are found. To understand the effects of adjusting PTO inertia and stiffness on P_c and CWR, compare the results in two methods:

(1) No artificial resonance, i.e., keeping both I_{PTO} and K_{PTO} zero, and scanning C_{PTO} only;

(2) Adjusting towards resonance, i.e., setting one of I_{PTO} and K_{PTO} zero, and scanning other one and C_{PTO}.

7.3 Results and Discussions

The study model is a surface-piercing flap with the same size as an Oyster 800-like OWSC in Chapter 3. To search out the highest CWR of each wave condition, the scanning ranges of PTO inertia torque, stiffness, and damping are from 0 to $110 \times 10^6\ \mathrm{kg \cdot m^2}$, from 0 to $100\ \mathrm{MN \cdot m/rad}$, and from 10 to $160\ \mathrm{MN \cdot m \cdot s/rad}$, respectively. The interval of PTO inertia torque, stiffness, and damping are $10^6\ \mathrm{kg \cdot m^2}$, $1\ \mathrm{MN \cdot m/rad}$ and $1\ \mathrm{MN \cdot m \cdot s/rad}$, respectively. All the PTO parameters can vary for each wave condition.

The natural period is an important property for the resonant study of oscillating bodies. In Eq. (3-38), the natural period is affected by the linearized restoring stiffness K_{HL}, which is dependent on the time–history angle. The non-constant stiffness was replaced by the small-angle stiffness K_0 for the estimate of natural period (Renzi et al., 2014b),

$$T_n = 2\pi\sqrt{(\Delta I + I_{PTO})/(K_0 + K_{PTO})} \tag{7-8}$$

By iterative calculation, due to the frequency-dependent inertia, the computed value of the natural period for the current model is $T_n = 19.44\ \mathrm{s}$, which is significantly larger than the global ocean mean wave period (Caires, 2005). The applications to reduce its natural period by adjusting PTO parameters for boosting the CWR will be studied in the next sub-sections.

7.3.1 Calibration of Drag Coefficient

The drag coefficient of an oscillating body in water is related to KC and Re. For simplification, the drag coefficient was often recognized by some researchers as a constant value, for example, $C_d = 1.2$ was applied for a 2D fully-submerged flap (Cheng et al., 2019), $C_d = 1.98$ was selected for a 3D edges-rounded flap (Gomes et al., 2015), and a calibrated

value of $C_d = 5.4$ was utilized in the time-domain BEM for a 3D Oyster-like OWSC (Liu et al., 2022a). Babarit et al. (2012) claimed that the assessment of the value of C_d was subject to some uncertainty to the results for a flap-type device. Therefore, a more accurate value of drag coefficient is required for the engineering tasks and can be obtained experimentally or numerically.

To achieve a more precise drag coefficient for the current study model, The NRMSEs between BEM for different C_d and CFD simulation results in OpenFOAM, of pitch amplitude results for both the undamped ($C_{PTO} = 0$) and damped ($C_{PTO} = 16\ \mathrm{MN \cdot m \cdot s/rad}$) flaps under unit-amplitude regular waves ($T = 5$–22.5 s with interval 2.5 s) were calculated. Fig. 7-1 shows that $C_d = 5.8$ as the selection of drag coefficient brings the minimum NRMSE for frequency-domain BEM results.

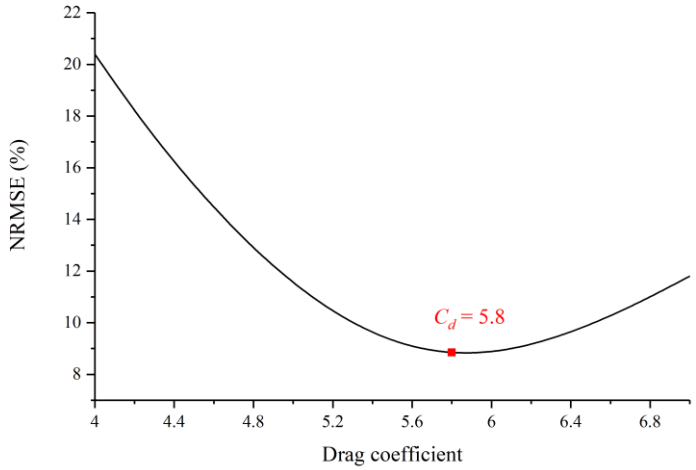

Fig. 7-1 NRMSE of frequency-domain BEM results against CFD results of the undamped and damped flaps under unit-amplitude regular waves.

Fig. 7-2 shows a good accuracy in BEM of the undamped and damped flaps under unit-amplitude regular waves using the calibrated drag coefficient $C_d = 5.8$, compared with CFD results.

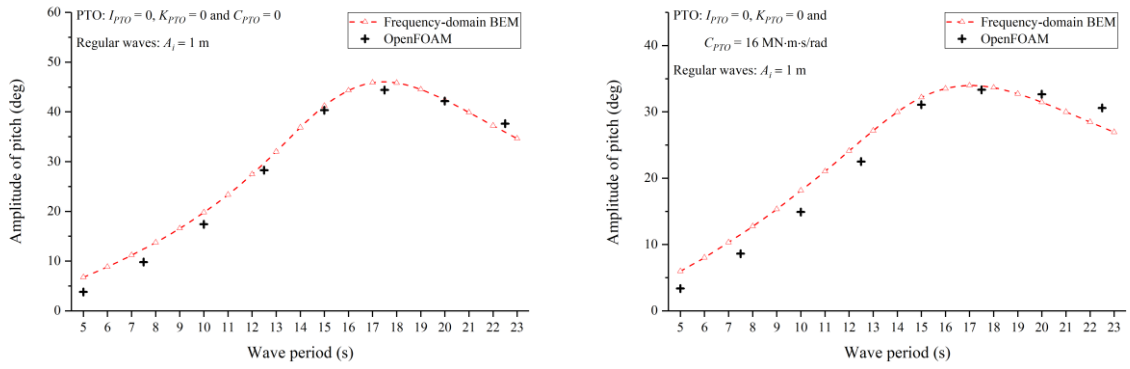

(a) (b)

Fig. 7-2 Comparison of pitch amplitude between frequency-domain BEM using calibrated drag coefficient C_d = 5.8 and CFD results of flaps under unit-amplitude regular waves: (a) C_{PTO} = 0; (b) C_{PTO} = 16 MN·m·s/rad.

To validate the feasibility of drag coefficient $C_d = 5.8$ under an irregular wave, the time–history response of an undamped flap under a modified wave spectrum at 12.5 m water depth corresponding to the original spectrum $H_s = 6$ m and $T_p = 17.5$ s is calculated. Fig. 7-3a shows the time–history incident wave elevation for a specific array of random phases. Fig. 7-3b shows the comparison of time–history pitch between frequency-domain BEM and CFD results of an undamped flap. The acceptable agreement of the results implicates that drag coefficient $C_d = 5.8$ is also applicable for irregular waves.

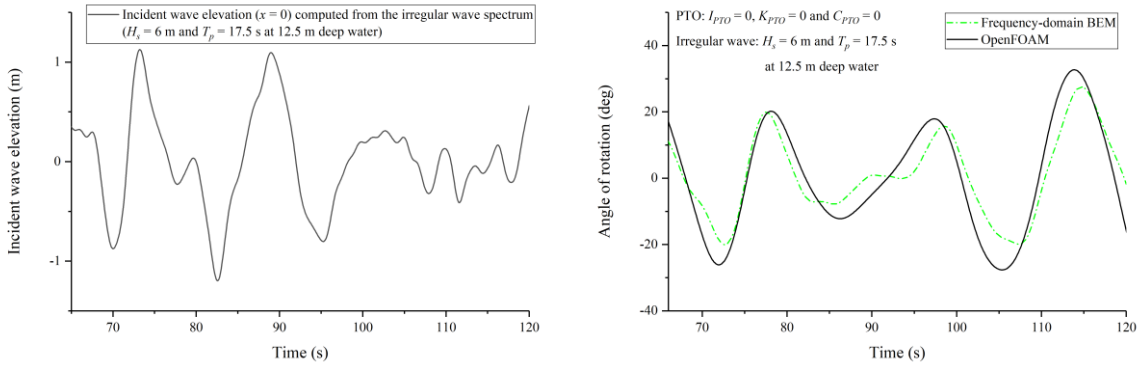

(a) (b)

Fig. 7-3 (a) Time–history wave elevation of a shoaling irregular wave for a specific array of random phases; (b) Comparison of time–history pitch between frequency-domain BEM using calibrated drag coefficient C_d = 5.8 and CFD results of an undamped flap.

For a regular wave case with a given PTO configuration, running a Python code to calculate the pith amplitude, the phase, and the hydrodynamic performance costs approximately 40 s on a desktop of 3.4GHz CPU and 32GB RAM for one processor computation. However, the

elapsed time of a CFD simulation for 6 regular wave cycles in OpenFOAM on a desktop with the same hardware configuration was about 190 h for 16 processors-parallel computation, shown in Chapter 6.

To calculate the performance under an irregular wave, for a given PTO system, it takes about 1 h for running the Python code (on one processor) to obtain the transfer functions $\varphi_0(\omega)/A_u(\omega)$ for various wave frequencies. Then, the response spectrum $S_{out}(\omega)$ in Eq. (3-39) and the hydrodynamic performance can be computed within 1 s for an arbitrary irregular wave. However, the elapsed time for a 120 s-simulation based on CFD was about 192 h for 16 processors-parallel computation, shown in Chapter 6.

Table 7-2 lists the allowable solutions and computational cost (on the same desktop in Section 3.5) for a given PTO system. The present study provides highly efficient computation, although the BEM-based method cannot compute the fluid field in the vicinity of OWSCs and its fidelities might be slightly lower than the CFD simulation.

Table 7-2 Allowable solutions and computational cost.

	Regular wave		Irregular wave		# of processors
	Solutions	Elapsed time	Solutions	Elapsed time	
Present study	φ_0, θ and CWR	≈ 40 s	$\varphi_0(\omega)/A_u(\omega)$ for one time	≈ 1 h	1
			$S_{out}(\omega)$ and CWR	≈ 1 s	
OpenFOAM	$\varphi(t)$ and fluid field	≈ 190 h modeling $6T$	$\varphi(t)$ and fluid field	≈ 192 h modeling 120 s	16

7.3.2 Maximized CWR Without vs. With Artificial Resonance under Regular Waves

Under unit-amplitude regular waves with different periods, Fig. 7-4 shows the maximized CWR in three methods for regular waves mentioned in Section 7.2.1 and the corresponding PTO parameters for each wave period. In Fig. 7-4a, the CWR for the approach of scanning PTO parameters for the best performance at each period (Method 3) is always higher than without artificial resonance (Method 1). The optimized values of PTO inertia and stiffness in Method 3 have similar trends to perfect resonance (Method 2), which explicates that Method 3 is not very far away from perfect resonance, and can be recognized as a near-resonance situation. Consequently, tuning towards resonance by adjusting PTO inertia or stiffness is favorable to

enhance the CWR for the flap-type model, although Renzi and Dias (2013b) believed that the OWSC was not designed tuned to resonance. In the application of resonant adjustment to capture more wave energy, adjusting PTO stiffness, e.g., combining the PTO damper with a torsional spring (Falcão, 2008) at short waves, and adjusting PTO inertia, e.g., coupling a flywheel to an electrical generator (Whittaker and Folley, 2012) at long waves, can be the potential control strategies.

The perfect resonance (Method 2) cannot lead to the maximal CWR except at short periods lower than 7 s and even causes the worse performance at the range of period from 13 s to 18 s than without artificial resonance (Method 1). In other words, the perfect resonance is not always the best situation for wave energy harvesting. The next sub-section will explain it.

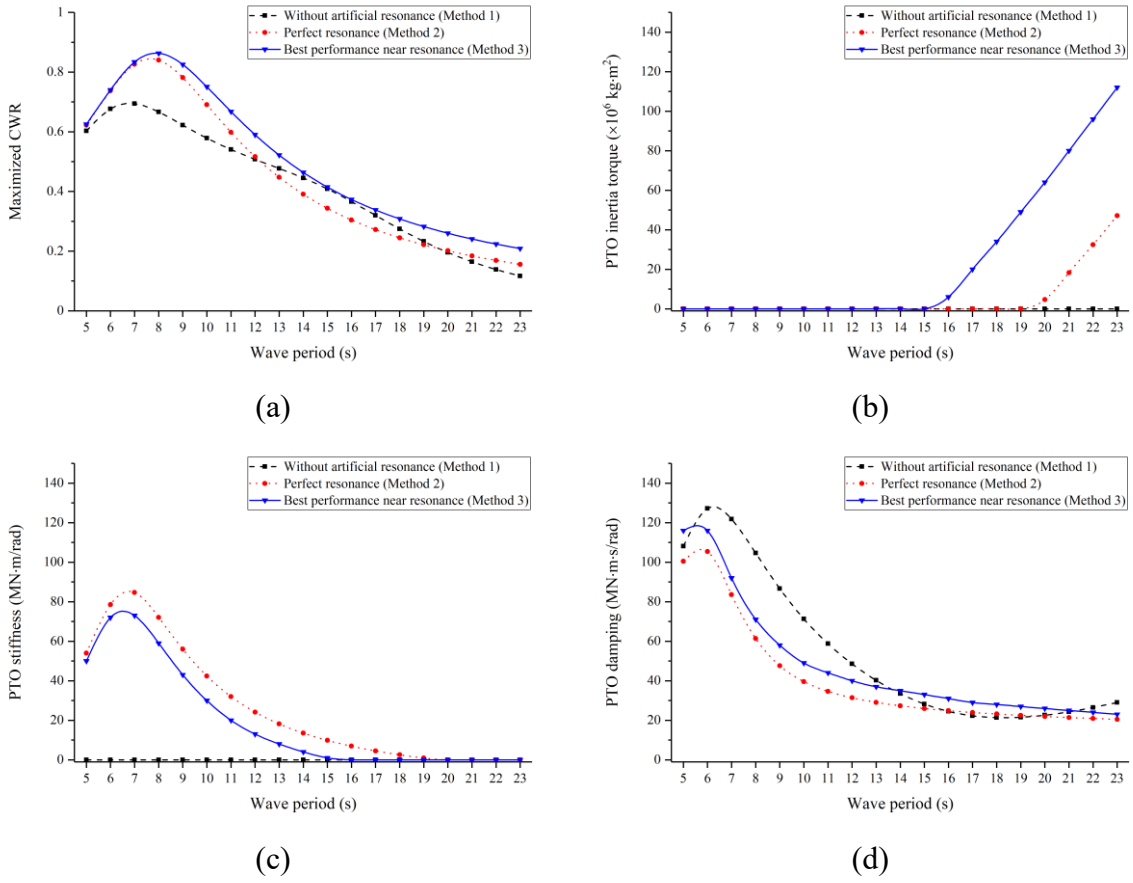

Fig. 7-4 Results in three different methods of maximizing the CWR under unit-amplitude regular waves: (a) Maximized CWR; (b) PTO inertia torque; (c) PTO stiffness; (d) PTO damping.

7.3.3 Why the Perfect Resonance Cannot Produce the Maximal CWR?

To understand why the perfect resonance under regular waves is not the best situation for capturing wave power, define

(1) $|(K_{HL}+K_{PTO})/\omega-(\Delta I+I_{PTO})\omega|$ as the resonant item;

(2) ΔC as the damping item.

For an arbitrary frequency, these two items are expected to be as small as possible for higher capturing power. However, it should be noticed in Eq. (7-3) that compared with the resonant item, a smaller value of the damping item dominates the higher CWR.

Fig. 7-5 presents these two items in three different methods of maximizing the CWR under unit-amplitude regular waves. It is observed in Fig. 7-5a that the resonant items in Method 1 are significantly larger than the other two methods at short periods. It proves that the reduction of the resonant item by tuning towards resonance contributes to the CWR promotion under short waves. Focusing on the results of perfect resonance (Method 2), shown as red dotted lines in Fig. 7-5a,b, the resonant items are always zero, but the damping items are bigger than the 'best' ones (Method 3). Therefore, a balance between a small resonant item and a much lower damping item creates the best performance close to but not exactly at the perfect resonance.

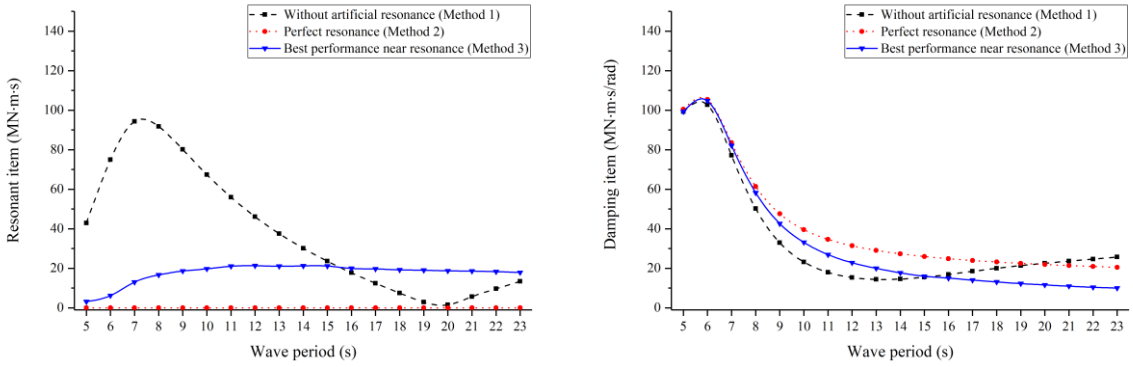

(a) (b)

Fig. 7-5 Items in three methods of maximizing the CWR under unit-amplitude regular waves: (a) Resonant item; (b) Damping item.

7.3.4 Phase Characteristics of Maximized CWR

Under unit-amplitude regular waves, the phase of angular velocity relative to wave exciting moment θ_2 vs. wave period is shown in Fig. 7-6. Adjusting only PTO damping was capable of changing the phase angle of angular velocity (Schmitt et al., 2016a), but more vigorous phase control can be implemented by altering PTO inertia or stiffness. That the velocity is controlled in phase precisely with the wave torque (Method 2) is not always beneficial for the highest hydrodynamic performance. However, a gradually growing hysteretic phase angle (the hysteretic phase angle denotes $|\theta_2|$ when $\theta_2 < 0$) of velocity relative to wave exciting moment with the increase of wave period, shown as the blue line (Method 3) in Fig. 7-6, which is recognized as the fittest phase, indicates the best situation of wave energy absorption. In

summary, PTO inertia and stiffness do not capture the wave energy directly but can establish a good situation of wave energy harvesting via precise phase control.

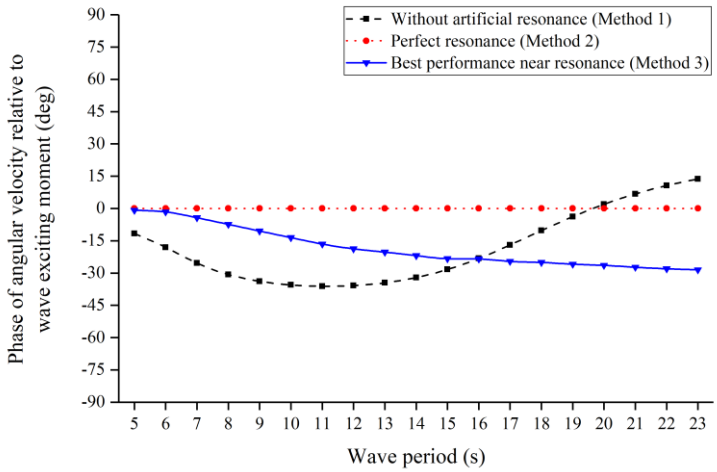

Fig. 7-6 Phase of angular velocity relative to wave exciting moment in three methods of maximizing the CWR under unit-amplitude regular waves.

7.3.5 Maximized CWR Without vs. With Artificial Resonance under Irregular Waves

JONSWAP spectrum was adopted. According to the adjustment of PTO parameters for irregular waves in Section 7.2.2, Fig. 7-7 shows the maximized CWR and corresponding PTO parameters for each peak period under the modified irregular waves of original significant wave height 2 m at 12.5 m deep water. Adjusting towards resonance is also beneficial to improve the CWR for irregular waves, especially when the peak period is shorter than 17 s, shown in Fig. 7-7a.

The optimized K_{PTO} and C_{PTO} for adjusting towards resonance, shown as the purple solid line and the green solid line in Fig. 7-7b, are similar to the results under regular waves. However, the optimized I_{PTO} is always zero, different from the results in regular waves. Flocard and Finnigan (2012) experimentally investigated the effects of inertia adjustment and indicated an increase of power capture under irregular waves by filling the ballast with water. However, the change of ballasting configuration results in the modifications of both inertia torque and restoring stiffness, and thus insufficiently testifies the isolated influence of inertia adjustment. The current result implies that solely adjusting PTO inertia is ineffective for performance promotion under irregular waves.

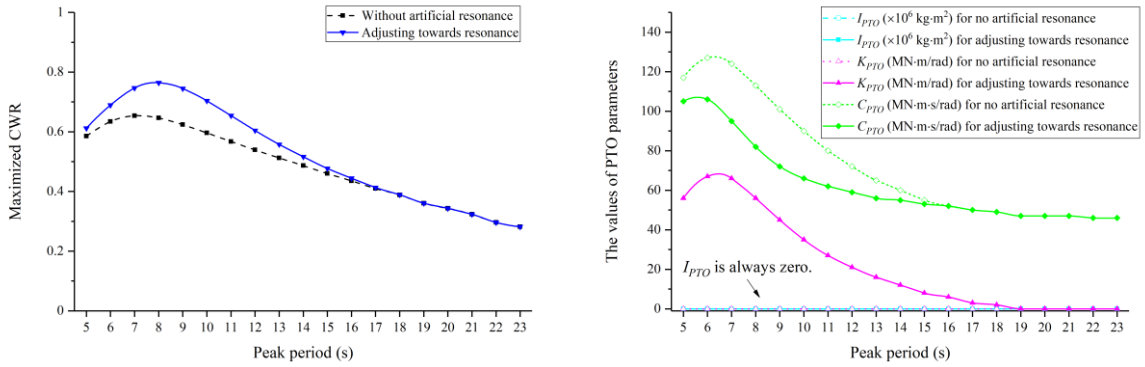

(a) (b)

Fig. 7-7 Results in two adjusting methods of maximizing the CWR under shoaling irregular waves: (a) Maximized CWR; (b) PTO inertia torque, stiffness, and damping.

7.4 Conclusions in the Chapter

This chapter employed frequency-domain BEM to discuss the applications of resonant adjustment by controlling the PTO parameters for enhancing the hydrodynamic. Some conclusions are described as follows:

(1) For the current study mode, an Oyster 800-like OWSC, the drag coefficient $C_d = 5.8$ in frequency-domain BEM is calibrated with CFD results, and certified to be applicable for regular and irregular waves with highly efficient computation and acceptable accuracy.

(2) Compared with adjusting PTO damping only, the approaches with artificial resonant adjustment, e.g., changing PTO stiffness under short regular waves and altering PTO inertia under long regular waves, provides a broader resonant bandwidth and can be successfully applied for a flap-type absorber to enhance the capturing power.

(3) Perfect resonance in regular waves is not the best situation for wave energy harvesting, because the relatively large value of damping item (in Section 7.3.3) in perfect resonance is remarkedly detrimental to the CWR.

(4) Altering PTO inertia or stiffness exhibits a powerful capacity of phase control. Under regular waves, the optimal hysteretic phase angle of velocity relative to wave torque gradually upgrades with the increase of wave period.

(5) Adjustment of PTO inertia does not work for promoting CWR under irregular waves, however, PTO stiffness adjustment is still helpful to enhance the hydrodynamic performance at short peak periods.

In this chapter, some nonlinear behaviors are considered, such as nonlinear hydrostatic restoring moment and nonlinear drag moment. However, there are some limitations, for

example, the constant value of drag coefficient and low wave conditions. Besides, the PTO parameters represent an ideal mathematical model of PTO system, possibly different from a realistic PTO system. However, the performance enhancement via adjusting these PTO parameters is also meaningful to understand the OWSC working principles and control strategies. A part of contents in Chapters 1–4 and this chapter was submitted to Renewable Energy ([2] in Publications). The status is under review when the dissertation is submitted.

8 Optimization of OWSCs under Irregular Waves

8.1 Introduction

The genetic algorithm (GA), an evolutionary optimization method introduced by Holland John (1992), has been widely applied to the optimization of an OWSC (Renzi et al., 2017; Calvário et al., 2020), an array of OWSCs (Tay and Venugopal, 2017a; Liu et al., 2021b), and a three-body WEC (Wang and Ringwood, 2021) for a single objective function that maximizes the CWR. The multi-objective genetic algorithm (MOGA) optimization of a buoy-like WEC was performed by Koh et al. (2015) with two objectives: simultaneously maximizing the capturing power and minimizing the costs. However, MOGA optimization of OWSCs has rarely been simulated by previous researchers.

In this chapter, the time-domain BEM was utilized and the study model was a new-design assembling OWSC. Bretschneider-Mitsuyasu spectrum was used because of its wide application in the target wave energy farms around Japan. The first objective is to present the nonlinear time-domain hydrodynamic mathematical model of 3D surface-piercing OWSCs under irregular waves in shallow water, considering the nonlinear hydrostatic restoring stiffness, viscous drag, and nonlinear PTO moment, based on linear hydrodynamics, assuming a linear relationship between the wave force and incident wave amplitude. Whilst the second aim is to find the optimal configuration of the OWSC geometric sizes and PTO parameters by MOGA for the target wave energy farm. In addition, parametric studies and local sensitivities were also formulated.

8.2 Environmental Loads Related to Wet Surface

Considering the variations in the instantaneous wet surface due to the volumetric displacement of water under waves, $M_H(t)$ can be written as a form of the sum of a small-angle stiffness and an additional stiffness,

$$M_H(t) = -\left\{\left(F_B \cdot \overline{BH} - mg \cdot \overline{GH}\right) + \frac{1}{2}\rho g w b d_a^2 \cdot \tan^2\{min[|\varphi(t)|, \varphi_m]\}\right\} \cdot \sin\varphi(t) \tag{8-1}$$

To compute drag moment, $h_w(t)$ can be expressed as.

$$h_w(t) = min[d_a/cos\,\varphi(t)\,, h] \tag{8-2}$$

Substituting Eq. (8-2) into Eq. (3-12), $M_D(t)$ can be achieved.

The excursion of the flap has to be constrained to prevent the large pitch rotational angle, especially under severe sea conditions. An additional nonlinear damper (Gomes et al., 2015) is introduced and can be active as a brake above a given threshold angle. Considering the mass, the stiffness, the damping and the friction of PTO system, the total moment of PTO system $M_{PTO}(t)$ is given by

$$M_{PTO}(t) = -I_{PTO}\ddot{\varphi}(t) - [C_{PTO} + C_B(t)]\dot{\varphi}(t) - K_{PTO}\varphi(t) - M_f(t) \tag{8-3}$$

where $C_B(t)$ is the nonlinear braking damping, which is applied when $\varphi(t) \cdot \dot{\varphi}(t) > 0$,

$$C_B(t) = \begin{cases} 0, & |\varphi(t)| \le \varphi_{b,i} \\ \left[3\left(\dfrac{|\varphi(t)| - \varphi_{b,i}}{\varphi_{b,f} - \varphi_{b,i}}\right)^2 - 2\left(\dfrac{|\varphi(t)| - \varphi_{b,i}}{\varphi_{b,f} - \varphi_{b,i}}\right)^3\right] \cdot C_b, & \varphi_{b,i} < |\varphi(t)| < \varphi_{b,f} \\ C_b, & |\varphi(t)| \ge \varphi_{b,f} \end{cases} \tag{8-4}$$

where $\varphi_{b,i}$ is the angle when the brake starts to work; $\varphi_{b,f}$ is the angle above which the brake damping becomes constant; C_b is a constant brake damping coefficient.

To solve the dynamic equation of the new OWSC design in this chapter, the number of sinusoidal wave components, N_w in Eqs. (2-1), (3-1), (3-14) and (3-15), is set to 50 with the equally spaced frequencies from 0.1 to 4 $\mathrm{rad/s}$, which are also used in the computation of impulse response function $R(t)$ in Eq. (3-4). For the convolution integral in Eq. (3-3), only the contribution of the first 20 s is retained, because the value of $R(t)$ after 20 s drops to below 0.03% of the initial value $R(0)$ (Gomes et al., 2015). For the stability of the results in the 4th-order Runge–Kutta integral scheme, the time step is set to $dt = T_{1/3}/100$, which was tested successfully with a small difference of $\varphi(t)$ from the smaller time-step cases. To ensure convergence for a few cases with extreme parameters, such as a large C_{PTO}, the automatic reduction of the time step (e.g., $dt = T_{1/3}/150$ for the first convergent difficulty, $dt = T_{1/3}/200$ for the second convergent challenge, and so on) can effectively result in a stable and efficient numerical computation.

The various parameters of a braking damper in Eq. (8-4) will be given in Section 8.3, and the selection of the drag coefficient C_d in Eq. (3-12), relied on the OWSC geometry, will be discussed in Section 8.4.

8.3 The Design of an Assembling OWSC and Its Performance Evaluation

8.3.1 Target Wave Energy Farm

The target wave energy farm is shown as a red rectangular frame in Fig. 1-1. It should be noted that the wave resource at the target area, known as a typical low-density wave energy location in contrast with EMEC's Billia Croo wave test site, UK, where Oyster 800 was installed (red point in Fig. 1-1), is 12–17 kW/m.

The statistical databases of the wave conditions for the target wave energy farm (Fig. 8-1a) were analyzed by National Maritime Research Institute Japan, based on the numerical weather prediction during 10 years, from February 1994 to January 2004, gathered by Japan Weather Association. To estimate the mean annual wave energy resource, a mean scatter diagram for the occurrence probability of each wave state in all areas was represented through a contour graph, as shown in Fig. 8-1b.

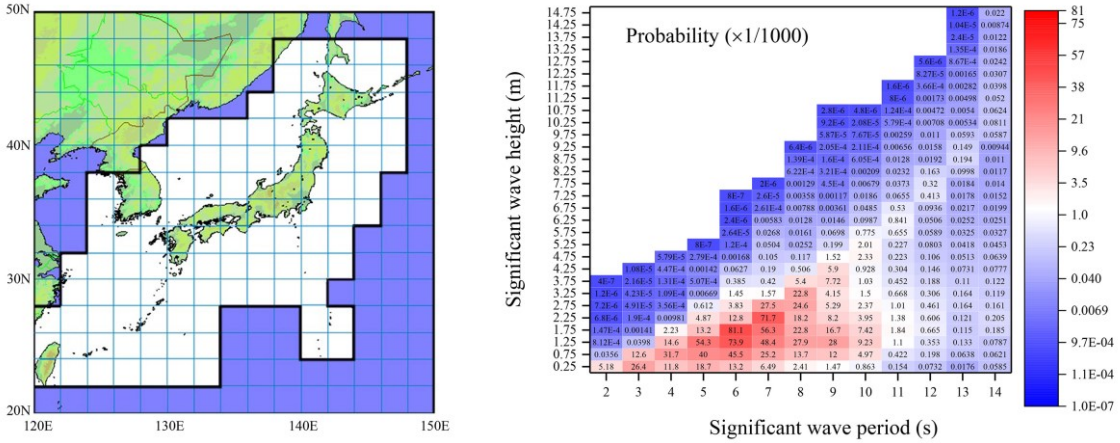

(a) (b)

Fig. 8-1 (a) Target area for wave energy farm; (b) Its scatter diagram in 10 years (National Maritime Research Institute Japan).

8.3.2 An Assembling OWSC

An assembling surface-piercing OWSC was designed and demonstrated in Fig. 8-2, with adaptive sizes, consisting of many hollow boxes and a semi-cylindrical base, for the target wave energy farm of 15 m deep water. The bottom of the OWSC is a semi-cylinder, the radius of which is half of the thickness. A smooth blend of edges at the bottom can reduce the drag moment during the pitch oscillation. To investigate the effects of inertia, the box was designed with the capacity to be filled with water. The box can be either empty or full of water to prevent sloshing. An equivalent water filling percentage was introduced, instead of the number of

water-filling boxes, but realize the same purpose of adjusting the total inertia of the devices. Each plate in the shell of the box and base is 1 cm thick and is made of aluminum alloy, the density of which is $\mathrm{kg/m^3}$. It is assumed that the mass of the bearing is ignored because it is much less than that of the boxes and bases.

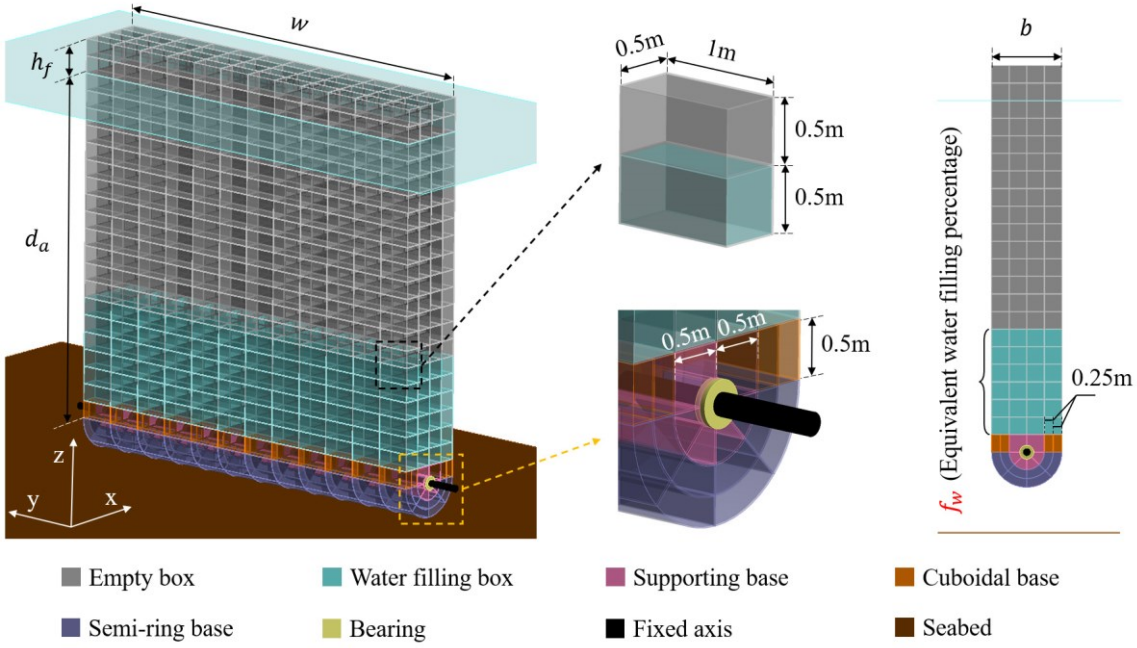

Fig. 8-2 An example model of 12 m wide and 2 m thick OWSC with 1 m height above still water, 10 m distance between hinged axis and still water, and 28.6% water filling, which consists of 720 empty boxes, 288 fully water filling boxes, 12 supporting bases, 48 cuboidal bases (0.25 m × 1 m × 0.5 m) and 96 one-eighth-ring bases.

The mathematical model, based on BEM, cannot consider the effects of the structure above the still water on the wave exciting moment, but can take the change of inertia and hydrostatic restoring moment at a large oblique position for different freeboard heights into account. The energy loss increases when the wave exciting moment is reduced for a short freeboard, which usually causes the OWSC to be submerged under waves (i.e., wave overtopping), especially in high waves (Whittaker and Folley, 2012). To block the wave, freeboard height is set to $h_f = 1$ m, greater than the mean annual wave amplitude of 0.9 m (see National Maritime Research Institute Japan) at the target wave energy farm (Fig. 8-1a). The equivalent water filling percentage f_w is the ratio of the tallness of filling water to the total height of the boxes, except for the cuboidal bases.

Renzi et al. (2017) defined only three variables (width, water depth and hinge height) as design parameters in the optimization of an OWSC. In this study, for a comprehensive

consideration of different designs, three discrete parameters of OWSC geometric sizes and three continuous variables (one for water filling and two for the PTO system), listed in Table 8-1, will be optimized by MOGA in Section 8.5. It should be noted that the water filling cannot be too large to guarantee the capability of restoration with sufficient buoyancy. The design maximum value of f_w is 30%, confirming that $K_0(t) > 0$. For the braking damper of the PTO system, in Eq. (8-4), the following constant values are adopted: $\varphi_{b,i} = 30^{\circ}$, $\varphi_{b,f} = 40^{\circ}$ and $C_b = 1\ \mathrm{GN \cdot m \cdot s/rad}$.

Table 8-1 Design variables of OWSCs and the bounds for each input parameter.

Classification	Input parameters	Physical properties	Lower bound	Upper bound	Interval
Discrete	w (m)	Width	10	18	1
	b (m)	Thickness	1	5	0.5
	h_w (m)	Axis depth underwater	8	12	1
Continuous	f_w (%)	Equivalent water filling percentage	0	30	
	K_{PTO} (MN·m/rad)	Stiffness of PTO system	0	120	
	C_{PTO} (MN·m·s/rad)	Damping of PTO system	10	100	

8.3.3 Performance Evaluation

As an early design stage of a wave energy device, the selection of a wave energy site is critical. The significance of wave energy farm selection should be considered in the performance evaluation. To calculate the mean annual CWR, the effects of water depth can be described in P_{ac} and have no need to be accounted in P_{res}, at least in the early design stage. For example, comparing 15 m and 20 m water depth, the shoaling irregular wave spectrum $S_d(\omega)$ in 15 m-deep water is lower than 20 m water depth. Consequently, P_{res} in 15 m-deep water is also lower than 20 m water depth. However, it is hard to judge the mean annual CWR using an inconsistent value of P_{res} for different water depths.

To evaluate the wave energy absorption capacity with considering the wave energy loss due to the small water depth in the selected wave energy farm, the unabated irregular wave power at infinite water depth is given by

$$P_w = \rho g \int_0^{\infty} C_g(\omega) S(\omega) d\omega \qquad \text{Irregular waves} \tag{8-5}$$

Substituting Eq. (8-5) into Eq. (3-51), the constant value of mean annual wave power resource per unit width P_{res} for infinite water depth can be obtained. According to the scatter diagram (Fig. 8-1b), P_{res} at the target wave energy farm is computed as 13.48 kW/m, which agrees with the forementioned range 12−17 kW/m shown in Fig. 1-1. It implies that the worldwide wave energy resource distribution in Fig. 1-1 represents an unabated value regardless of water depth.

The mean annual CWR, η in Eq. (3-52), which does not rely on the device width, is more appropriate as the design standard of productivity to avoid the situation where a very wide device is obtained as the best design. For the calculation of the CWR matrix and mean annual CWR in this study, the equivalent water filling percentage, PTO stiffness, and PTO damping are constant for all sea states in a given scatter diagram.

The levelized cost of energy (LCOE), measured by the discounting method (Allan et al., 2011), is commonly used in the energy generation industry for the comparison of different concepts. However, it is difficult to determine the parameters for the calculation of the LCOE, for example, cost information and discount rate, during the early design period. To simplify the economic assessment, the structural mass of the flap per unit width m_s without counting the axle, foundation, internal filling water, and PTO system, independent of the width and expected to be as small as possible, is utilized as a representative of economic performance.

8.4 Determination of Drag Coefficient

Bhinder et al. (2012) evaluated the effects of drag forces on the performances of WECs with heave and surge modes, and claimed that the energy loss due to drag forces could be negligible in point absorbers, but the significant effects of drag coefficient were found in the surge mode. Ghafari et al. (2021) ignored the drag of point absorbers and compared the BEM results well with experimental data. However, the selection of the drag coefficient for a flap-type pitching device is essential. Some useful discussions about the drag coefficient of an OWSC can be found in Wei et al. (2015). Next, the drag coefficients of OWSCs under two different circumstances, steady flow and oscillating flow, were numerically estimated.

8.4.1 A Fixed OWSC under Steady Current

For the steady current flow around a fixed vertical flap, the drag coefficient is Re dependent, which is directly proportional to the characteristic length of the device (here the flap width is chosen). The drag coefficient can be computed as

$$C_d = \frac{2F_D}{\rho w h_e v^2} \tag{8-6}$$

where F_D is the drag force, h_e is the height encountering the flow, and v is the incoming current velocity.

To obtain C_d in steady flow, a pseudo 2D fluid field of a horizontal slice ($h_e = 1$ cm) around the fixed flap was simulated using OpenFOAM, as shown in Fig. 8-3. The symmetric computational domain 10w × 3w. The boundary layer is neglected owing to the insignificance of the fluid shear stress relative to the normal stress for a prototype OWSC (Wei et al., 2015).

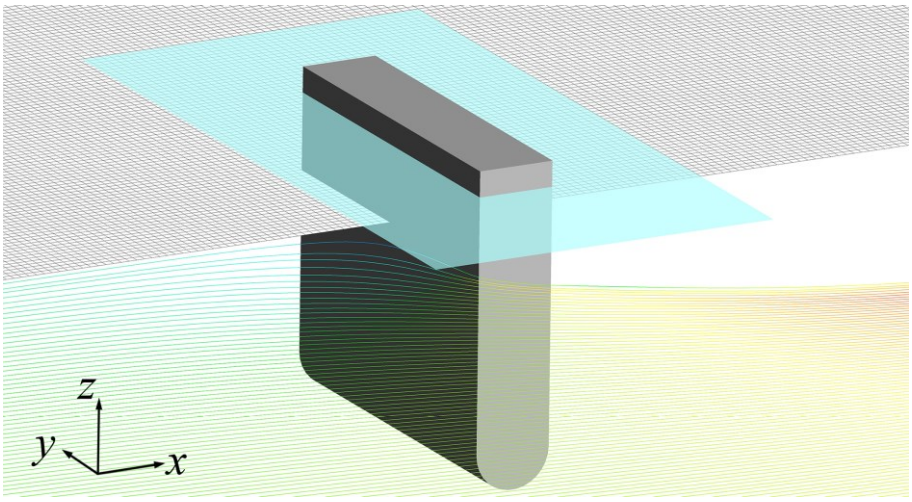

Fig. 8-3 A pseudo 2D steady flow field of a horizontal slice around the fixed flap.

For the mesh-independence validation, a flap with moderate dimensions ($w = 14$ m and $b = 3$ m) was chosen and three different cell sizes were set. From the results of C_d under a current $v = 1$ m/s in Table 8-2, it is observed that the results of the medium mesh are stable, and C_d is no longer sensitive to the smaller mesh size. Accordingly, the medium size was chosen for further studies.

Table 8-2 Test of the mesh independence.

Mesh	Mean size (m)	# of flap	# of water	# of cells	C_d
Coarse	0.45	7 × 16	312 × 94	29.3k	2.370
Medium	0.32	10 × 22	440 × 132	57.9k	2.373
Fine	0.21	15 × 34	668 × 200	134.0k	2.373

Further tests of the effects of width and thickness on C_d , listed in Table 8-3, show that the drag coefficient of the fixed flap in a steady current flow ($v = 1$ m/s) is almost insensitive to the width and thickness. Wei et al. (2015) explained that the full scale OWSC always had a large Re. Moreover, Sarpkaya and Isaacson (1981) stated that C_d may be independent of the Re when the Re exceeds a critical value, i.e., 10^5 for a smooth cylinder. This implies that the assumption of a constant C_d may be appropriate for simply computing the drag force for the prototype OWSC, which usually has a large size and thus a relatively large Re.

Table 8-3 Drag coefficient in steady flow for different width and thickness.

Width (m)	Thickness (m)	C_d
10	3	2.365
14	1	2.371
14	3	2.373
14	5	2.353
18	3	2.380

8.4.2 An Oscillating OWSC under Waves

In contrast to steady flow, the drag coefficient of an oscillating body in waves is related to both KC and Re. KC is inversely proportional to the characteristic length of the device. However, to simplify the computation of the drag moment, a constant value of the drag coefficient has been assumed in some studies. For example, a constant value of $C_d = 1.2$ was utilized for a 2D fully submerged OWSC by Cheng et al. (2019), and $C_d = 1.98$ was selected for a 3D OWSC by Gomes et al. (2015). In their studies, the drag coefficients were estimated empirically. Liu et al. (2022a) scanned a range of C_d values and performed a calibration with CFD simulations using OpenFOAM; $C_d = 5.4$ was applied to an Oyster 800-like OWSC. Babarit et al. (2012) stated that the selection of the drag coefficient for an oscillating OWSC was subject to some uncertainty. Therefore, a more accurate value of the drag coefficient should be obtained experimentally or numerically.

Although the width is usually chosen as the characteristic length in the estimate of KC and Re, the thickness can also be considered as the characteristic length if the effects of thickness

are of interest (Schmitt and Elsäßer, 2017). Based on the expression of the drag moment in Eq. (3-12), it is found that the effects of thickness, unlike the width and height, can be only considered in the value of drag coefficient. However, it was reported by Lin et al. (2018) that a larger drag force may occur at the sidewalls of the thick flap in waves. This implies a closer correlation between the drag coefficient and the thickness of the oscillating bodies under waves. As shown in Table 8-1, the variation in thickness (the upper bound is five times the lower bound) in the design is relatively larger than the width and axis depth. Based on the discussions above, the drag coefficient is assumed to be independent of the width and height, and only depends on the thickness.

To determine the drag coefficients in the oscillating flow for different thicknesses, 3D transient simulations, based on CFD, of flaps ($w = 14$ m and $d_a = 10$ m) for different thicknesses without the PTO system under a long-period irregular wave ($T_{1/3} = 14$ s and $H_{1/3} = 1.8$ m) were performed in OpenFOAM, in which the computational domain (the medium cell size in Table 8-2 are utilized in the refined zone near the flap and the still water surface shown in Fig. 8-4), the overset dynamic mesh method and other settings follow (Liu et al., 2022a). It was demonstrated by Liu et al. (2021a) that the variation in the drag coefficient has a larger effect on the hydrodynamic performance under long waves. This can explain why a long-period irregular wave in the target wave energy farm was chosen. The selected significant wave height is a representative value that is equal to the most frequent wave height in the target wave energy farm (National Maritime Research Institute Japan).

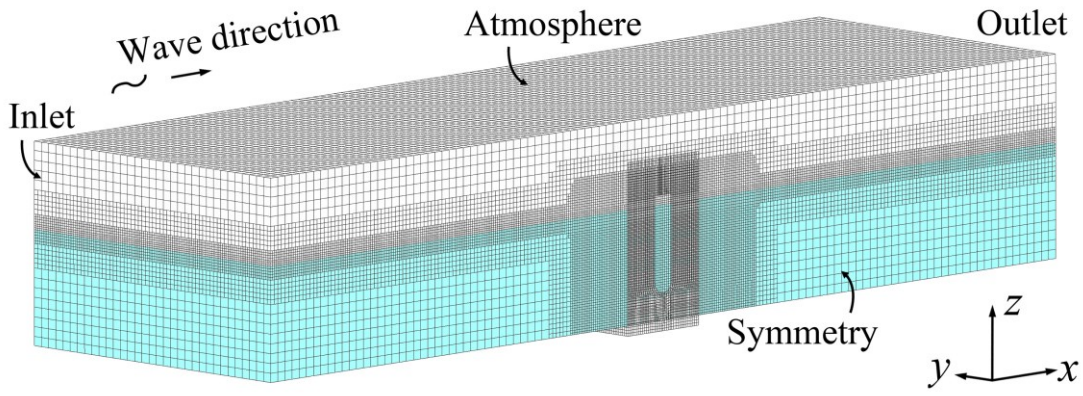

Fig. 8-4 A 3D transient simulation model of the flap in NWT, based on the CFD.

A range of C_d values from 1 to 18 are scanned to find the most suitable value for various thicknesses by screening the minimum error of normalized kinetic energy in a duration (20–90 s) between BEM and CFD. The error of the normalized kinetic energy can be expressed as

$$Error = \frac{\left|E_k^{BEM} - E_k^{CFD}\right|}{E_k^{CFD}} \tag{8-7}$$

where $E_k = \int_{20}^{90} \dot{\varphi}^2(t)dt$ is the normalized kinetic energy, and the superscripts BEM and CFD refer to the simulation methods. Negligible differences of < 0.5% were found in the hydrodynamic coefficients obtained from NEMOH for different mesh sizes of the flap surface, as shown in Fig. 8-5. It was also presented by Liu et al. (2022a) that the hydrodynamic coefficients are insensitive to the mesh size in the BEM. Finally, the medium mesh (12 × 14 × 20 on the flap surface above the hinge and 16 divisions on the bottom round) was chosen for further studies.

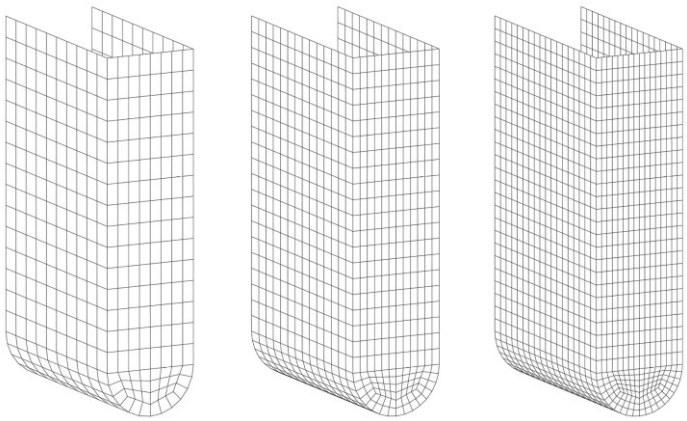

Fig. 8-5 Mesh models in NEMOH, based on the BEM, for the calculation of hydrodynamic coefficients.

Fig. 8-6a–e shows the comparison of time–history response of the flaps for different thicknesses between BEM and CFD. The selection of C_d in the BEM corresponds to the minimum $Error$. In contrast to the steady flow, the selected values of C_d in the oscillating flow are affected by the variation in b. A quadratic fitting curve of C_d vs. b is shown in Fig. 8-6f and will be utilized in the subsequent optimization analysis and case studies.

$$C_d = 0.793b^2 - 1.567b + 2.86 \tag{8-8}$$

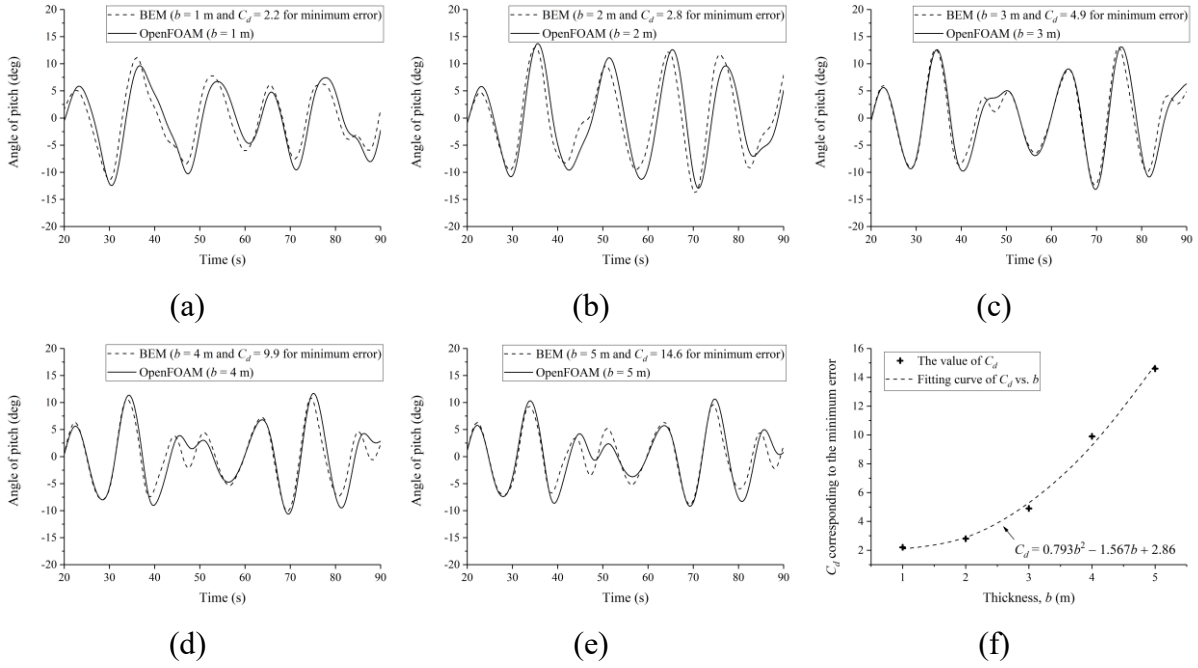

Fig. 8-6 Comparison of time–history response, between BEM collaborating with the value of C_d corresponding to the minimum error and CFD methods, of the flaps for different thickness: (a) b = 1 m; (b) b = 2 m; (c) b = 3 m; (d) b = 4 m; (e) b = 5 m; (f) Quadratic fitting curve of C_d vs. b.

Obviously, there is a significant difference in the selection of the drag coefficients for OWSCs under steady flow and oscillating flow. The relative velocity $\dot{\varphi}(t)r - u_n(t)$ in Eq. (3-12), which is the difference value between the theoretical water particle velocity in the absence of the flap and the actual flap velocity, may vary from the actual water particle velocity relative to the oscillating flap. Therefore, considering the oscillating flow experimentally or numerically in the selection of the drag coefficient for an OWSC under waves is critical when applying the Morison equation to estimate the drag force in the BEM.

The computational cost to model the response of an OWSC under the irregular wave in OpenFOAM with eight processors on a desktop of 3.4 GHz CPU and 32 GB RAM is approximately 85 h for a 90 s simulation. However, it takes approximately 1 min to run the Python code based on the BEM for a given array of random phases with one processor for the same duration of simulation. Owing to the high computational cost of CFD, the nonlinear mathematical model based on BEM can provide efficient computation and acceptable accuracy after calibrating drag coefficients with a few high-fidelity CFD simulations.

8.5 Optimization of OWSC and PTO Parameters Using MOGA

GA is a widely applied approach to search for the optimal solution for various optimization problems based on evolution theory, which features the gradual elimination of bad individuals from a group, to ensure that the best offspring survive in the next generation. In a multi-objective optimization analysis, a problem with conflicting objectives (e.g., to maximize the power generation and minimize the costs) usually has not one but multiple optimal solutions, unlike the single solution for single-objective optimization. These optimal solutions are represented through the Pareto front, which represents the group of solutions, where selecting any one solution in place of another always sacrifices quality for at least one objective, while improving quality for at least one other. A generic workflow of the MOGA is illustrated in Fig. 8-7. The initial population is created by design of experiment (DOE) (Fisher, 1936) sampling from the design space, and the new generations evolve through crossover and mutation processes (Mitchell, 1998), until the convergence criterion is reached after several iterations. The details of the MOGA optimization process are described below.

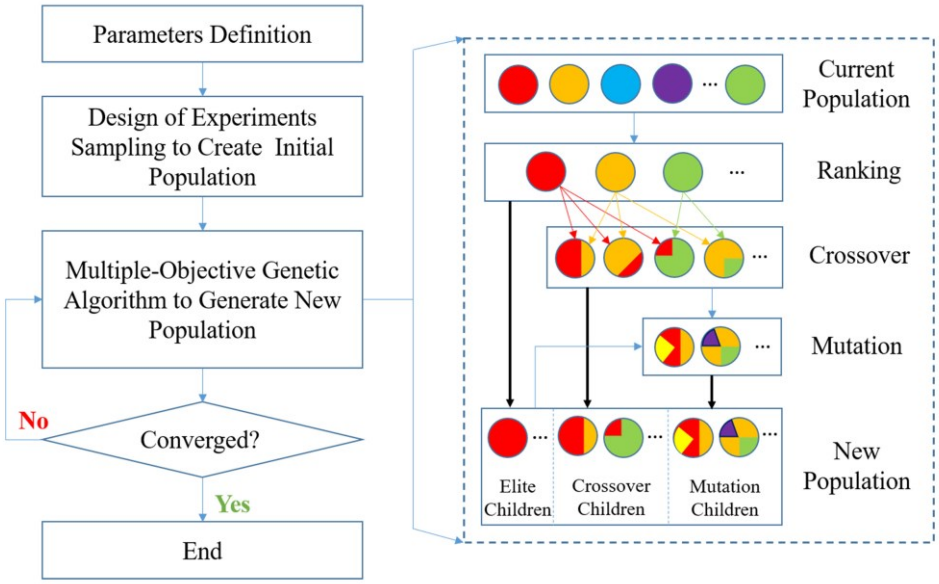

Fig. 8-7 A generic workflow of the MOGA optimization method.

8.5.1 Design of Experiments

For well-proportioned filling in the entire design space and simultaneously efficient computation, a proper sampling method is important. The equally spaced sampling method for discrete parameters and the Latin hypercube sampling (LHS) method (Mckay et al., 2000) for continuous parameters were used. To reduce the initial population for efficient computation,

the discrete parameters of w and b are extracted with every two intervals as the sampling step, that is, by varying both w and b five times. In LHS, the contribution of all the continuous parameters with four variations for each to the total number of initial samples can be considered as the same work for a single parameter changing four times (see Mckay et al., 2000). Therefore, the number of individuals in the initial population can be calculated as $5 \times 5 \times 5 \times 4 = 500$.

8.5.2 MOGA Processing

A Python code was developed to run the MOGA processing, a loop of ranking, crossover, and mutation, for gradual aggregation to the fittest solutions until convergence. A population size of 150 individuals (including two elite children, 100 crossover children, and 48 mutation children) was employed for each generation in the MOGA.

8.5.2.1 Ranking Based on Weighted Objective Function

For a multi-objective problem, there are usually multiple fittest solutions (Pareto front). All individuals in a generation are ranked based on the weighting factor of each objective function. The weighted objective function, which is a combined function of multiple objectives, is applied and given by

$$\Phi = \sum_{j=1}^{N_o} W_j \cdot O_j \tag{8-9}$$

where N_o is the number of objective functions; W_j is the weighting factor for the jth objective function, and agrees to $\sum_{j=1}^{N_o} W_j = 1$; O_j is the normalized objective function,

$$O_j = \left(\frac{\left| P_{o,t} - P_o \right|}{P_{o,max} - P_{o,min}} \right)_j \tag{8-10}$$

where P_o is the output parameter; $P_{o,max}$ and $P_{o,min}$ denote the minimum and maximum values of all the output parameters in the current population, respectively; $P_{o,t}$ is dependent on the target of optimization,

$$P_{o,t} = \begin{cases} P_{o,min} & \text{if objective is minimization} \\ P_{o,max} & \text{if objective is maximization} \end{cases} \tag{8-11}$$

All individuals in the current generation are subsequently ranked by ascending magnitudes of the value Φ. In this study, there are two objective functions: (1) to maximize the mean annual CWR η with the weighting factor W_1 and (2) to minimize the structural mass per unit width m_s

with the weighting factor W_2. For the equal consideration of productivity and expenditure, set $W_1 = W_2 = 0.5$.

8.5.2.2 Elite Children

Individuals with the top-ranking order in the current generation are guaranteed to survive to the next generation, called elite children. They usually help to fasten the convergence, but a large number of elite children will cause the best individual continuously dominate multiple generations and even reach a pseudo convergence, i. e., the optimal candidate found by MOGA may be not the fittest solution. In this study, two elite children are directly selected from the top ranking of the current generation, and will still become either the parents for crossover or the children for mutation.

8.5.2.3 Crossover Children

Crossover combines two parents to produce a new child, with the expectation that the offspring can be better than both of the parents if it takes the best genes from each of the parents. A crossover child is produced, according to the following equation,

$$Crossover\ Child = \delta_c \cdot Parent\ 1 + (1 - \delta_c) \cdot Parent\ 2 \tag{8-12}$$

where $Parent\ 1$ and $Parent\ 2$ are selected from the current population; δ_c is a bias factor between 0 and 1, being closer to 1 when the chromosome of $Parent\ 1$ dominates. It ensures all the crossover child laying on the line between the parents, shrinking gradually around the optima during the iterations. The parents for the next generation are chosen based on ascending ranking of the weighted objective function. A high-ranking individual can be selected more than once as a parent, in which it contributes its genes to more than one child. Specially, the discrete parameters of a crossover child might be not in the list of allowable values. To solve this problem, adjustment of a discrete parameter to either become closer allowable value or extrapolate to two allowable values at both sides can be applicable. In the extrapolation, if there are X discrete parameters of a crossover child outside the list of given values, one child will be replicated and extrapolated to create 2^X crossover children.

In the present study, there are three following ways to combine between (1) two top-ranking individuals, (2) a top-ranking individual and one from Pareto Fronts, (3) two from Pareto Fronts. The top-ranking individuals are selected no matter whether one of them is or not Pareto Front, so that it is necessary to remove the identical offspring when some parents are

either top ranking or Pareto Front. It is noted that the total amount of crossover children is dependent on the number of selected top-ranking individuals. For each generation, one hundred crossover children are created at the midpoints of the line between the parents, i. e., $\delta_c = 0.5$ in Eq. (8-12), with increasing the number of selected top-ranking individuals until the generated crossover children over the design value, and then randomly remove the redundancies. Once a discrete parameter of crossover child locates between two allowable values, extrapolation will be applied.

8.5.2.4 Mutation Children

Mutation randomly alters gene values and can produce totally new gene in the gene pool. It helps to prevent the population from stagnating at any local optima. The discrete parameter mutates its value by a particular interval, whereas, for the continuous parameter, the mutation occurs according to the following equation,

$$Mutation\ Child = Child + \delta_m \cdot (Upper\ Bound - Lower\ Bound) \tag{8-13}$$

where δ_m is a small and random variation, which allows the limited change of the genes and simultaneously satisfy the constraint of the bounds. The $Child$ in Eq. (8-13) can be either elite child or crossover child.

In the current study, 48 mutation children are randomly selected from generated children, then mutate one or two values for each child with small extent, e. g., one interval variance for discrete parameters and an adaptive δ_m from -0.2 to 0.2 in Eq. (8-13) for continuous parameters, and finally, adjust to fulfill the constraint of bounds, e. g., normal projection to the boundary if the mutation child stands outside the design space.

8.5.3 Optimized Results

The optimization process is judged to converge when the differences between the optimal candidate of all parameters (including input parameters and objective functions) in the current generation and the previous generation are less than 0.5%, as the convergence criterion. Regardless of the inertia and friction of the PTO system in the optimization, MOGA successfully produced the converged solution in the 21st generation, and an additional five iterations were performed to confirm the optimal solution invariable.

The design parameters and results of the optimal configuration are listed in Table 8-4. It shows that the mean annual CWR for the optimal design is 0.358, which is slightly lower than

that of Oyster 800 ($\eta = 0.459$), calculated using Eq. (3-52) according to $P_{ac} = 800$ kW, $w = 26$ m (Renzi et al., 2017) and $P_{res} = 67$ kW/m (shown as the red point in Fig. 1-1), mainly because water is allowed to flow below the flap in this study, but the flow under Oyster 800 is obstructed by a base support, which was shown in Henry et al. (2018) to have a significant impact on the wave torque and power capture. Another reason is the consistent water filling and invariable PTO parameters in different wave climates in the current study. In addition, the different characteristics of the wave climate in the target wave energy farm and the northwest coast of Europe, where Oyster 800 is located, may also cause discrepancies in the hydrodynamic performance.

Table 8-4 Design parameters and results of the optimal configuration found by MOGA.

w (m)	b (m)	d_a (m)	f_w (%)	K_{PTO} (MN·m/rad)	C_{PTO} (MN·m·s/rad)	E_{ac}	m_s (t/m)
16	1	12	0	87.2	70.6	0.358	3.93

In fact, the optima is an idealized result, which does not consider friction and other energy losses, for example, wave overtopping. The CWR matrix for the optimal configuration shown in Fig. 8-8 reveals the highest performance existing at the significant wave periods from 5 to 6 s, which are nearly matched with the scatter diagram (Fig. 8-1b). The CWR mainly depends on the significant wave period, but slight correlations with the significant wave height are also inferred.

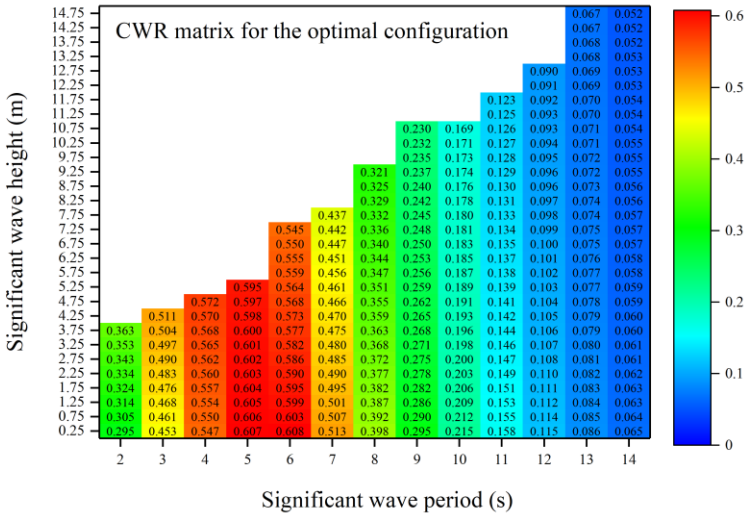

Fig. 8-8 CWR matrix for the optimal configuration.

For a given geometry, PTO system, and scatter diagram, the computation of the mean annual CWR, which is the average value of the results for five different arrays of random phase, involves a cost of approximately 5 h to run the Python code with one processor on the same desktop (see Section 8.4).

8.6 Parametric Study and Local Sensitivity

To comprehend the effects of each input parameter, the parametric studies were performed, and subsequently, the most sensitive parameters for the mean annual CWR and the structural mass per unit width were determined. The parameters of the OWSC model and PTO system in Table 8-4 were employed for the parametric studies aside from additional elucidation.

8.6.1 Effects of Width

The mean annual CWR and structural mass per unit width results for different widths are shown in Fig. 8-9a. It is observed that the mean annual CWR increased noticeably when the width increased from 10 to 16 m, but decreased slightly when the width increased from 16 to 18 m. The structural mass per unit width is independent of the width. The averaged values of CWR for the different significant wave heights at the same significant wave period, called averaged CWR, for different widths are shown in Fig. 8-9b. For a narrow OWSC, for example, 10 m width, the highest CWR occurs when the significant wave period is 4–5 s, but the CWR is lower than 0.1 when the significant wave period is greater than 10 s. With increasing width, the CWR diminishes under short waves and increases under long waves. Consequently, there should be a fittest width to enhance the mean annual CWR at a target wave energy farm to coordinate well with its scatter diagram.

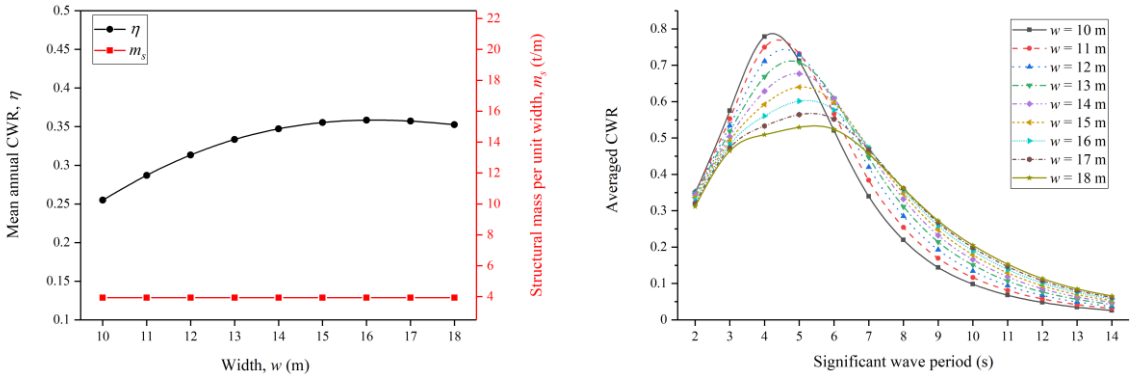

(a) (b)

Fig. 8-9 (a) Mean annual CWR and structural mass per unit width for different values of width; (b) Curves of averaged CWR vs. significant wave period for different width.

8.6.2 Effects of Thickness

It is observed in Fig. 8-10a that the values of η first increase and then decrease with the increase of thickness, but m_s always grows. In Fig. 8-10b, the larger thickness results in the decline in CWR under very short waves, e.g., the significant wave period is 2 s, but an intermediate thickness leads to high averaged CWR at the significant wave period from 5 to 7 s (near the most frequent wave period in the target wave energy farm), which explains why the largest value of η occurs when $b = 2.5$ m. When the significant wave period is greater than 8 s, the differences in the averaged CWR for various thicknesses become slight. The numerical results from (Van't Hoff, 2009) showed that the thickness influence of hydrodynamic coefficients was quite small, because only a narrow range of thickness from 0.2 to 1.8 m was studied. Fig. 8-11 presents the added inertia torque, radiation damping and wave exciting moment of a flap ($w = 16$ m and $d_a = 12$ m) for different thicknesses from 1 to 5 m. As a result, the variations in these hydrodynamic coefficients are small when the wave period is less than 5 s, but the differences are apparent at larger wave periods. Renzi et al. (2014b) indicated that the power absorption of the OWSC was mainly driven by the wave exciting moment. It was found from Fig. 8-11c that the wave exciting moment of a thick OWSC is fundamentally greater than a thin one when the significant wave period is greater than 5 s. The increase in thickness promotes the wave exciting moment, but a larger drag coefficient is detrimental to the hydrodynamic performance. In addition, it also significantly increases the material consumption. Accordingly, the unbiased trade-off between high η and low m_s yields the fittest value of thickness (see Table 8-4) at its lower bound (see Table 8-1), because the impact of thickness on the economics is much stronger than on the mean annual CWR.

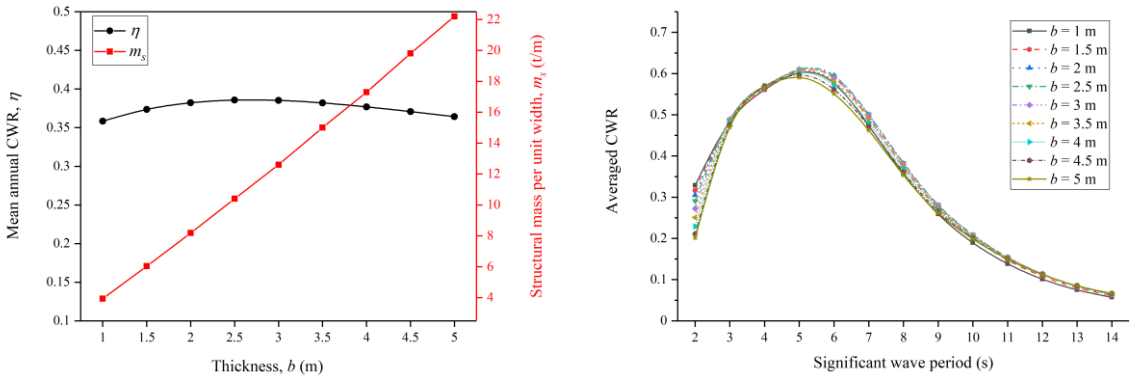

(a) (b)

Fig. 8-10 (a) Mean annual CWR and structural mass per unit width for different values of thickness; (b) Curves of averaged CWR vs. significant wave period for different thickness.

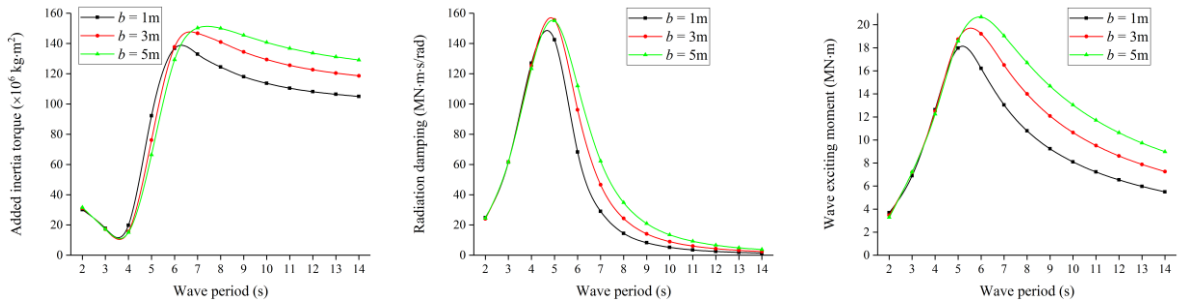

(a) (b) (c)

Fig. 8-11 Hydrodynamic coefficients of a 16 m-wide flap for various values of thickness: (a) Added inertia torque; (b) Radiation damping; (c) Wave exciting moment.

8.6.3 Effects of Axis Depth

Fig. 8-12a shows the mean annual CWR and structural mass per unit width results for different values of axis depth. The mean annual CWR is significantly promoted with increasing axis depth because a larger value of axis depth can enlarge the working surface of the OWSC. By comparing the curves in Fig. 8-12b, when the axis depth increases from 8 to 11 m, the CWR almost increases in the whole range of wave periods. However, when the axis depth increases further to 12 m, the CWR decreases in the range of wave periods from 2 to 6 s, owing to the enormous viscous drag moment. Therefore, increasing the axis depth can be favorable for increasing the wave exciting moment or disadvantageous owing to the increment in viscous drag moment.

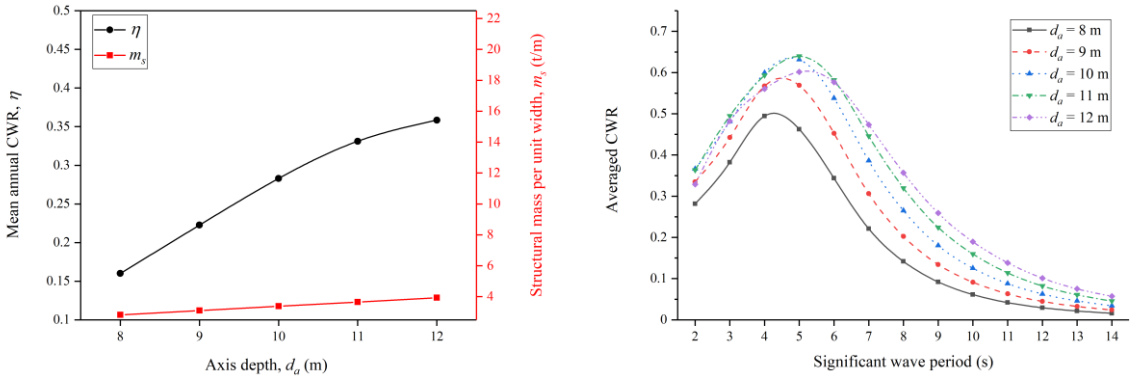

(a) (b)

Fig. 8-12 (a) Mean annual CWR and structural mass per unit width for different values of axis depth; (b) Curves of averaged CWR vs. significant wave period for different axis depth.

In the current study, the design water depth is only 15 m, so the monotonic relationship between the limited axis depth and the mean annual CWR cannot adequately prove that the increasing axis depth must lead to a higher mean annual CWR. The structural mass per unit

width increased marginally with the incremental axis depth. The critical impact on the mean annual CWR and slight influence on the structural mass per unit width collectively conduces to the upper bound (see Table 8-1) of the axis depth as the optimized solution (see Table 8-4).

8.6.4 Effects of Equivalent Water Filling Percentage

Fig. 8-13a shows that the equivalent water filling percentage contributes very little to the mean annual CWR. Quantitatively contrasting the results for maximum water filling in Fig. 8-13b with Fig. 8-8, which denotes the results without water filling, it is observed that the OWSC with larger water filling captures a little more power under long waves, which is in agreement with Chow et al. (2018), but has slightly lower CWR under short waves, e.g., when the significant wave period is less than 7 s. Summarizing the decay under short waves and growth under long waves, the mean annual CWR characterizes steadiness. In the real operation of an OWSC, the inertia adjustment by filling water, which turns the natural period up (Ning et al., 2017), is possibly an ineffective control strategy to enhance the absorbed power in rough seas.

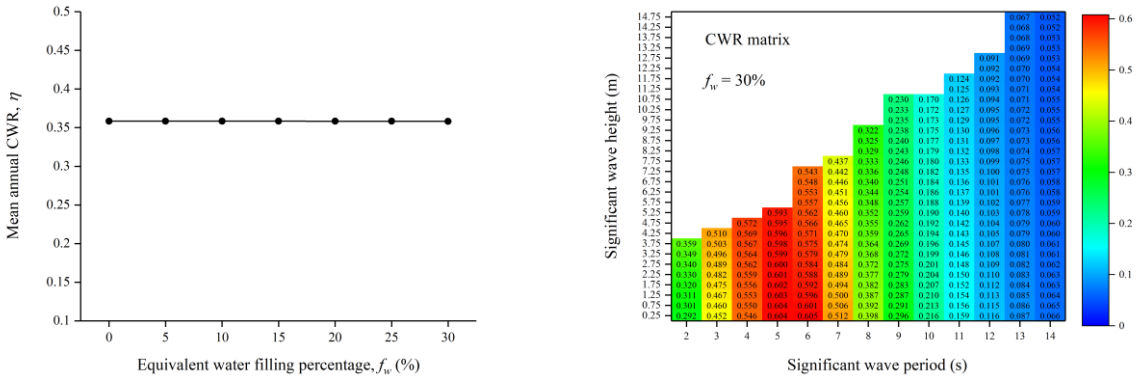

(a) (b)

Fig. 8-13 (a) Mean annual CWR for different values of equivalent water filling percentage; (b) CWR matrix for f_w = 30%.

8.6.5 Effects of PTO Stiffness

The mean annual CWR results for various values of the PTO stiffness are shown in Fig. 8-14a, indicating that there should be a fittest PTO stiffness corresponding to the highest mean annual CWR. To understand the effects of the PTO stiffness under different wave conditions, the averaged CWRs for different values of PTO stiffness are shown in Fig. 8-14b. It should be noted that the comprehensive promotion of CWR occurs over the entire range of wave periods when configuring a PTO torsional spring with an intermediate stiffness, for example, K_{PTO} =

60 MN · m/rad, in contrast to the case without PTO stiffness. Nevertheless, an extremely large value of PTO stiffness, for example, $K_{PTO} = 120$ MN · m/rad, can negatively affect the CWR under long waves but shows a positive influence under short waves. An increase in PTO stiffness can shift the natural period to lower values (see Renzi et al., 2014b), and the capture power can thus be promoted because of the dynamic amplification of the pitch motion when the natural period is close to the dominant wave period. Significant dynamic amplifications of a floating WEC under regular waves near certain periods were observed experimentally in Ribeiro e Silva et al. (2021). Consequently, the adjustment of PTO stiffness to regulate the torsional stiffness can be a control strategy for a high CWR, for example, by adding or removing the torsional springs on/from the hinge, according to the forecast of sea climates.

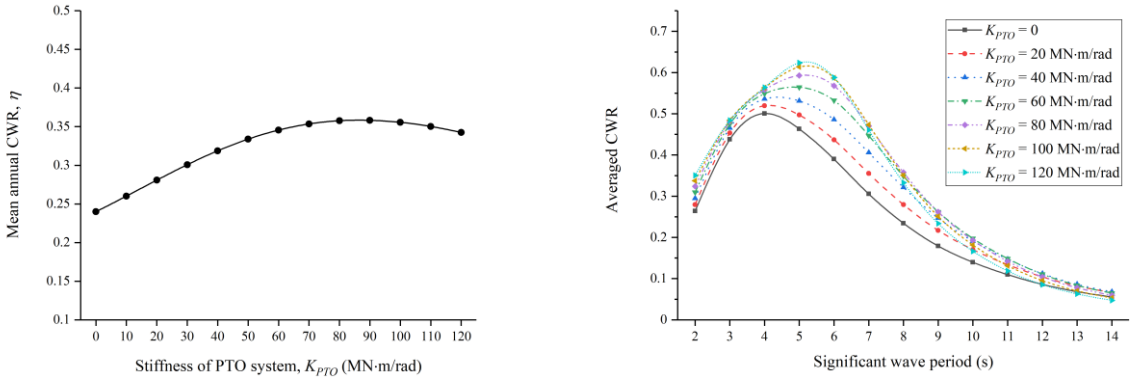

(a) (b)

Fig. 8-14 (a) Mean annual CWR for different values of PTO stiffness; (b) Curves of averaged CWR vs. significant wave period for different PTO stiffness.

8.6.6 Effects of PTO Damping

Fig. 8-15a shows that the mean annual CWR rapidly increases with the increase of PTO damping from 10 to 50 MN · m · s/rad, gradually becomes steady until the maximum value (see Table 8-4), and slightly decreases with the further increment of PTO damping. When it is difficult to determine the precise value of PTO damping by the controller for some sea states, a large value instead of a very small value is recommended to weaken the capture energy loss. It is noted in Fig. 8-15b that the thorough growth of the averaged CWR appears in the whole range of wave periods when installing an intermediate PTO damping, e.g., $C_{PTO} = 70$ MN · m · s/rad. A further increase in PTO damping assists with a slight growth of the CWR only when the significant wave period is 4–6 s, but brings slightly negative impacts at the other periods.

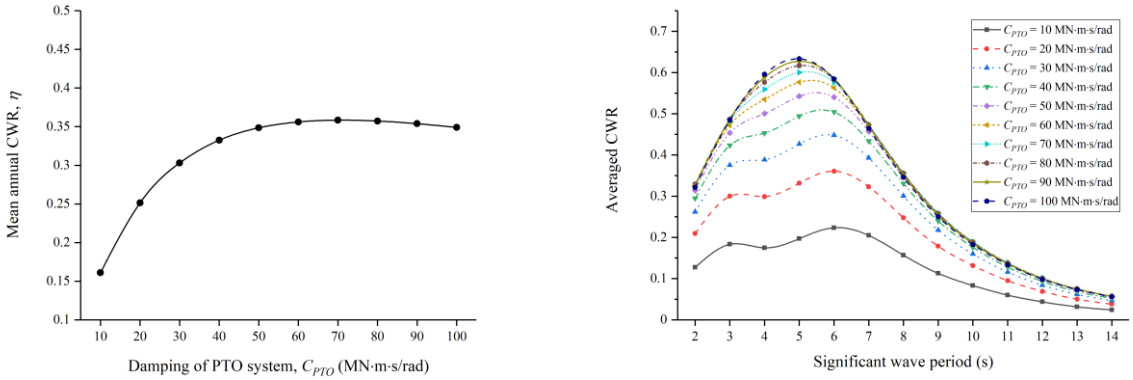

(a) (b)

Fig. 8-15 (a) Mean annual CWR for different values of PTO damping; (b) Curves of averaged CWR vs. significant wave period for different PTO damping.

8.6.7 Effects of PTO Friction

Under small waves, it is very difficult for a hydraulic PTO system, which is usually utilized for OWSCs, to produce electricity, because of friction and other factors (Plummer and Schlotter, 2009). To understand the effects of friction on the capturing power, the energy loss is defined as

$$E_{Loss} = \frac{P(T_{PTO} = 0) - P(T_{PTO} > 0)}{P(T_{PTO} = 0)} \tag{8-14}$$

where P is the capturing power and agrees with either $P = P_c(H_{1/3}, T_{1/3})$ for the energy loss matrix assembled from the results of multiple wave conditions, or $P = P_{ac}$ for the mean annual energy loss. This study follows the assumption that the energy loss percentage due to friction is expected to be approximately 5% in real operations (Henderson, 2006). Fig. 8-16a shows that the mean annual energy loss has an approximately linear relationship with the frictional moment of the PTO system. The frictional moment of the PTO system is linearly interpolated as 167.2 kN·m when the energy loss is 5%. The distribution of the energy loss for different wave conditions is shown in Fig. 8-16b. For each wave period, the energy loss decreased with increasing significant wave height. Subtracting the constant frictional moment from the wave exciting moment, a high wave produces a larger torque to the generator than a small wave. Under small waves, the maximum energy loss reached 80%. However, the energy loss is lower than 40% in the range of significant wave periods from 4 to 8 s even when the significant wave height is down to 0.25 m. Consequently, the wave period zone corresponding to the low energy loss should be near the energy peak period to reduce energy loss. In addition, to achieve high mean annual CWR, the development of a PTO system with low friction is also required.

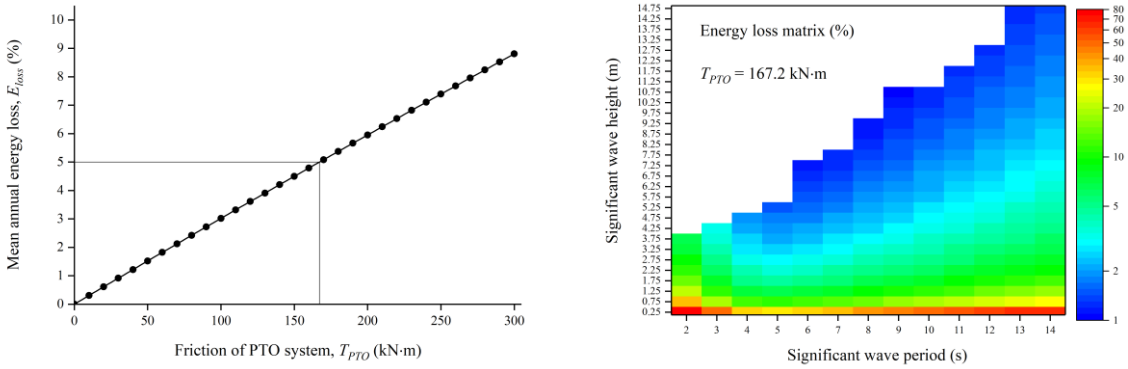

(a) (b)

Fig. 8-16 (a) Mean annual energy loss for different values of PTO frictional moment; (b) Energy loss matrix for different wave states when the mean annual energy loss is 5%.

8.6.8 Local Sensitivity

Local sensitivity belongs to the one-at-a-time (OAT) method, which is calculated when one factor is changed and all other factors are fixed. Dimensionless local sensitivity coefficients S, based on an automatic differentiation technique (Christopher Frey and Patil, 2002), are calculated by the relative variation of output P_o with a small perturbation of a selected input P_i at the designated based value,

$$S = \frac{P_i}{P_o} \cdot \frac{\partial P_o}{\partial P_i} \tag{8-15}$$

Recognizing the optimal values in Table 8-4 as the base values, the average of the local sensitivity coefficients in the range from the lower bound to the upper bound for each variable are computed and shown in Fig. 8-17. Positive sensitivity refers to the positive effects of inputs on the outputs (e.g., monotonously increasing output as input increases), and vice versa. As a result, the axis depth has the highest impact on the mean annual CWR, and the thickness is the most sensitive to the structural mass per unit width. The variables of width and PTO damping have a modest influence on η, whereas the thickness, PTO stiffness, and PTO friction are relatively insensitive to η. The equivalent water filling percentage does not reveal a correlation with η. However, the thickness can severely affect economics. Accordingly, a large value of axis depth and a small value of thickness are determined as the optimal results by MOGA with a trade-off between mean annual CWR and economics.

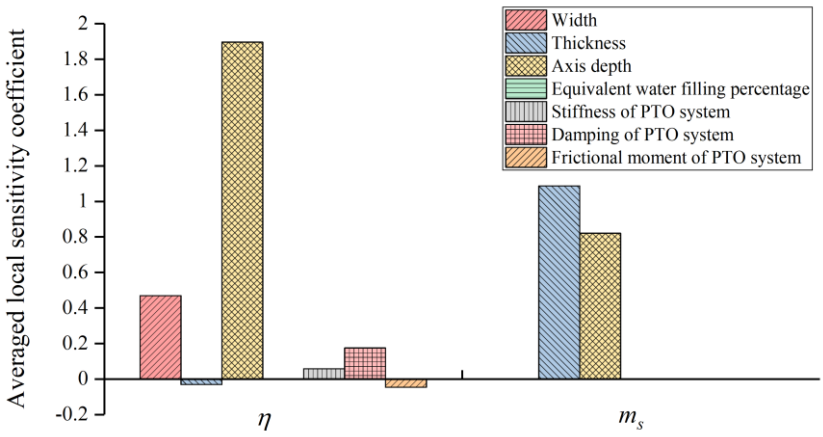

Fig. 8-17 Averaged local sensitivity coefficients of the input parameters to the objective functions.

8.7 Conclusions in the Chapter

This chapter used time-domain BEM to study hydrodynamics under irregular waves and optimize the OWSC sizes and PTO parameters for designated objectives. An assembling OWSC model with adaptive sizes was designed for the target wave energy farm. There are obvious differences in the selection of the drag coefficient between the steady flow and oscillating flow, for example, under waves. The drag coefficients under irregular waves were calibrated with the CFD simulations by determining the minimum error of the normalized kinetic energy. A quadratic fitting curve of the drag coefficient vs. thickness was utilized in the case studies.

The MOGA optimization effectively searches for the optimal solution, in which the width, thickness, axis depth, water filling, PTO stiffness, and PTO damping are optimized, with two objective functions: maximizing the mean annual CWR and minimizing the structural mass per unit width. The optimal OWSC configurations of 16 m width, 1 m thickness, 12 m axis depth, and 0% water filling for the target wave energy farm were determined using the same weighting factor of each objective function. The results of the parametric studies are explained as follows.

(1) A narrow OWSC leads to high CWR under short waves and a wide one can prompt CWR under long waves, so there should be a fittest width for a designated wave energy farm to match well with its scatter diagram.

(2) An intermediate-thickness OWSC reveals higher productivity due to the relatively large wave exciting moment under long waves and the relatively small drag coefficient. However, a large thickness value is harmful to economics. Accordingly, a thin OWSC fits for the low-

density wave energy location, considering that the most frequent significant wave period in the target wave energy farm is not very large, in addition to economizing the material.

(3) A tall OWSC corresponding to a large value of axis depth and a constant freeboard helps to increase the working area to capture more wave energy, but also potentially aggravates the effects of the drag. In shallow water, the taller OWSC brings a dramatic increase in CWR, but a moderate disadvantage of economics.

(4) Water filling contributes little to the mean annual CWR, because it is propitious to improve the hydrodynamic behavior under long waves, but reduces the capability of capturing wave energy under short waves. When the sea state becomes severe, raising the filling water can be a control strategy to enhance the instantaneous CWR, but the effect is limited.

(5) The fittest stiffness of PTO system boosts the CWRs for all wave conditions, but a very high value of PTO stiffness shifts down the natural period, and thus, leads to the mediocre performance under long waves.

(6) The mean annual CWR initially exhibits an aggressive increase as the PTO damping grows, then a stable trend, and afterward a mild decrease after its peak with the further increment of PTO damping. In real operation, when halting the decision of PTO damping, a large value guarantees great power.

(7) The friction of the PTO system indicates an approximately linear relationship with the mean annual energy loss. In the low waves, friction works evidently, especially far from the wave period of the maximum wave exciting moment. To improve the hydrodynamic performance, the wave period corresponding to the largest wave exciting moment should coordinate well with the energy peak period for a designated wave energy farm.

Owing to the overwhelmingly positive effect of axis depth on the mean annual CWR and the significant negative influence of thickness on the economics, a thin and tall profile of OWSC appears in the optima, impartially trading-off between higher mean annual CWRs and lower costs.

However, this study has some limitations. The drag coefficient is assumed to be a constant value related to the given thickness without variation for other geometric parameters and different wave climates. The energy loss due to wave overtopping is neglected, so the CWR may be overestimated, especially under high waves. Future research will focus on the effects of these nonlinear phenomena on CWR. A part of contents in Chapters 1–4 and this chapter was published in Ocean Engineering ([3] in Publications).

9 Conclusions, Innovations, and Future Research

9.1 Conclusions

Chapter 1 introduced many types of WECs and focused on the numerical research background of the bottom-hinged OWSCs, which were reported in published works having higher capture performance than most other WECs.

Chapter 2 presented the expressions of regular and irregular waves in shallow water. To count the wave energy loss in shallow water, the deep-water irregular wave spectral values should be corrected according to the water depth.

Chapter 3 developed a nonlinear BEM-based mathematical model in both frequency-domain and time-domain methods, taking various nonlinear items, such as nonlinear hydrostatic restoring moment, nonlinear drag moment, and nonlinear PTO friction moment, into account. The BEM model of an Oyster 800-like OWSC was described.

Chapter 4 depicted a CFD-based numerical model, including governing equations and setup in OpenFOAM. It represents a high-fidelity simulation and is employed to calibrate and validate BEM solutions. The CFD model of an Oyster 800-like OWSC was described.

Chapter 5 classified the BEM-based dynamic equations under regular waves as three different modes. BEM was validated well with published experiments. The purely linear solution of pitch amplitude was significantly overestimated in long waves when the pitch amplitude is larger than 30° and the nonlinearities play important roles. A surface-piercing OWSC can capture more power than a same-size fully submerged one in most regular wave conditions. Increasing PTO stiffness helps enhance the peak CWR for a thin flap. For a given regular wave state, a fittest PTO damping exists to ensure maximum CWR. The CWR decreases with increasing drag coefficient or PTO friction moment, especially near the resonant zone.

Chapter 6 studied the resonant behaviors under regular and irregular waves, using time-domain BEM. A corrected wet surface was introduced to improve BEM accuracy. The wave surface correcting factor and drag coefficient was calibrated with CFD. In BEM-based free decay analysis, an intermediate angle was recommended as the initial inclination for estimating the natural period. Under regular waves with uniform wave amplitude rather than uniform wave exciting moment amplitude, the maximum pitch appears near the natural period, as the criterion of judging resonance. Perfect resonance cannot be reached, because a hysteresis of angular velocity relative to the wave exciting moment near the natural period always exists. The

maximum CWR does not coexist with resonance. Under irregular waves, resonance cannot exist stably at a peak period near the natural period. The angular velocity also lags behind the wave exciting moment when the peak period is close to the natural period. The hysterical angle of angular velocity relative to wave exciting moment is affected by either PTO damping or friction. The curves of CWR vs. peak period for different PTO damping exhibit a similar tendency to the results under regular waves.

Chapter 7 discussed the approaches of adjusting PTO parameters to maximize the CWR for an arbitrary wave condition, using frequency-domain BEM. The drag coefficient was calibrated with CFD results. Compared with adjusting PTO damping only, an additional adjustment of PTO stiffness and inertia torque provides a broader resonant bandwidth and can be successfully applicable for a flap-type absorber to enhance the CWR. Under regular waves, the perfect resonance is not the best situation for wave energy harvesting, because a relatively large damping item is remarkedly detrimental to the CWR. The optimal hysteretic phase angle of velocity relative to wave exciting moment gradually increases with increasing wave period. Under irregular waves, adjusting PTO inertia torque is almost ineffective for enhancing the CWR, however, adjusting PTO stiffness is still beneficial to enhance the CWR at short peak periods.

Chapter 8 designed an assembling OWSC model with adaptive sizes and optimized the OWSC sizes and PTO parameters based on time-domain BEM. For selecting the drag coefficient, there are obvious differences between the steady and oscillating flow. The drag coefficient in oscillating flow was significantly affected by the thickness. A quadratic fitting curve of the drag coefficient vs. thickness was employed for the current design. MOGA optimization of the width, thickness, axis depth, water filling, PTO stiffness, and PTO damping was conducted for two objectives: (1) maximizing the mean annual CWR and (2) minimizing the structural mass per unit width. The optimal OWSC sizes and PTO configuration for the target wave energy farm were determined. The comprehensively parametric studies conclude as follows: A narrow OWSC produces high CWR under short waves and a wide one can prompt CWR under long waves; An intermediate-thickness OWSC leads to high CWR due to the relatively large wave exciting moment under long waves and the relatively small drag coefficient; A large axis depth and a constant freeboard help to capture more wave energy in shallow water; Water filling contributes little to the mean annual CWR; A fittest PTO stiffness enhances the CWRs for all wave periods but an extremely large PTO stiffness makes decreases

CWR under long waves; With increasing the PTO damping, the mean annual CWR exhibits an aggressive increase, a stable trend, and a mild decrease; PTO friction has an approximately linear relationship with the mean annual energy loss. Because of the overwhelmingly positive effect of axis depth on the mean annual CWR and the apparently negative influence of thickness on the economics, a slender OWSC represents the optimized geometry.

However, there are some limitations in the present BEM mathematical model. For a given OWSC geometry, the drag coefficient was assumed constant, ignoring the relation to wave conditions. Based on the linear relationship between the wave amplitude and wave exciting moment, only small-amplitude waves can be considered, ignoring various nonlinearities, such as wave overtopping, slamming, etc.

9.2 Innovations

Python codes based on a nonlinear BEM mathematical model, with a balance between accuracy and computational costs, of bottom-hinged OWSCs under small-amplitude regular and irregular waves were developed and validated with high-fidelity CFD simulations.

The thorough studies on resonant behaviors under unidirectional waves help to understand the control strategies of adjusting PTO parameters to maximize the capturing capacity. Some interesting findings were presented, for example, perfect resonance is not the best situation for wave energy harvesting for a flap-type WEC, unlike a point-absorber. The reason was theoretically interpreted for the first time.

MOGA optimization found the fittest OWSC sizes and PTO system for the low-density wave energy farms around Japan. The effects of width, thickness, axis depth, water filling, PTO stiffness, damping, and friction were comprehensively discussed to discover the most sensitive factors for the optimized design.

9.3 Future Research

Conducting 3D experiments of an OWSC under regular and irregular waves is the next plan for validation of numerical simulation.

Developing a mathematical model with low sensitivity to the drag coefficients is a research topic because most of the published papers and current work were significantly affected by the selection of drag coefficients.

The current work focuses on the unidirectional waves pointing to the flap, which are ideal conditions. To describe more realistic seas, the interaction of OWSCs with oblique and multidirectional waves is required.

Strongly nonlinear sea conditions, for example, under the large-amplitude waves, are worthy of investigation.

References

Aderinto, T., Li, H., 2018. Ocean Wave Energy Converters: Status and Challenges. Energies 11, 1250. https://doi.org/10.3390/en11051250

Aggidis, G.A., Taylor, C.J., 2017. Overview of wave energy converter devices and the development of a new multi-axis laboratory prototype. IFAC-PapersOnLine 50, 15651–15656. https://doi.org/10.1016/j.ifacol.2017.08.2391

Alamian, R., Shafaghat, R., Safaei, M.R., 2019. Multi-Objective Optimization of a Pitch Point Absorber Wave Energy Converter. Water 11, 969. https://doi.org/10.3390/w11050969

Alcorn, R., Hunter, S., Signorelli, C., Obeyesekera, R., Finnigan, T., Denniss, T., 2005. Results of the testing of the Energetech wave energy plant at Port Kembla. Energeth Report 5, 44.

Allan, G., Gilmartin, M., McGregor, P., Swales, K., 2011. Levelised costs of Wave and Tidal energy in the UK: Cost competitiveness and the importance of "banded" Renewables Obligation Certificates. Energy Policy 39, 23–39. https://doi.org/10.1016/j.enpol.2010.08.029

Anagnostopoulos, S.A., 1982. Dynamic response of offshore platforms to extreme waves including fluid-structure interaction. Engineering Structures 4, 179–185. https://doi.org/10.1016/0141-0296(82)90007-4

Arena, F., Romolo, A., Malara, G., Ascanelli, A., 2013. On Design and Building of a U-OWC Wave Energy Converter in the Mediterranean Sea: A Case Study, in: Volume 8: Ocean Renewable Energy. Presented at the ASME 2013 32nd International Conference on Ocean, Offshore and Arctic Engineering, American Society of Mechanical Engineers, Nantes, France, p. V008T09A102. https://doi.org/10.1115/OMAE2013-11593

Astariz, S., Iglesias, G., 2015. The economics of wave energy: A review. Renewable and Sustainable Energy Reviews 45, 397–408. https://doi.org/10.1016/j.rser.2015.01.061

Babarit, A., 2015. A database of capture width ratio of wave energy converters. Renewable Energy 80, 610–628. https://doi.org/10.1016/j.renene.2015.02.049

Babarit, A., Hals, J., Muliawan, M.J., Kurniawan, A., Moan, T., Krokstad, J., 2012. Numerical benchmarking study of a selection of wave energy converters. Renewable Energy 41, 44–63. https://doi.org/10.1016/j.renene.2011.10.002

Beatty, S.J., Hall, M., Buckham, B.J., Wild, P., Bocking, B., 2015. Experimental and numerical comparisons of self-reacting point absorber wave energy converters in regular waves. Ocean Engineering 104, 370–386. https://doi.org/10.1016/j.oceaneng.2015.05.027

Benites-Munoz, D., Huang, L., Anderlini, E., Marín-Lopez, J.R., Thomas, G., 2020. Hydrodynamic Modelling of An Oscillating Wave Surge Converter Including Power Take-Off. JMSE 8, 771. https://doi.org/10.3390/jmse8100771

Bhatt, J., Carthy, J., Clark, T., Galea, S., Sutch, A., Tutt, A. and Walker, J., 2016. Optimisation and Development of a Multi-Axis Wave Energy Converter Device. Master of Engineering Project Report, Engineering Department, Lancaster University.

Bhinder, M.A., Babarit, A., Gentaz, L., Ferrant, P., 2012. Effect of Viscous Forces On the Performance of a Surging Wave Energy Converter. Presented at the Twenty-second International Offshore and Polar Engineering Conference, p. ISOPE-I-12-194.

Bouws, E., Günther, H., Rosenthal, W., Vincent, C.L., 1985. Similarity of the wind wave spectrum in finite depth water: 1. Spectral form. J. Geophys. Res. 90, 975. https://doi.org/10.1029/JC090iC01p00975

Bretschneider, C., 1959. Wave variability and wave spectra for wind-generated gravity waves. Beach Erosion Board, US Army Corps of Engineers, Tech. Memo 118, 1–192.

Brito, M., Canelas, R.B., García-Feal, O., Domínguez, J.M., Crespo, A.J.C., Ferreira, R.M.L., Neves, M.G., Teixeira, L., 2020a. A numerical tool for modelling oscillating wave surge converter with nonlinear mechanical constraints. Renewable Energy 146, 2024–2043. https://doi.org/10.1016/ j.renene.2019.08.034

Brito, M., Ferreira, R.M.L., Teixeira, L., Neves, M.G., Canelas, R.B., 2020b. Experimental investigation on the power capture of an oscillating wave surge converter in unidirectional waves. Renewable Energy 151, 975–992. https://doi.org/10.1016/j.renene.2019.11.094

Brito, M., Ferreira, R.M.L., Teixeira, L., Neves, M.G., Gil, L., 2020c. Experimental Investigation of the Flow Field in the Vicinity of an Oscillating Wave Surge Converter. JMSE 8, 976. https://doi.org/10.3390/jmse8120976

Budal, K., Falnes, J., 1982. Wave power conversion by point absorbers: A Norwegian project. International Journal of Ambient Energy 3, 59–67. https://doi.org/10.1080/01430750.1982.9675829

Caires, S., 2005. Global ocean mean wave period data: Validation and description. J. Geophys. Res. 110, C02003. https://doi.org/10.1029/2004JC002631

Calvário, M., Gaspar, J.F., Kamarlouei, M., Hallak, T.S., Guedes Soares, C., 2020. Oil-hydraulic power take-off concept for an oscillating wave surge converter. Renewable Energy 159, 1297–1309. https://doi.org/10.1016/j.renene.2020.06.002

Cameron, L., Doherty, R., Henry, A., Doherty, K., Van't Hoff, J., Kaye, D., Naylor, D., Bourdier, S., Whittaker, T., 2010. Design of the next generation of the Oyster wave energy converter, in: 3rd International Conference on Ocean Energy. ICOE Bilbao, Spain, p. 1e12.

Capper, J., Mi, J., Li, Q., Zuo, L., 2021. Numerical Analysis and Parameter Optimization of a Portable Two-Body Attenuator Wave Energy Converter, in: Volume 10: 33rd Conference on Mechanical Vibration and Sound (VIB). Presented at the ASME 2021 International Design Engineering Technical Conferences and Computers and Information in Engineering Conference, American Society of Mechanical Engineers, Virtual, Online, p. V010T10A005. https://doi.org/10.1115/DETC2021-69977

Causon, D.M., Ingram, D.M., Mingham, C.G., Yang, G., Pearson, R.V., 2000. Calculation of shallow water flows using a Cartesian cut cell approach. Advances in Water Resources 23, 545–562.

https://doi.org/10.1016/S0309-1708(99)00036-6
Chen, W., Dolguntseva, I., Savin, A., Zhang, Y., Li, W., Svensson, O., Leijon, M., 2017. Numerical modelling of a point-absorbing wave energy converter in irregular and extreme waves. Applied Ocean Research 63, 90–105. https://doi.org/10.1016/j.apor.2017.01.004
Cheng, Y., Ji, C., Zhai, G., 2019. Fully nonlinear analysis incorporating viscous effects for hydrodynamics of an oscillating wave surge converter with nonlinear power take-off system. Energy 179, 1067–1081. https://doi.org/10.1016/j.energy.2019.04.189
Cheng, Y., Li, G., Ji, C., Fan, T., Zhai, G., 2020. Fully nonlinear investigations on performance of an OWSC (oscillating wave surge converter) in 3D (three-dimensional) open water. Energy 210, 118526. https://doi.org/10.1016/j.energy.2020.118526
Cho, Y.-H., Nakamura, T., Mizutani, N., Lee, K.-H., 2020. An Experimental Study of a Bottom-Hinged Wave Energy Converter with a Reflection Wall in Regular Waves—Focusing on Behavioral Characteristics. Applied Sciences 10, 6734. https://doi.org/10.3390/app10196734
Choi, S.-J., Lee, K.-H., Gudmestad, O.T., 2015. The effect of dynamic amplification due to a structure's vibration on breaking wave impact. Ocean Engineering 96, 8–20. https://doi.org/10.1016/j.oceaneng.2014.11.012
Choiniere, M.A., Tom, N.M., Thiagarajan, K.P., 2019. Load shedding characteristics of an oscillating surge wave energy converter with variable geometry. Ocean Engineering 186, 105982. https://doi.org/10.1016/j.oceaneng.2019.04.063
Chow, Y.-C., Tzang, S.-Y., Chen, J.-H., Lin, C.-C., 2019. Inertial Effects on the Performance of a Bottom-Hinged Oscillating Wave Surge Converter. Journal of Offshore Mechanics and Arctic Engineering 141, 021902. https://doi.org/10.1115/1.4041203
Christopher Frey, H., Patil, S.R., 2002. Identification and Review of Sensitivity Analysis Methods. Risk Analysis 22, 553–578. https://doi.org/10.1111/0272-4332.00039
Clemente, D., Rosa-Santos, P., Taveira-Pinto, F., 2021. On the potential synergies and applications of wave energy converters: A review. Renewable and Sustainable Energy Reviews 135, 110162. https://doi.org/10.1016/j.rser.2020.110162
Collins, I., Hossain, M., Masters, I., 2019. A review of flexible membrane structures for Wave Energy Converters, in: Proceedings of the 13th European Wave and Tidal Energy Conference (EWTEC 2019), Naples, Italy. pp. 1–6.
Combourieu, A., Philippe, M., Alain, L., Espedal, J., 2014. Experimental validation of InWave, a numerical design tool for WECs, in: 5th International Conference on Ocean Energy.
Cordonnier, J., Gorintin, F., De Cagny, A., Clément, A.H., Babarit, A., 2015. SEAREV: Case study of the development of a wave energy converter. Renewable Energy 80, 40–52. https://doi.org/10.1016/j.renene.2015.01.061

Cummins, C.P., Dias, F., 2017. A new model of viscous dissipation for an oscillating wave surge converter. J Eng Math 103, 195–216. https://doi.org/10.1007/s10665-016-9868-4

Cummins, W.E., Iiuhl, W., Uinm, A., Cummins, W.E., 1962. The Impulse Response Function and Ship Motions (No. AD0288277). DTIC, Washington, DC, USA.

Dias, F., Renzi, E., Gallagher, S., Sarkar, D., Wei, Y., Abadie, T., Cummins, C., Rafiee, A., 2017. Analytical and computational modelling for wave energy systems: the example of oscillating wave surge converters. Acta Mech. Sin. 33, 647–662. https://doi.org/10.1007/s10409-017-0683-6

Di Lauro, E., Maza, M., Lara, J.L., Losada, I.J., Contestabile, P., Vicinanza, D., 2020. Advantages of an innovative vertical breakwater with an overtopping wave energy converter. Coastal Engineering 159, 103713. https://doi.org/10.1016/j.coastaleng.2020.103713

dos Santos, E.D., Machado, B.N., Zanella, M.M., Gomes, M. das N., Souza, J.A., Isoldi, L.A., Rocha, L.A.O., 2014. Numerical Study of the Effect of the Relative Depth on the Overtopping Wave Energy Converters According to Constructal Design. DDF 348, 232–244. https://doi.org/10.4028/www.scientific.net/DDF.348.232

ESI OpenCFD. OpenFOAM v1912. URL https://www.openfoam.com/news/main-news/openfoam-v1912 (accessed Dec.13 2021).

Falcão, A.F. de O., 2010. Wave energy utilization: A review of the technologies. Renewable and Sustainable Energy Reviews 14, 899–918. https://doi.org/10.1016/j.rser.2009.11.003

Falcão, A.F. de O., 2008. Phase control through load control of oscillating-body wave energy converters with hydraulic PTO system. Ocean Engineering 35, 358–366. https://doi.org/10.1016/j.oceaneng.2007.10.005

Falcão, A.F.O., Henriques, J.C.C., 2016. Oscillating-water-column wave energy converters and air turbines: A review. Renewable Energy 85, 1391–1424. https://doi.org/10.1016/j.renene.2015.07.086

Faltinsen, O., 1990. Sea loads on ships and offshore structures. Cambridge University Press, Cambridge, UK.

Ferziger, J.H., Perić, M., Street, R.L., 2002. Computational methods for fluid dynamics. Springer, Berlin/Heidelberg, Germany.

Finnegan, W., Goggins, J., 2012. Numerical simulation of linear water waves and wave–structure interaction. Ocean Engineering 43, 23–31. https://doi.org/10.1016/j.oceaneng.2012.01.002

Fisher, R.A., 1936. Design of Experiments. BMJ 1, 554–554. https://doi.org/10.1136/bmj.1.3923.554-a

Flocard, F., Finnigan, T.D., 2009. Experimental investigation of power capture from pitching point absorbers, in: Eight European Wave and Tidal Energy Conference, Upsalla.

Flocard, F., Finnigan, T.D., 2012. Increasing power capture of a wave energy device by inertia adjustment. Applied Ocean Research 34, 126–134. https://doi.org/10.1016/j.apor.2011.09.003

Folley, M., Whittaker, T., Van't Hoff, J., 2007a. The design of small seabed-mounted bottom-hinged wave energy converters, in: Proceedings of the 7th European Wave and Tidal Energy Conference. Citeseer, p. 312.

Folley, M., Whittaker, T.J.T., Henry, A., 2007b. The effect of water depth on the performance of a small surging wave energy converter. Ocean Engineering 34, 1265–1274. https://doi.org/10.1016/j.oceaneng.2006.05.015

Galvin, C.J., 1972. Wave breaking in shallow water. Waves on beaches and resulting sediment transport 413–456.

Gao, H., Liang, R., 2019. Performance analysis of axisymmetric floating energy harvesters and influences of parameters and shape variation. Int J Energy Res er.4398. https://doi.org/10.1002/er.4398

Gao, H., Yu, Y., 2018. The dynamics and power absorption of cone-cylinder wave energy converters with three degree of freedom in irregular waves. Energy 143, 833–845. https://doi.org/10.1016/j.energy.2017.11.036

Garcia-Teruel, A., Forehand, D.I.M., 2021. A review of geometry optimisation of wave energy converters. Renewable and Sustainable Energy Reviews 139, 110593. https://doi.org/10.1016/j.rser.2020.110593

Ghafari, H.R., Ghassemi, H., He, G., 2021. Numerical study of the Wavestar wave energy converter with multi-point-absorber around DeepCwind semisubmersible floating platform. Ocean Engineering 232, 109177. https://doi.org/10.1016/j.oceaneng.2021.109177

Ghaneei, H., Mahmoudi, M., 2021. Simulation, Optimization and Economic Assessment of Pelamis Wave Energy Converter. SSRN Journal. https://doi.org/10.2139/ssrn.3939656

Goda, Y., 1988. Statistical Variability of Sea State Parameters as a Function of Wave Spectrum. Coastal Engineering in Japan 31, 39–52. https://doi.org/10.1080/05785634.1988.11924482

Gomes, R.P.F, Henriques, J.C.C, Gato, L.M.C, Falcão, A.F.O., 2010. IPS two-body wave energy converter: acceleration tube optimization, in: The Twentieth International Offshore and Polar Engineering Conference. OnePetro.

Gomes, R.P.F., Henriques, J.C.C., Gato, L.M.C., Falcão, A.F.O., 2012. Hydrodynamic optimization of an axisymmetric floating oscillating water column for wave energy conversion. Renewable Energy 44, 328–339. https://doi.org/10.1016/j.renene.2012.01.105

Gomes, R.P.F., Lopes, M.F.P., Henriques, J.C.C., Gato, L.M.C., Falcão, A.F.O., 2015. The dynamics and power extraction of bottom-hinged plate wave energy converters in regular and irregular waves. Ocean Engineering 96, 86–99. https://doi.org/10.1016/j.oceaneng.2014.12.024

Gunawardane, S., Kankanamge, C., Watabe, T., 2016. Study on the Performance of the "Pendulor" Wave Energy Converter in an Array Configuration. Energies 9, 282. https://doi.org/10.3390/en9040282

Hasselmann, K., Barnett, T.P., Bouws, E., Carlson, H., Cartwright, D.E., Enke, K., Ewing, J., Gienapp, A., Hasselmann, D., Kruseman, P., others, 1973. Measurements of wind-wave growth and swell decay during the Joint North Sea Wave Project (JONSWAP). Ergaenzungsheft zur Deutschen Hydrographischen Zeitschrift, Reihe A.

He, H., Qu, Q., Li, J., 2013. Numerical Simulation of Section Systems in the Pelamis Wave Energy Converter. Advances in Mechanical Engineering 5, 186056. https://doi.org/10.1155/2013/186056

Heath, T., 2007. The development of a turbo-generation system for application in OWC breakwaters, in: Proceedings of the 7th European Wave and Tidal Energy Conference. Porto, Portugal.

Heath, T, Whittaker, T.J.T., Boake, C.B., 2001. The design, construction and operation of the LIMPET wave energy converter (Islay, Scotland) [Land Installed Marine Powered Energy Transformer].

Henderson, R., 2006. Design, simulation, and testing of a novel hydraulic power take-off system for the Pelamis wave energy converter. Renewable Energy 31, 271–283. https://doi.org/10.1016/j.renene.2005.08.021

Henry, A., Folley, M., Whittaker, T., 2018. A conceptual model of the hydrodynamics of an oscillating wave surge converter. Renewable Energy 118, 965–972. https://doi.org/10.1016/j.renene.2017.10.090

Henry, A., Kimmoun, O., Nicholson, J., Dupont, G., Wei, Y., Dias, F., 2014. A Two Dimensional Experimental Investigation of Slamming of an Oscillating Wave Surge Converter. Presented at the Twenty-fourth International Ocean and Polar Engineering Conference, Busan, Korea, p. ISOPE-I-14-448.

Hirt, C.W., Nichols, B.D., 1981. Volume of fluid (VOF) method for the dynamics of free boundaries. Journal of Computational Physics 39, 201–225. https://doi.org/10.1016/0021-9991(81)90145-5

Holland, J.H., 1992. Adaptation in natural and artificial systems: an introductory analysis with applications to biology, control, and artificial intelligence. MIT Press, Cambridge, MA, USA.

Hughes, S.A., 1984. The TMA Shallow-Water Spectrum Description and Applications. COASTAL ENGINEERING RESEARCH CENTER VICKSBURG MS.

Issa, R.I., 1986. Solution of the implicitly discretised fluid flow equations by operator-splitting. Journal of Computational Physics 62, 40–65. https://doi.org/10.1016/0021-9991(86)90099-9

Istrati, D., Buckle, I.G., 2014. Effect of fluid-structure interaction on connection forces in bridges due to tsunami loads, in: Proceedings of the 30th US-Japan Bridge Engineering Workshop, Washington, DC, USA. pp. 21–23.

Jefferys, E.R., 1984. Simulation of wave power devices. Applied Ocean Research 6, 31–39. https://doi.org/10.1016/0141-1187(84)90026-9

Jiang, X., Day, S., Clelland, D., 2018. Hydrodynamic responses and power efficiency analyses of an oscillating wave surge converter under different simulated PTO strategies. Ocean Engineering 170, 286–297. https://doi.org/10.1016/j.oceaneng.2018.10.050

King, R., 1977. A review of vortex shedding research and its application. Ocean Engineering 4, 141–171.

https://doi.org/10.1016/0029-8018(77)90002-6
Kitaigordskii, S.A., Krasitskii, V.P., Zaslavskii, M.M., 1975. On Phillips' Theory of Equilibrium Range in the Spectra of Wind-Generated Gravity Waves. J. Phys. Oceanogr. 5, 410–420. https://doi.org/10.1175/1520-0485(1975)005<0410:OPTOER>2.0.CO;2
Kofoed, J.P., 2009. Hydraulic evaluation of the DEXA wave energy converter. Department of Civil Engineering, Aalborg University, Aalborg. DCE Technical Reports.
Kofoed, J.P., Frigaard, P., Friis-Madsen, E., Sørensen, H.Chr., 2006. Prototype testing of the wave energy converter wave dragon. Renewable Energy 31, 181–189. https://doi.org/10.1016/j.renene.2005.09.005
Koh, H.-J., Ruy, W.-S., Cho, I.-H., Kweon, H.-M., 2015. Multi-objective optimum design of a buoy for the resonant-type wave energy converter. J Mar Sci Technol 20, 53–63. https://doi.org/10.1007/s00773-014-0268-z
Kolios, A., Di Maio, L.F., Wang, L., Cui, L., Sheng, Q., 2018. Reliability assessment of point-absorber wave energy converters. Ocean Engineering 163, 40–50. https://doi.org/10.1016/j.oceaneng.2018.05.048
Korde, U.A., 1999. Efficient primary energy conversion in irregular waves. Ocean Engineering 26, 625–651. https://doi.org/10.1016/S0029-8018(98)00017-1
Kraemer, D.R.B., McCormick, M.E., Ohl, C.O.G., 2001. Comparison of experimental and theoretical results of the motions of a McCabe wave pump. Presented at the 4th European wave energy conference, Aalborg, Denmark.
Lagoun, M.S., Benalia, A., Benbouzid, M.E.H., 2010. Ocean wave converters: State of the art and current status, in: 2010 IEEE International Energy Conference. Presented at the 2010 IEEE International Energy Conference (ENERGYCON 2010), IEEE, Manama, Bahrain, pp. 636–641. https://doi.org/10.1109/ENERGYCON.2010.5771758
Lavelle, J., Kofoed, J.P., 2011. Experimental testing of the Langlee wave energy converter, in: Proceedings of the 9th European Wave and Tidal Energy Conference, Southampton, UK. pp. 5–9.
Li, B., Sui, F., Yang, B., 2020. An efficient multi-factor geometry optimization based on motion analysis and resonance response for hinged double-body floating wave energy converter. Science Progress 103, 003685042095015. https://doi.org/10.1177/0036850420950151
Li, Y., Yu, Y.-H., 2012. A synthesis of numerical methods for modeling wave energy converter-point absorbers. Renewable and Sustainable Energy Reviews 16, 4352–4364. https://doi.org/10.1016/j.rser.2011.11.008
Liao, Z., Gai, N., Stansby, P., Li, G., 2020. Linear Non-Causal Optimal Control of an Attenuator Type Wave Energy Converter M4. IEEE Trans. Sustain. Energy 11, 1278–1286. https://doi.org/10.1109/TSTE.2019.2922782
Liang, C., Zuo, L., 2017. On the dynamics and design of a two-body wave energy converter. Renewable Energy 101, 265–274. https://doi.org/10.1016/j.renene.2016.08.059
Lilypad. URL http://www.energyisland.com/projects/lilypad/lilypad.html (accessed June 5 2022)

Lin, C.-C., Chow, Y.-C., Tzang, S.-Y., Chiou, C.-Y., Huang, Y.-Y., 2018. Numerical Study on the Geometric and Inertial Parameters for Oscillating Wave Surge Converters, in: Volume 10: Ocean Renewable Energy. Presented at the ASME 2018 37th International Conference on Ocean, Offshore and Arctic Engineering, American Society of Mechanical Engineers, Madrid, Spain, p. V010T09A040. https://doi.org/10.1115/OMAE2018-77938

Liu, C., Yang, Q., Bao, G., 2017. Performance investigation of a two-raft-type wave energy converter with hydraulic power take-off unit. Applied Ocean Research 62, 139–155. https://doi.org/10.1016/j.apor.2016.12.002

Liu, Y., Cho, Y.-H., Mizutani, N., Nakamura, T., 2022a. Study on the Resonant Behaviors of a Bottom-Hinged Oscillating Wave Surge Converter. JMSE 10, 2. https://doi.org/10.3390/jmse10010002

Liu, Y., Mizutani, N., Cho, Y.-H., Nakamura, T., 2022b. Nonlinear hydrodynamic analysis and optimization of oscillating wave surge converters under irregular waves. Ocean Engineering 250, 110888. https://doi.org/10.1016/j.oceaneng.2022.110888

Liu, Y., Mizutani, N., Zhao, Y., 2021a. Nonlinear Hydrodynamic Analysis of Oscillating Wave Surge Converters under Regular Waves. IJOPE 31, 453–461. https://doi.org/10.17736/ijope.2021.hc23

Liu, Z., Wang, Y., Hua, X., 2020. Numerical studies and proposal of design equations on cylindrical oscillating wave surge converters under regular waves using SPH. Energy Conversion and Management 203, 112242. https://doi.org/10.1016/j.enconman.2019.112242

Liu, Z., Wang, Y., Hua, X., 2021b. Proposal of a novel analytical wake model and array optimization of oscillating wave surge converter using differential evolution algorithm. Ocean Engineering 219, 108380. https://doi.org/10.1016/j.oceaneng.2020.108380

Loh, T.T., Greaves, D., Maeki, T., Vuorinen, M., Simmonds, D., Kyte, A., 2016. Numerical modelling of the WaveRoller device using OpenFOAM, in: Proceedings of the 3rd Asian Wave & Tidal Energy Conference.

López, I., Andreu, J., Ceballos, S., Martínez de Alegría, I., Kortabarria, I., 2013. Review of wave energy technologies and the necessary power-equipment. Renewable and Sustainable Energy Reviews 27, 413–434. https://doi.org/10.1016/j.rser.2013.07.009

López, I., Carballo, R., Iglesias, G., 2019. Site-specific wave energy conversion performance of an oscillating water column device. Energy Conversion and Management 195, 457–465. https://doi.org/10.1016/j.enconman.2019.05.030

López, M., Taveira-Pinto, F., Rosa-Santos, P., 2017. Numerical modelling of the CECO wave energy converter. Renewable Energy 113, 202–210. https://doi.org/10.1016/j.renene.2017.05.066

Magkouris, A., Bonovas, M., Belibassakis, K., 2020. Hydrodynamic Analysis of Surge-Type Wave Energy Devices in Variable Bathymetry by Means of BEM. Fluids 5, 99.

https://doi.org/10.3390/fluids5020099
Mann, L.D., 2011. Application of ocean observations & analysis: The CETO wave energy project, in: Operational Oceanography in the 21st Century. Springer, pp. 721–729.
Margheritini, L., Vicinanza, D., Frigaard, P., 2009. SSG wave energy converter: Design, reliability and hydraulic performance of an innovative overtopping device. Renewable Energy 34, 1371–1380. https://doi.org/10.1016/j.renene.2008.09.009
Maria-Arenas, A., Garrido, A.J., Rusu, E., Garrido, I., 2019. Control Strategies Applied to Wave Energy Converters: State of the Art. Energies 12, 3115. https://doi.org/10.3390/en12163115
Maskell, E., 1955. Flow separation in three dimensions. RAE Report No. Aero 2565.
Masuda, Y., McCormick, M.E., 1986. Experiences in pneumatic wave energy conversion in Japan, in: Coastal Engineering 1986. ASCE, pp. 1–33.
McCabe, A.P., Bradshaw, A., Meadowcroft, J.A.C., Aggidis, G., 2006. Developments in the design of the PS Frog Mk 5 wave energy converter. Renewable Energy 31, 141–151. https://doi.org/10.1016/j.renene.2005.08.013
Mckay, M.D., Beckman, R.J., Conover, W.J., 2000. A Comparison of Three Methods for Selecting Values of Input Variables in the Analysis of Output From a Computer Code. Technometrics 42, 55–61. https://doi.org/10.1080/00401706.2000.10485979
Mehlum, E., 1986. Tapchan, in: Hydrodynamics of Ocean Wave-Energy Utilization. Springer, pp. 51–55.
Mitchell, M., 1998. An introduction to genetic algorithms. MIT Press, Cambridge, MA, USA.
Mitsuyasu, H., 1970. On the growth of wind-generated waves (2)-spectral shape of wind waves at finite fetch, in: Proc. 17th Japanese Conf. Coastal Eng., 1970. JSCE.
Monaghan, J.J., 1994. Simulating Free Surface Flows with SPH. Journal of Computational Physics 110, 399–406. https://doi.org/10.1006/jcph.1994.1034
Morison, J.R., Johnson, J.W., Schaaf, S.A., 1950. The Force Exerted by Surface Waves on Piles. Journal of Petroleum Technology 2, 149–154. https://doi.org/10.2118/950149-G
Mottahedi, H.R., Anbarsooz, M., Passandideh-Fard, M., 2018. Application of a fictitious domain method in numerical simulation of an oscillating wave surge converter. Renewable Energy 121, 133–145. https://doi.org/10.1016/j.renene.2018.01.021
National Maritime Research Institute Japan. Statistical Database of Wind and Waves around Japan. URL https://www.nmri.go.jp/wwjapan/namikaze_main_e.html (accessed July 5 2021).
Newman, J.N., 2018. Marine hydrodynamics. MIT Press, Cambridge, MA, USA.
Ning, D., Liu, C., Zhang, C., Göteman, M., Zhao, H., Teng, B., 2017. Hydrodynamic performance of an oscillating wave surge converter in regular and irregular waves: an experimental study. Journal of Marine Science and Technology 25, 4. https://doi.org/10.6119/JMST-017-0504-1
Ocean Harvesting Technologies. URL https://oceanharvesting.com/ (accessed June 5 2022)

Ocean Power Technologies.URL https://www.oceanpowertechnologies.com/ (accessed June 5 2022)
Osawa, H., Miyazaki, T., Miyajima, S., 2013. Characteristics of Hydrodynamics and Generating Output of the Offshore Floating Wave Energy Device "Mighty Whale." Journal of Offshore Mechanics and Arctic Engineering 135, 011901. https://doi.org/10.1115/1.4007248
O'Boyle, L., Doherty, K., van't Hoff, J., Skelton, J., 2015. The value of full scale prototype data-testing oyster 800 at emec, orkney, in: Proceedings of the 11th European Wave and Tidal Energy Conference (EWTEC), Nantes, France. pp. 6–11.
Palma, G., Mizar Formentin, S., Zanuttigh, B., Contestabile, P., Vicinanza, D., 2019. Numerical Simulations of the Hydraulic Performance of a Breakwater-Integrated Overtopping Wave Energy Converter. JMSE 7, 38. https://doi.org/10.3390/jmse7020038
Pastor, J., Liu, Y., 2014. Power Absorption Modeling and Optimization of a Point Absorbing Wave Energy Converter Using Numerical Method. Journal of Energy Resources Technology 136, 021207. https://doi.org/10.1115/1.4027409
Penalba, M., Giorgi, G., Ringwood, J.V., 2017. Mathematical modelling of wave energy converters: A review of nonlinear approaches. Renewable and Sustainable Energy Reviews 78, 1188–1207. https://doi.org/10.1016/j.rser.2016.11.137
Pierson, W.J., Moskowitz, L., 1964. A proposed spectral form for fully developed wind seas based on the similarity theory of S. A. Kitaigorodskii. J. Geophys. Res. 69, 5181–5190. https://doi.org/10.1029/JZ069i024p05181
Plummer, A., Schlotter, M., 2009. Investigating the performance of a hydraulic power take-off, in: Proceedings of the Eight European Wave and Tidal Energy Conference, Uppsala. pp. 729–735.
Rafiee, A., Elsaesser, B., Dias, F., 2013. Numerical Simulation of Wave Interaction With an Oscillating Wave Surge Converter, in: Volume 5: Ocean Engineering. Presented at the ASME 2013 32nd International Conference on Ocean, Offshore and Arctic Engineering, American Society of Mechanical Engineers, Nantes, France, p. V005T06A013. https://doi.org/10.1115/OMAE2013-10195
Rashid, A., Sidenmark, M., Eskilsson, C., Wallentin, M., 2021. IWEC–Model Validation and Cost Optimization of Infinity WEC Wave Energy Converter, in: 14th European Wave and Tidal Energy Conference 5-9th Sept 2021, Plymouth, UK. pp. 2192–1.
Renzi, E., Abdolali, A., Bellotti, G., Dias, F., 2014a. Wave-power absorption from a finite array of oscillating wave surge converters. Renewable Energy 63, 55–68. https://doi.org/10.1016/j.renene.2013.08.046
Renzi, E., Dias, F., 2013a. Hydrodynamics of the oscillating wave surge converter in the open ocean. European Journal of Mechanics - B/Fluids 41, 1–10. https://doi.org/10.1016/j.euromechflu.2013.01.007
Renzi, E., Dias, F., 2013b. Mathematical Modelling of a Flap-Type Wave Energy Converter, in: Volume 9: Odd M. Faltinsen Honoring Symposium on Marine Hydrodynamics. Presented at the ASME 2013 32nd International Conference on Ocean, Offshore and Arctic Engineering, American Society of Mechanical Engineers, Nantes, France, p. V009T12A005. https://doi.org/10.1115/OMAE2013-10215

Renzi, E., Dias, F., 2012. Resonant behaviour of an oscillating wave energy converter in a channel. J. Fluid Mech. 701, 482–510. https://doi.org/10.1017/jfm.2012.194

Renzi, E., Doherty, K., Henry, A., Dias, F., 2014b. How does Oyster work? The simple interpretation of Oyster mathematics. European Journal of Mechanics - B/Fluids 47, 124–131. https://doi.org/10.1016/j.euromechflu.2014.03.007

Renzi, E., Leech, J., Phillips, I., 2017. WEC-GA optimisation tool for an oscillating wave surge converter, in: Proc. European Wave and Tidal Energy Conference. Cork, Ireland.

Retzler, C., 2006. Measurements of the slow drift dynamics of a model Pelamis wave energy converter. Renewable Energy 31, 257–269. https://doi.org/10.1016/j.renene.2005.08.025

Ribeiro e Silva, S., Gomes, R.P.F., Lopes, B.S., Carrelhas, A.A.D., Gato, L.M.C., Henriques, J.C.C., Gordo, J.M., Falcão, A.F.O., 2021. Model testing of a floating wave energy converter with an internal U-shaped oscillating water column. Energy Conversion and Management 240, 114211. https://doi.org/10.1016/j.enconman.2021.114211

Ropero-Giralda, P., Crespo, A.J.C., Tagliafierro, B., Altomare, C., Domínguez, J.M., Gómez-Gesteira, M., Viccione, G., 2020. Efficiency and survivability analysis of a point-absorber wave energy converter using DualSPHysics. Renewable Energy 162, 1763–1776. https://doi.org/10.1016/j.renene.2020.10.012

Rusu, E., Onea, F., 2016. Estimation of the wave energy conversion efficiency in the Atlantic Ocean close to the European islands. Renewable Energy 85, 687–703. https://doi.org/10.1016/j.renene.2015.07.042

Salcedo, F., Ruiz-Minguela, P., Rodriguez, R., Ricci, P., Santos, M., 2009. Oceantec: sea trials of a quarter scale prototype, in: Proceedings of 8th European Wave Tidal Energy Conference. pp. 460–465.

Sarkar, D., Renzi, E., Dias, F., 2015. Effect of a straight coast on the hydrodynamics and performance of the Oscillating Wave Surge Converter. Ocean Engineering 105, 25–32. https://doi.org/10.1016/j.oceaneng.2015.05.025

Sarkar, D., Renzi, E., Dias, F., 2013. Wave Power Extraction by an Oscillating Wave Surge Converter in Random Seas, in: Volume 8: Ocean Renewable Energy. Presented at the ASME 2013 32nd International Conference on Ocean, Offshore and Arctic Engineering, American Society of Mechanical Engineers, Nantes, France, p. V008T09A008. https://doi.org/10.1115/OMAE2013-10188

Sarpkaya, T., 1976. Vortex shedding and resistance in harmonic flow about smooth and rough circular cylinders at high Reynolds numbers. Naval Postgraduate School Monterey CA.

Sarpkaya, T., Isaacson, M., Wehausen, J.V., 1982. Mechanics of Wave Forces on Offshore Structures. Journal of Applied Mechanics 49, 466–467. https://doi.org/10.1115/1.3162189

Schmitt, P., Asmuth, H., Elsäßer, B., 2016a. Optimising power take-off of an oscillating wave surge converter using high fidelity numerical simulations. International Journal of Marine Energy 16, 196–208. https://doi.org/10.1016/j.ijome.2016.07.006

Schmitt, P., Bourdier, S., Whittaker, T., Sarkar, D., Renzi, E., Dias, F., Doherty, K., van 't Hoff, J., 2012a. Hydrodynamic Loading On a Bottom Hinged Oscillating Wave Surge Converter. Presented at the Twenty-second International Offshore and Polar Engineering Conference, p. ISOPE-I-12-198.

Schmitt, P., Doherty, K., Clabby, D., Whittaker, T., 2012b. The opportunities and limitations of using CFD in the development of wave energy converters. Marine & Offshore Renewable Energy 89–97.

Schmitt, P., Elsaesser, B., 2015. On the use of OpenFOAM to model oscillating wave surge converters. Ocean Engineering 108, 98–104. https://doi.org/10.1016/j.oceaneng.2015.07.055

Schmitt, P., Elsäßer, B., 2017. The application of Froude scaling to model tests of Oscillating Wave Surge Converters. Ocean Engineering 141, 108–115. https://doi.org/10.1016/j.oceaneng.2017.06.003

Schmitt, P., Windt, C., Nicholson, J., Elsässer, B., 2016b. Development and validation of a procedure for numerical vibration analysis of an oscillating wave surge converter. European Journal of Mechanics - B/Fluids 58, 9–19. https://doi.org/10.1016/j.euromechflu.2016.02.005

Schubert, B.W., Robertson, W.S.P., Cazzolato, B.S., Ghayesh, M.H., 2020. Linear and nonlinear hydrodynamic models for dynamics of a submerged point absorber wave energy converter. Ocean Engineering 197, 106828. https://doi.org/10.1016/j.oceaneng.2019.106828

Sea Power.URL https://www.seapower.ie/ (accessed June 5 2022)

Sergiienko, N.Y., Cazzolato, B.S., Ding, B., Hardy, P., Arjomandi, M., 2017. Performance comparison of the floating and fully submerged quasi-point absorber wave energy converters. Renewable Energy 108, 425–437. https://doi.org/10.1016/j.renene.2017.03.002

Shadman, M., Estefen, S.F., Rodriguez, C.A., Nogueira, I.C.M., 2018. A geometrical optimization method applied to a heaving point absorber wave energy converter. Renewable Energy 115, 533–546. https://doi.org/10.1016/j.renene.2017.08.055

Singh, U., Abdussamie, N., Hore, J., 2020. Hydrodynamic performance of a floating offshore OWC wave energy converter: An experimental study. Renewable and Sustainable Energy Reviews 117, 109501. https://doi.org/10.1016/j.rser.2019.109501

Tay, Z.Y., Venugopal, V., 2017a. Optimization of Spacing for Oscillating Wave Surge Converter Arrays Using Genetic Algorithm. J. Waterway, Port, Coastal, Ocean Eng. 143, 04016019. https://doi.org/10.1061/(ASCE)WW.1943-5460.0000368

Tay, Z.Y., Venugopal, V., 2017b. Hydrodynamic interactions of oscillating wave surge converters in an array under random sea state. Ocean Engineering 145, 382–394. https://doi.org/10.1016/j.oceaneng.2017.09.012

Tedd, J., Kofoed, J.P., 2009. Measurements of overtopping flow time series on the Wave Dragon, wave energy converter. Renewable Energy 34, 711–717. https://doi.org/10.1016/j.renene.2008.04.036

Tisovska, P., 2019. Description of the overset mesh approach in ESI version of OpenFOAM, in: Proceedings of the CFD with OpenSource Software. Chalmers University of Technology Gothenburg, Sweden.

Tom, N.M., Lawson, M.J., Yu, Y.H., Wright, A.D., 2016. Development of a nearshore oscillating surge wave energy converter with variable geometry. Renewable Energy 96, 410–424. https://doi.org/10.1016/j.renene.2016.04.016

Tongphong, W., Kim, B.-H., Kim, I.-C., Lee, Y.-H., 2021. A study on the design and performance of ModuleRaft wave energy converter. Renewable Energy 163, 649–673. https://doi.org/10.1016/j.renene.2020.08.130

Valério, D., Beirão, P., Sá da Costa, J., 2007. Optimisation of wave energy extraction with the Archimedes Wave Swing. Ocean Engineering 34, 2330–2344. https://doi.org/10.1016/j.oceaneng.2007.05.009

van der Meer, J.W., Briganti, R., Zanuttigh, B., Wang, B., 2005. Wave transmission and reflection at low-crested structures: Design formulae, oblique wave attack and spectral change. Coastal Engineering 52, 915–929. https://doi.org/10.1016/j.coastaleng.2005.09.005

van der Werf, I., van Gent, M., 2018. Wave Overtopping over Coastal Structures with Oblique Wind and Swell Waves. JMSE 6, 149. https://doi.org/10.3390/jmse6040149

Van't Hoff, J., 2009. Hydrodynamic modelling of the oscillating wave surge converter (PhD Thesis). Queen's University Belfast.

Vates Avilés, A., 2009. Wave Energy Converters (PhD Thesis). Università degli studi di Firenze, Facoltà di Ingegneria.

Vicente, P.C., Falcão, A.F.O., Justino, P.A.P., 2013. Nonlinear dynamics of a tightly moored point-absorber wave energy converter. Ocean Engineering 59, 20–36. https://doi.org/10.1016/j.oceaneng.2012.12.008

Victor, L., Troch, P., Kofoed, J.P., 2011. On the Effects of Geometry Control on the Performance of Overtopping Wave Energy Converters. Energies 4, 1574–1600. https://doi.org/10.3390/en4101574

Wahid, F., Sanjana, T., Roy, A., Tareq, Q., Karim, M.A., 2017. Designing of a Pelamis wave energy converter in Matlab Simulink and studying the output characteristics with variation to electrical and mechanical parameters, in: 2017 4th International Conference on Advances in Electrical Engineering (ICAEE), IEEE, Dhaka, pp. 669–674. https://doi.org/10.1109/ICAEE.2017.8255440

Wang, L., Ringwood, J.V., 2021. Control-informed ballast and geometric optimisation of a three-body hinge-barge wave energy converter using two-layer optimisation. Renewable Energy 171, 1159–1170. https://doi.org/10.1016/j.renene.2021.02.125

Wang, Y., Liu, Z., 2021. Proposal of novel analytical wake model and GPU-accelerated array optimization method for oscillating wave surge energy converter. Renewable Energy 179, 563–583. https://doi.org/10.1016/j.renene.2021.07.054

WaveStar. URL http://wavestarenergy.com/ (accessed June 5 2022)

Weber, J., Mouwen, F., Parish, A., Robertson, D., 2009. Wavebob—research & development network and tools in the context of systems engineering, in: Proc. Eighth European Wave and Tidal Energy Conference, Uppsala, Sweden. pp. 416–420.

Wehausen, J.V., Laitone, E.V., 1960. Surface Waves, in: Truesdell, C. (Ed.), Fluid Dynamics / Strömungsmechanik, Encyclopedia of Physics / Handbuch Der Physik. Springer Berlin Heidelberg, Berlin, Heidelberg, pp. 446–778. https://doi.org/10.1007/978-3-642-45944-3_6

Wei, Y., Abadie, T., Henry, A., Dias, F., 2016. Wave interaction with an Oscillating Wave Surge Converter. Part II: Slamming. Ocean Engineering 113, 319–334. https://doi.org/10.1016/j.oceaneng.2015.12.041

Wei, Y., Rafiee, A., Henry, A., Dias, F., 2015. Wave interaction with an oscillating wave surge converter, Part I: Viscous effects. Ocean Engineering 104, 185–203. https://doi.org/10.1016/j.oceaneng.2015.05.002

Weinstein, A., Fredrikson, G., Parks, M.J., Nielsen, K., 2004. AquaBuOY - the offshore wave energy converter numerical modeling and optimization, in: Oceans '04 MTS/IEEE Techno-Ocean '04 (IEEE Cat. No.04CH37600). Presented at the Oceans '04 MTS/IEEE Techno-Ocean '04, IEEE, Kobe, Japan, pp. 1854–1859. https://doi.org/10.1109/OCEANS.2004.1406425

Whittaker, T., Collier, D., Folley, M., Osterried, M., Henry, A., Crowley, M., 2007. The development of Oyster—a shallow water surging wave energy converter, in: Proceedings of the 7th European Wave and Tidal Energy Conference. pp. 11–14.

Whittaker, T., Folley, M., 2012. Nearshore oscillating wave surge converters and the development of Oyster. Phil. Trans. R. Soc. A. 370, 345–364. https://doi.org/10.1098/rsta.2011.0152

Whittaker, T., Folley, M., Causon, D., Ingram, D., Mingham, C., 2005. An experimental and numerical study of oscillating wave surge converters (No. GR/S12326/01). Engineering and Physical Sciences Research Council.

Windt, C., Davidson, J., Akram, B., Ringwood, J.V., 2018a. Performance Assessment of the Overset Grid Method for Numerical Wave Tank Experiments in the OpenFOAM Environment, in: Volume 10: Ocean Renewable Energy. Presented at the ASME 2018 37th International Conference on Ocean, Offshore and Arctic Engineering, American Society of Mechanical Engineers, Madrid, Spain, p. V010T09A006. https://doi.org/10.1115/OMAE2018-77564

Windt, C., Davidson, J., Ringwood, J.V., 2018b. High-fidelity numerical modelling of ocean wave energy systems: A review of computational fluid dynamics-based numerical wave tanks. Renewable and Sustainable Energy Reviews 93, 610–630. https://doi.org/10.1016/j.rser.2018.05.020

Windt, C., Davidson, J., Ringwood, J.V., 2021. Numerical analysis of the hydrodynamic scaling effects for the Wavestar wave energy converter. Journal of Fluids and Structures 105, 103328. https://doi.org/10.1016/j.jfluidstructs.2021.103328

Xu, C., Wang, X., Wang, Z., 2016. Experimental Study on the Dynamics of A Bottom-hinged Oscillating Wave Surge Converter, in: 2016 5th International Conference on Sustainable Energy and Environment Engineering (ICSEEE 2016). Atlantis Press, pp. 210–214.

Yu, Y.-H., Li, Y., Hallett, K., Hotimsky, C., 2014. Design and Analysis for a Floating Oscillating Surge Wave Energy Converter, in: Volume 9B: Ocean Renewable Energy. Presented at the ASME 2014 33rd International Conference on Ocean, Offshore and Arctic Engineering, American Society of Mechanical Engineers, San Francisco, California, USA, p. V09BT09A048. https://doi.org/10.1115/OMAE2014-24511

Zhang, D.H., Shi, Y.X., Huang, C., Si, Y.L., Huang, B., Li, W., 2018. SPH method with applications of oscillating wave surge converter. Ocean Engineering 152, 273–285. https://doi.org/10.1016/j.oceaneng.2018.01.057

Zhang, Y., Zhao, Y., Sun, W., Li, J., 2021. Ocean wave energy converters: Technical principle, device realization, and performance evaluation. Renewable and Sustainable Energy Reviews 141, 110764. https://doi.org/10.1016/j.rser.2021.110764

Zhao, X., Zhang, L., Li, M., Johanning, L., 2021. Experimental investigation on the hydrodynamic performance of a multi-chamber OWC-breakwater. Renewable and Sustainable Energy Reviews 150, 111512. https://doi.org/10.1016/j.rser.2021.111512

Zhao, Y., Ai, Y., Liu, Y., 2018. Study of a Pelamis-Like Wave Energy Converter in Regular Waves. Presented at the 28th International Ocean and Polar Engineering Conference, p. ISOPE-I-18-399.

Zimmerman, J.T.F., 1982. On the Lorentz linearization of a quadratically damped forced oscillator. Physics Letters A 89, 123–124. https://doi.org/10.1016/0375-9601(82)90871-4

Zurkinden, A.S., Ferri, F., Beatty, S., Kofoed, J.P., Kramer, M.M., 2014. Non-linear numerical modeling and experimental testing of a point absorber wave energy converter. Ocean Engineering 78, 11–21. https://doi.org/10.1016/j.oceaneng.2013.12.009

Publications

- Unpublished journal papers:

[1] **Liu, Y.**, Cho, Y.-H., Mizutani, N., Nakamura, T. Hydrodynamics of a Bottom-Hinged Oscillating Wave Surge Converter under Large-Amplitude Regular Waves, Coastal Engineering. (Submitted on June 6, 2022; Under review)

[2] **Liu, Y.**, Mizutani, N., Cho, Y.-H., Nakamura, T. Performance Promotion of a Bottom-hinged Oscillating Wave Surge Converter via Resonant Adjustment, Renewable Energy. (Submitted on Feb. 28, 2022; Under review)

- Published journal papers during doctoral course:

[3] **Liu, Y.**, Mizutani, N., Cho, Y.-H., Nakamura, T., 2022. Nonlinear hydrodynamic analysis and optimization of oscillating wave surge converters under irregular waves. Ocean Engineering 250, 110888. https://doi.org/10.1016/j.oceaneng.2022.110888

[4] **Liu, Y.**, Cho, Y.-H., Mizutani, N., Nakamura, T., 2022. Study on the Resonant Behaviors of a Bottom-Hinged Oscillating Wave Surge Converter. Journal of Marine Science and Engineering 10(1), 2. https://doi.org/10.3390/jmse10010002

[5] **Liu, Y.**, Mizutani, N., Zhao, Y., 2021. Nonlinear Hydrodynamic Analysis of Oscillating Wave Surge Converters under Regular Waves. International Journal of Offshore and Polar Engineering 31(04), 453-461. https://doi.org/10.17736/ijope.2021.hc23

- Published journal papers before doctoral course:

[6] Zhao, Y., Ai, Y., **Liu, Y.**, 2018. Study of a Pelamis-like wave energy converter in regular waves. In The 28th International Ocean and Polar Engineering Conference, Sapporo, Japan, p. ISOPE-I-18-399.

[7] **Liu, Y.**, Liu, J., Li, T., 2012. The plastic dynamic response of two way stiffened square plates with large deflection subjected to blast loads. Engineering Mechanics 29(1):64-69. (in Chinese)

[8] Liu J., **Liu, Y.**, Tang, H., Li, W., 2011. Plastic and large deflection dynamic response analysis of a one way stiffened square plate subjected to blast loads. Journal of Vibration and Shock 30(4):182-187. (in Chinese)

[9] Liu, J., **Liu, Y.**, Li, W., 2010. Dynamic plastic response of one-way stiffened plates subjected to blast loads. China Journal of Ship Research 5(5):6-9. (in Chinese)

- Thesis:

[10] **Liu, Y.**, 2012. The Large Deformation Dynamic Plastic Response of Stiffened Plates Subjected to Blast Loads. Master's Thesis in Huazhong University of Science and Technology, China. (in Chinese)

[11] **Liu, Y.,** 2009. The Large Deflection Dynamic Plastic Response of Blast-loaded Stiffened Square Plates. Bachelor's Thesis in Huazhong University of Science and Technology, China. (in Chinese)

Acknowledgments

Thanks to the doctoral course under the supervision of Prof. Mizutani as well as with the help from Assoc. Prof. Nakamura and Lecturer Cho, I learned so much in the numerical simulations using open-source software, for example, Python, NEMOH, and OpenFOAM. Before the doctoral course, I was only able to complete some coarse hydrodynamic modeling. But now, I am becoming more professional with various research methods in the simulations and gaining a deeper understanding of wave energy devices. My progress is attributed to the advice from professors, which is favorable for my career and will lead me into profound research in the future. So, I'd like to express my greatest gratitude to all the laboratory professors.

I am deeply grateful to my family. My wife took me out of depression with powerful encouragement when I encountered big challenges in the research. My parents also heartened me in my back. I will do my best for great accomplishments to make them proud. I appreciate their support and endless love.

The author also acknowledges the help from all the laboratory students.